1.0

2.8 2.5

3.2 2.2

36

40 2.0

1.1

1.8

1.25 1.4 1.6

MICROCOPY RESOLUTION TEST CHART

NATIONAL BUREAU OF STANDARDS-1963-A

Surface Traction and Crack Propagation in Delamination Wear

Final Report to
The Office of Naval Research

Contract No. N00014-78-C-0252

Nam P. Suh
Hyo-Chol Sin

Laboratory for Manufacturing and Productivity
School of Engineering
Massachusetts Institute of Technology
Cambridge, Massachusetts 02139

November 1981
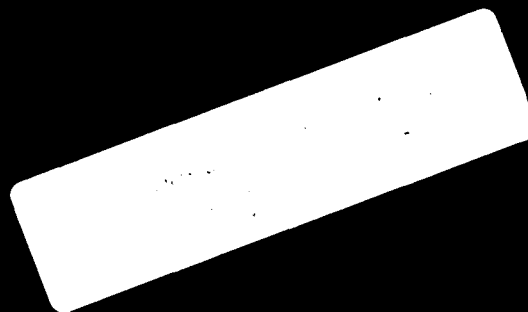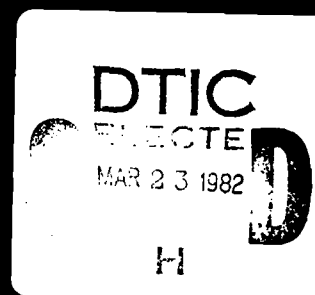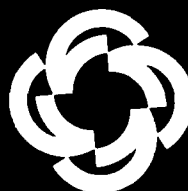
SURFACE TRACTION AND CRACK PROPAGATION
IN DELAMINATION WEAR

Final Report

to

The Office of Naval Research
Contract No. N00014-78-C-0252

Nam P. Suh

Hyo-Chol Sin

Laboratory for Manufacturing and Productivity
School of Engineering
Massachusetts Institute of Technology
Cambridge, Massachusetts 02139

November 1981

REPORT DOCUMENTATION PAGE		READ INSTRUCTIONS BEFORE COMPLETING FORM
1. REPORT NUMBER ----	2. GOVT ACCESSION NO. AD-A-112 354	3. RECIPIENT'S CATALOG NUMBER ----
4. TITLE (and Subtitle) Surface Traction and Crack Propagation in Delamination Wear		5. TYPE OF REPORT & PERIOD COVERED February 1978–September 1981
		6. PERFORMING ORG. REPORT NUMBER ----
7. AUTHOR(s) Nam P. Suh and Hyo-Chol Sin		8. CONTRACT OR GRANT NUMBER(s) N00014-78-C-0252
9. PERFORMING ORGANIZATION NAME AND ADDRESS Laboratory for Manufacturing and Productivity Massachusetts Institute of Technology 77 Mass. Ave., Cambridge, MA 02139		10. PROGRAM ELEMENT, PROJECT, TASK AREA & WORK UNIT NUMBERS ----
11. CONTROLLING OFFICE NAME AND ADDRESS Office of Naval Research Department of the Navy Arlington, VA 22217		12. REPORT DATE November 1981
		13. NUMBER OF PAGES 188
14. MONITORING AGENCY NAME & ADDRESS(If different from Controlling Office) M.I.T. Resident Representative Office of Naval Research Room E19-628, M.I.T. 77 Mass. Ave., Cambridge, MA 02139		15. SECURITY CLASS. (of this report) unclassified
		15a. DECLASSIFICATION/DOWNGRADING SCHEDULE ----

16. DISTRIBUTION STATEMENT (of this Report)

unlimited

DISTRIBUTION STATEMENT A
Approved for public release;
Distribution Unlimited

17. DISTRIBUTION STATEMENT (of the abstract entered in Block 20, if different from Report)

----

18. SUPPLEMENTARY NOTES

----

19. KEY WORDS (Continue on reverse side if necessary and identify by block number)

surface traction, crack propagation, delamination wear, asperity deformation, adhesion, plowing, friction space, Mode II str‍ ensity factor, crack-tip sliding displacement, fracture strain, pla: ne size

20. ABSTRACT (Continue on reverse side if necessary and identify by block number)

The mechanisms of surface traction and crack propagation and their functional relation to slidng wear are investigated experimentally and theoretically. According to the delamination theory of wear, the wear of materials strongly depends on friction because of the effect of surface traction on subsurface deformation and crack nucleation and propagation rates.

DD FORM 1473 EDITION OF 1 NOV 65 IS OBSOLETE
1 JAN 73
S/N 0102-014-6601

(block 20 continued)

Experimental studies using the cylinder-on-cylinder sliding arrangement with the iron based metals show that the coefficient of friction varies with the sliding distance and the environment. It is postulated that it is due to the changing contributions of three components of friction: μ_d due to the deforming asperities; μ_p due to plowing by wear particles and hard surface asperities; μ_a due to adhesion. At any given loading contact only one of these mechanisms may operate and therefore, the local surface traction can vary from contact to contact, affecting the crack nucleation and propagation processes. The three mechanisms responsible for the generation of friction are analyzed using plasticity theory.

The finite element analyses for the elastic and elastic-plastic solids with subsurface cracks indicate that the cracks in sliding wear propagate in a ductile manner. Such fracture parameters as the crack-tip sliding displacement and the fracture strain are found to be useful in characterizing crack propagation.

Finally, a quantitative model of wear based on the crack propagation study is shown to be able to predict the wear rates in delamination wear given the surface traction values. An attempt to correlate friction to wear is made and the implication of the friction and crack propagation mechanisms and the limitations of the present study are discussed.

SURFACE TRACTION AND CRACK PROPAGATION

IN DELAMINATION WEAR

ABSTRACT

The mechanisms of surface traction and crack propagation and their functional relation to sliding wear are investigated experimentally and theoretically. According to the delamination theory of wear, the wear of materials strongly depends on friction because of the effect of surface traction on subsurface deformation and crack nucleation and propagation rates.

Experimental studies using the cylinder-on-cylinder sliding arrangement with the iron based metals show that the coefficient of friction varies with the sliding distance and the environment. It is postulated that it is due to the changing contributions of three components of friction: μ_d due to the deforming asperities; μ_p due to plowing by wear particles and hard surface asperities; μ_a due to adhesion. At any given loading contact only one of these mechanisms may operate and therefore, the local surface traction can vary from contact to contact, affecting the crack nucleation and propagation processes. The three mechanisms responsible for the generation of friction are analyzed using plasticity theory.

The finite element analyses for the elastic and elastic-plastic solids with subsurface cracks indicate that the cracks in sliding wear propagate in a ductile manner. Such fracture parameters as the crack-tip sliding displacement and the fracture strain are found to be useful in characterizing crack propagation.

Finally, a quantitative model of wear based on the crack propagation study is shown to be able to predict the wear rates in delamination wear given the surface traction values. An attempt to correlate friction to wear is made and the implication of the friction and crack propagation mechanisms and the limitations of the present study are discussed.

ACKNOWLEDGEMENTS

TABLE OF CONTENTS

TABLE OF CONTENTS (Cont'd.)

TABLE OF CONTENTS (Cont'd)

7

LIST OF FIGURES

LIST OF FIGURES (Cont'd.)

LIST OF FIGURES (Cont'd.)

LIST OF FIGURES (Cont'd.)

LIST OF FIGURES (Cont'd.)

LIST OF FIGURES (Cont'd.)

13

LIST OF TABLES

1. INTRODUCTION

1.1 Opening Remarks

From pre-historic times tribological concepts and systems have been developed and used to its advantage by mankind. The use of lubricants by the Egyptians in the transport of large building blocks and the early attempts to develop rolling-element bearings in Greek and Roman times are good examples. It is, however, not until the mid-twentieth century that many scientists and engineers began to give serious attention to the fundamentals of tribology, although the first scientific studies of friction dates back to the era of Leonardo da Vinci [1].

Among various theories proposed in the past, the adhesion theories for friction and wear have been widely accepted. Most theories, however, including the adhesion theories, do not predict some of experimentally observed phenomena and sometimes lack physical basis. In 1973 Suh [2], considering these problems, introduced the delamination theory of wear for metals sliding at low speeds. Extensive experimental and analytical work conducted since that time has proved most hypotheses in the theory except the exact mechanism of crack propagation. One of the difficulties in predicting the crack propagation rates was the lack of precise knowledge on surface traction. The validity of friction theories proposed in the past has been questioned since the experimentally observed high coefficient of friction could not be explained by the adhesion theory from the simple continuum mechanics point of view, i.e., the yield condition is violated at the interface. Therefore, the frictional behavior of materials was investigated at

M. I. T. to clarify the friction mechanism. Tohkai studied the effect of varying hardness on friction in 1979 as part of his S. M. thesis [3], showing that the frictional behavior of materials generally affects the wear behavior, which is consistent with the result of the previous investigation by Rabinowicz [4]. This is because of the influence of friction on crack propagation as well as plastic deformation and crack nucleation. Therefore, it is necessary to acquire better understanding of the magnitude of frictional force at each asperity contact and then to apply this knowledge in studying crack propagation so as to determine the wear rate of sliding metal surfaces.

1.2 A Review of Previous Work in Friction and Wear

Since Amontons published the result of his experimental investigation of the friction of unlubricated solids in 1699, such investigators as de la Hire (1732), Euler (1750), Coulomb (1785), Morin (1835) and Hirn (1854) contributed to the classic laws of friction [5]. They considered that friction is due to the interlocking of asperities and the friction force is the tangential force necessary to lift the asperities of one surface over the asperities of the other, which is generally referred to as the roughness theory.

The adhesion theory of friction began to attract the scientists when Tomlinson (1929) and Hardy (1936) attributed friction forces to energy dissipation when the molecules are forced into each other's atomic fields and then separated. At the time the theory seemed to explain the variation of friction with varying surface contamination better than the roughness theory. However, the adhesion theory was

established when Holm [6], Ernst and Merchant [7], and Bowden and
Tabor [8] pointed out the difference between the apparent area and the
real area of contact, and showed that the friction force is independent
of the apparent area of contact, but it is proportional to the real
area of contact.

In early 1940's, several investigators suggested quantitative
models of friction. Ernst and Merchant [7] have proposed that the
frictional force F may be written as

$$F = S + R \qquad\qquad (1.1)$$

where S is the force required to shear the metallic junctions and R
the force required to lift the asperities of one surface over those
of the other. On the other hand, Bowden et al. [9] have suggested
that another factor to be considered is the force required to displace
the softer metal from the path of the slider, P, i.e,

$$F = S + P. \qquad\qquad (1.2)$$

It follows that S = As, R = tanθ and P = A'H where A is the real area
of contact of the metals, s the shear strength of the softer metal,
θ the slope of asperity contact, A' the cross-sectional area of the
grooved track and H the hardness of the softer metal.

Both of the two groups were concerned about the deviation of their
friction laws from Amontons' law and considered that, by neglecting R
and P since they were believed to be small in comparison to S, the
coefficient of friction may be written as

$$\mu = \frac{s}{H} \qquad (1.3)$$

which has been the basic equation for the dominating adhesion theory of friction. Ernst and Merchant derived the expression for the value of shear stress to be applied to a metal to lower its melting point to a certain temperature (usually room temperature), while Bowden et al. estimated s from $S = F - P$ by using their experimental results. However, the hardness-shear strength relationship indicates that the coefficient of friction in the limiting case is approximately equal to 1/6. This value is much lower than those measured in air as well as in vacuum.

In order to explain the discrepancy between the experimentally measured and the theoretically predicted friction coefficients, the adhesion theory has relied on the argument that the area of contact grows as the tangential force is increased to the point at which gross sliding occurs [10-12]. When a tangential force F is applied in addition to the normal load W there is junction growth and the area of contact increases to A. McFarlane and Tabor [10] assumed that the new pressure $p = W/A$ due to the increase in the area of contact and the tangential stress $s = F/A$ satisfy the criterion of plastic flow over the contact region of the following form

$$p^2 + \alpha s^2 = p_0^2 \qquad (1.4)$$

where α is an appropriate constant (3 for a two-dimensional case) and p_0 is the normal pressure when $s = 0$, i.e., p_0 is equal to the hardness H. If the relation between p and s in Eq. 1.4 is true, then it

can be argued that s can reach $p_0/\sqrt{\alpha}$ when $p \to 0$. Using this argument
Tabor [12] explained how the coefficient of friction can reach infinity
theoretically. However, the yield criterion in Eq. 1.4 is not correct
at all since other stress components are completely ignored, for
example, σ_{xx} component in two-dimensional plane strain case which is
necessary to satisfy the equilibrium condition. The slip-line field
solution by Green [13] indicates that the minimum value of p/H (or p/p_0)
is 0.5 for a flat contact. Also, Gupta and Cook [14] have experimentally
shown that the average normal contact pressure for many practical
problems may be obtained by the relation p/H ≃ 0.5.

The adhesion theory of friction became theoretically strong when
Green [15] analyzed plastic junctions using slip-line field theory under
combined normal and shear stress for sliding between unlubricated metals.
Further, the elaboration of Bowden and Tabor's friction theory using
the theoretical solutions and plasticine models [13] has shown that the
distinctive feature of steady sliding is that, on the average, the
surfaces move parallel to each other, and that theoretical plastic
solutions for junctions provide qualitative estimates for μ by con-
sidering the life cycle of a junction. Also, strong junctions that
are sufficiently ductile to survive until the normal stress becomes
tensile were regarded as a possible mechanism for a high value of μ
in vacuum. However, the insufficient accuracy in the normal and
tangential forces exerted through a junction during its life cycle
makes it impossible to estimate μ quantitatively.

Gupta and Cook [14, 16] have extended Green's model and developed
an analytical model, using a statistical distribution of spherical

asperities, to study the contact problem. They included the possibility
of some plastic junctions supporting a tensile normal stress following
Green's suggestion, and showed that the effect of adhesion is unimport-
ant if the tensile stress is less than (2 - 3)k, where k is the shear
yield stress. The model predicts that the number of asperity junctions
increases by the 0.91 power of normal load, while the area of each
individual junction grows only by the 0.09 power with increase of load.
With the statistical description of surface topography the model was
found to agree well with experimental results of friction coefficients.
However, it is the steady state topography that is more relevant in
describing the contact behavior and it is known that this steady state
topography is independent of the initial topography [17].

Recently some plasticity solutions by modifying Green's solution
have been published [18, 19]. Among them Challen and Oxley's approach
is noteworthy: they showed in their rubbing model how hard asperities
deform the surface of a softer metal in the presence of interfacial
adhesion [19]. This may provide a theoretical basis for the adhesion
component of friction.

Since the adhesion theory of friction emphasizes the importance
of adhesion between asperities, a great deal of attention in the past
has been devoted to the role of surface energy and the mutual solubility
of the contact materials. Rabinowicz [20, 21] modified the adhesion
theory of friction by including the effect of surface energy since the
original adhesion theory fails to explain the large variation of
friction coefficient. According to the theory, high friction coeffi-
cients are expected for sliding materials when the ratios of the surface

energy to hardness are high. Further, he has shown that metals with
a high tendency towards solid solution exhibit higher friction coef-
ficients than metals that do not form solid solutions [22]. Although
many experimental results were presented to support the theory, some
of the interpretations are now suspect because surfaces are easily
contaminated by chemisorption and physisorption and the chemical compo-
sition of the surface is different from that of the bulk [23].

As can be noticed from the review above, the adhesion theory of
friction has dominated other theories such as the roughness and plowing
theory, even though an attempt was made to combine the shearing,
plowing and roughness components by Shaw and Macks [24]. The early
roughness theory may be abandoned, since the raising and lowering of the
asperities of one surface over those of the other surface involves no
energy dissipation. Friction is certainly a dissipation mechanism.
Early investigators were concerned about the energy dissipation during
sliding friction. It is, however, only in recent days that the import-
ance of plastic deformation has been recognized in the study of friction
and wear.

The work done by Liu [25], Suh and Sridharan [26] and Tsuya [27]
prompted Rigney and Hirth [28] to propose the following model for
sliding and friction based on the energy balance during plastic
deformation

$$\mu = \frac{w\tau\epsilon}{L} \tag{1.5}$$

where w is the width of the highly deformed region (approximately equal

to the wear track width), t the thickness of the region, τ the shear
stress, ϵ the average strain per cycle and L the applied load.
However, this model does not provide any insignt into the real cause
of friction and moreover, the value of ϵ is the most difficult to
obtain since ϵ is not the steady state strain itself but the strain
increment per cycle.

From dislocation theory it is known that plastic deformation of
crystalline materials deforming in glide occurs if the momentary
critical resolved shear stress is exceeded on any crystallographic slip
system. Based on this Kuhlmann-Wilsdorf [29] recently proposed the
following expression for friction:

$$\mu \simeq m_b \qquad (1.6)$$

where m_b is the Schmid factor. This expression has been found to pre-
dict a number of effects which appear to be consistent with observations,
dependent on surface texture, surface hardness, and surface temperature.
However, the estimate for μ given by Eq. 1.6 may be regarded as the
adhesion component as Kuhlmann-Wilsdorf suggested. Further, many
simplified assumptions made for the estimation of m_b for the case of
polycrystals remain to be refined in regard of multiple slip.

Although many investigations have been conducted about friction,
many questions still remain unanswered; no extensive effort has been
made to isolate the relative contribution of each mechanism responsible
for friction; for example, the plowing component of friction has been
assumed to be small and ignored in the shade of the dominant adhesion
theory. The fact that the frictional behavior does not depend solely

on adhesion is supported by the observation that the frictional force
depends on the history of sliding. The work done at M. I. T. by
Tohkai [3] indicates that the frictional force undergoes significant
changes during the early stages of sliding before reaching steady state.
The time dependent nature of frictional behavior has been largely
ignored in the past, although it is a rich source of information in
understanding friction. The difference between the static and kinetic
coefficients of friction has been quoted in the literature, but the
time dependent nature of the kinetic coefficient of friction has not
been widely reported [30].

In the field of wear the adhesion theory also has been widely
accepted. The theory postulates that wear particles are formed when
the strong metallic junctions get sheared and become loose. Holm [31],
Burwell and Strang [32] and Archard [33] contributed to the theory in
formulating the adhesive wear law. It was the only theory in sliding
wear before the delamination theory of wear emerged in 1973.

1.3 The Delamination Theory of Wear and Recent Developments in the Theory

The delamination theory of wear describes the following sequential
(or independent if there are pre-existing subsurface cracks) events
which lead to loose wear shear formation [34].

(1) When two surfaces come into contact, normal and tangential
loads are transmitted through the contact points. Asperities of the
softer surface are easily deformed and fractured by the repeated
loading action, forming small wear particles. Hard asperities are also
removed but at slower rates. A relatively smooth surface is initially

generated, either when these asperities are deformed or when they are removed.

(2) The surface traction exerted by the harder asperities at the contact points induces incremental plastic deformation per cycle of loading, accumulating with repeated loading. The increment of permaent deformation remaining after given cyclic loading is small compared with the total plastic deformation that occurs in that cycle due to the reversal of shear deformation.

(3) As the subsurface deformation continues, cracks are nucleated below the surface. Crack nucleation very near the surface cannot occur due to the triaxial state of compressive loading which exists just below the contact region.

(4) Once cracks are present (either by crack nucleation or from pre-existing voids and cracks), further loading and deformation causes the cracks to extend and propagate, eventually joining with neighboring cracks. The cracks tend to propagate parallel to the surface at a depth governed by material properties and the state of loading. When the cracks cannot propagate because of the small stress concentration at the crack tip due to an extremely small surface traction at the asperity contact, crack nucleation is the rate controlling mechanism.

(5) When the cracks finally shear to the surface, long and thin wear sheets delaminate. The thickness of the wear sheet is controlled by the location of subsurface crack growth, which is controlled by the normal and tangential loads at the surface.

A series of experimental study conducted at M. I. T. [35] has substantiated the theory, showing the delamination process initiates

when the subsurface plastic deformation causes the nucleation of voids (Fig. 1.1). With further deformation these voids elongate and link up to form long cracks in a direction nearly parallel to the wear surface (Fig. 1.2). At a critical length, these cracks shear to the surface, yielding a wear particle in the form of a long thin sheet as shown in Fig. 1.3. The top surface of the wear sheet is generally smooth, while the fractured surface is rough, often showing dimples (Fig. 1.4).

The mechanism of crack nucleation in materials with inclusions or hard second phase particles is well known, although the exact mechanism in single phase materials is not clear. Jahanmir and Suh [36] investigated the location of crack nucleation, based on the stress criterion, for circular inclusions. It indicates that voids can only nucleate in a small region below the sliding contact and the depth of this region increases with increase of both the normal load and the friction coefficient. It further shows that crack nucleation takes place readily in two-phase materials, leading to a conclusion that crack propagation controls the wear rate in many engineering materials.

The analysis of the mechanics of crack propagation using linear elastic fracture mechanics has shown that the stress intensity factors reach maximum at a distance below the surface, indicating that the cracks at this depth propagate faster than others [37]. Also, the change in stress intensity factor, and therefore the crack propagation rate, increases with increasing coefficient of friction. The stress intensity factors calculated, however, were much smaller than the threshold values, implying that the crack growth process does not

Sliding Direction
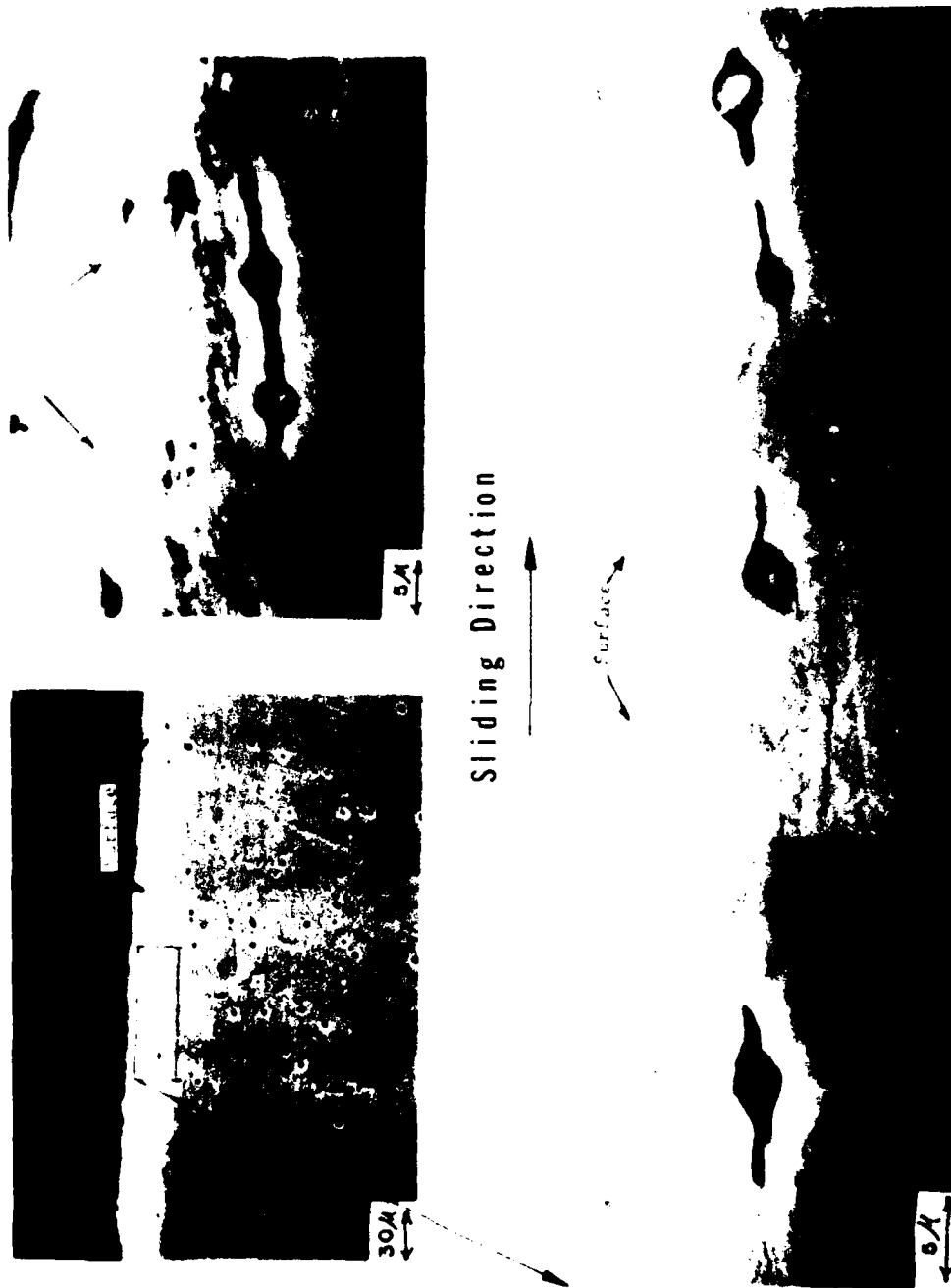
Fig. 1.1 Void formation around inclusions and crack propagation from these voids near the surface in annealed Fe-1.3% Mo [Ref. 41].
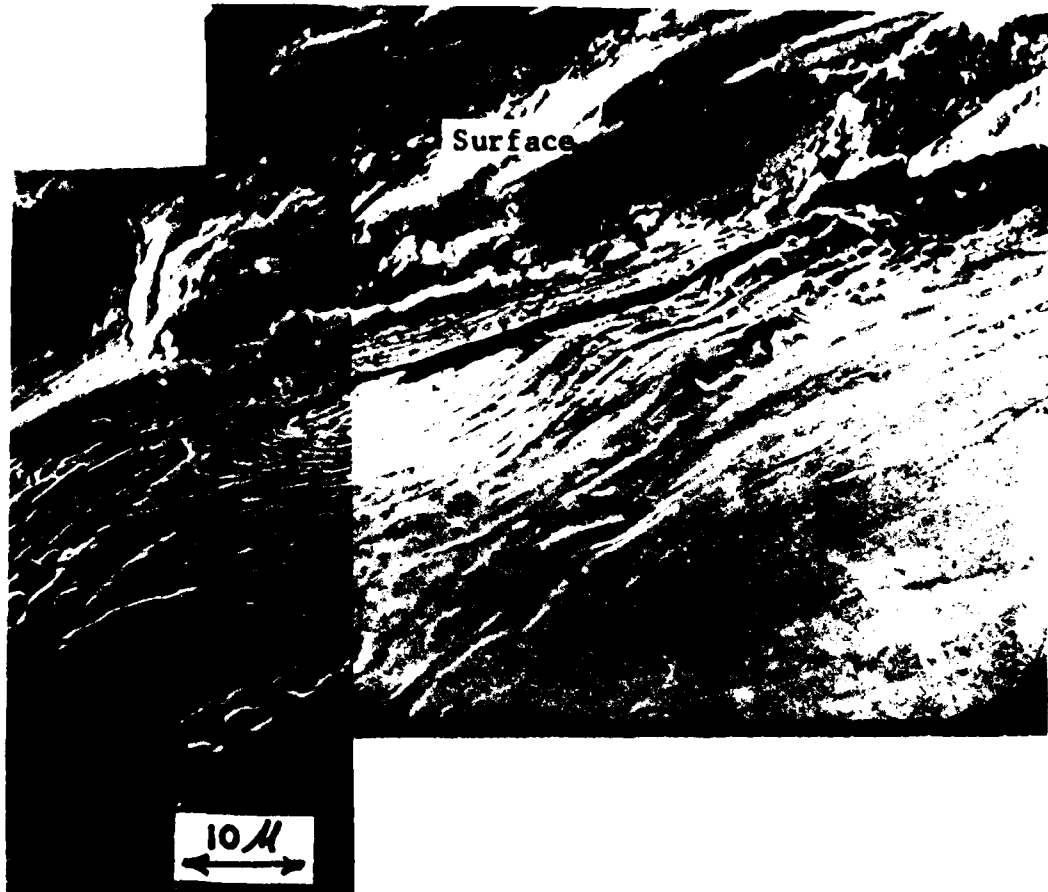
Fig. 1.2 Subsurface deformation and crack formation in iron solid solution [Ref. 35].
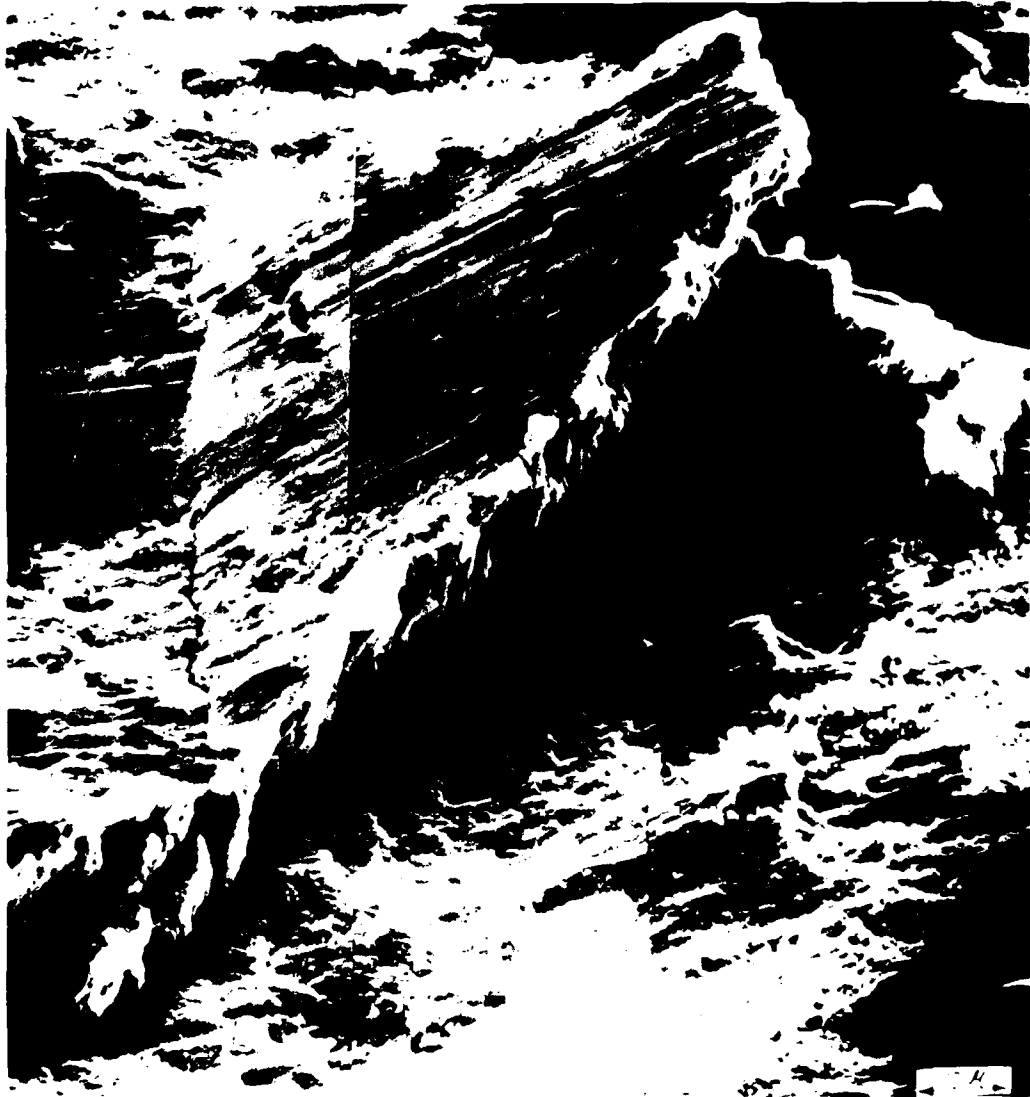
Fig. 1.3 Wear sheet formation in iron solid solution [Ref. 35].
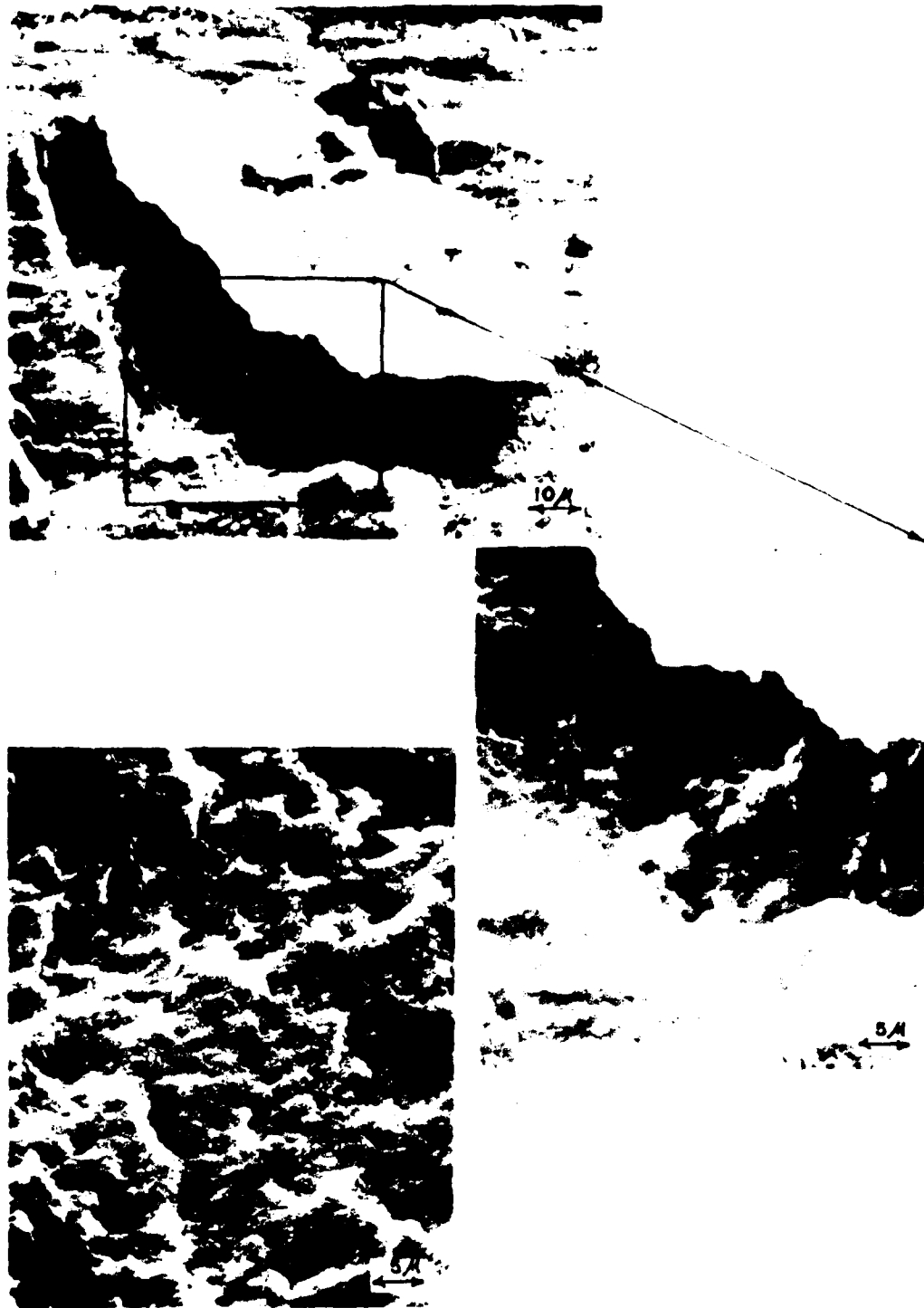
Fig. 1.4   Worn surface of pure iron: (a) wear sheet formation; (b) shear
dimples beneath the wear sheet in (a); (c) dimpled appearance
of a wear crater [Ref. 35].

take place by large macroscopic crack propagation but rather by void nucleation and the deformation of the voids generated. One of the reasons for the small values is that the method applied to calculate the stress intensity factors, namely, the pseudo-stress field and the weighting function method, may be too crude for such a geometrically complicated one in sliding wear.

Recently, Hills and Ashelby [38], Rosenfield [39], and Keer et al. [40] have solved the same subsurface crack problem for the stress intensity factors. The first two papers have considered the Mode II crack propagation and found that the maximum stress intensity factor exists at the compression region ahead of the asperity. On the other hand, the other two by Fleming and Suh and Keer et al. have concentrated on the tensile region. Nevertheless, two points are consistent with each other: shear stresses dominate over normal stresses and the stress intensity factors are too low to cause crack growth.

1.4 Scope of Research

As reviewed in the previous section extensive experimental investigation by Jahanmir [41] has confirmed that wear sheets are indeed formed as a result of plastic deformation, crack nucleation, and crack propagation. As part of his doctoral thesis work at M. I. T. he has shown analytically that cracks can readily nucleate in the subsurface. In addition, the results show that plastic deformation and crack nucleation are greatly affected by frictional force at the asperity contact. The analyses of crack propagation by several investigators have also suggested that the higher the coefficient of friction is the faster cracks propagate.

It is well known that the coefficient of friction has a significant effect on the wear rate [3, 4]. This is due to the effect of the surface traction on plastic deformation, crack nucleation and crack propagation rates. Therefore, it is required that we properly understand the genesis of friction because the magnitude of the frictional force at each contact point, which will in turn affect the crack nucleation and propagation rates, cannot be determined without this understanding.

In order to determine the mechanism of crack propagation a more rigorous method such as the finite element method is required before any conclusion is drawn. The methods used previously were either too approximate or limited.

The objective of this study is to examine the genesis of friction both experimentally and theoretically, to identify the mechanism of crack propagation through a rigorous analysis based on better understanding of the magnitude of surface traction, and to discuss the implications of the mechanism of friction and crack propagation on wear.

A different theory is proposed to explain the frictional behavior of materials based on the experimental results in Chapter 2. Each mechanism of asperity deformation, plowing and adhesion is analyzed by using plasticity theory. In Chapters 3 and 4, the mechanism of crack propagation is discussed through the finite element analysis. It first examines the validity of the linear elastic fracture mechanics approach and then considers the plasticity aspect of subsurface crack growth. Friction and crack propagation are related to the wear rate of materials in Chapter 5. Finally, based on this investigation, conclusions are given in Chapter 6.

2. <u>THE GENESIS OF FRICTION</u>

2.1 <u>Introduction</u>

Recent research has shown that the frictional behavior of materials generally affects the wear behavior. This is due to the fact that high friction not only expedites subsurface deformation and crack nucleation but also accelerates crack propagation. Thus the exact load at each asperity contact must be known first to assess its effect on crack propagation and to compute the crack propagation rate. To be able to do this the exact mechanisms responsible for friction should be identified first of all.

In this chapter a different theory of friction is proposed based on the experimental and theoretical results and quantitative models for the friction-generating mechanisms such as asperity deformation, plowing by wear particles and hard asperities, and adhesion are presented.

2.2 <u>Experiments</u>

A series of experiments were conducted at M. I. T. to study the friction and wear behavior of various combinations of the following materials: Armco iron, AISI 1020, 1045, and 1095 steel. These iron based metals with differing carbon contents have large differences in hard-phase concentrations and hardness. These materials were chosen to minimize chemical differences.

Armco iron was recrystallized at 973 K for one hour. AISI 1020, 1045 and 1095 steels were austenitized at 1173 K for 15 minutes, oil

quenched, and then tempered at 673 K for one hour to obtain a sphero-dized microstructure. The hardness and the volume fraction of cementite are listed in Table 2.1.

The experimental study was initiated by Tohkai [3] as part of his S. M. thesis work and he conducted half of the tests reported in Tables 2.2 and 2.3, that comprises the triangular part of the matrix below the diagonal from upper left to lower right. Later it was extended to this study.

The heat-treated samples were polished with 4/0 abrasive paper, cleaned with trichloroethylene and weighed to an accuracy of 0.01 mg before testing. Some OFHC copper specimens were also tested in air against AISI 1020 steel to compare the initial frictional behavior. The initial coefficient of friction, μ_i, was about the same as those obtained with steel and iron specimens. This initial frictional behavior is being studied by Willett extensively [42].

Samples of 6.35 mm in diameter were tested for friction and wear using cross-cylinder geometry. The specimen (rotating cylinder) was rotated by the spindle of the lathe, and the slider (stationary cylinder) was held stationary in a holder attached to a lathe tool dynamometer which was mounted on the carriage of the lathe. Both normal and tan-gential forces were measured by a dynamometer-recorder assembly.

Tests were conducted in a purified argon atmosphere except for AISI 1020 steel, where some samples were tested in air under both lubricated and unlubricated conditions. Water and light machine oil were used as lubricants. The experimental results were obtained under the following conditions: a normal load of 1 kg (9.8 N); a sliding speed of 0.02 m/s; a total sliding distance of 36 m; room temperature.

Table 2.1. Experimental Materials

Material	Heat Treatment	Vickers Hardness (MPa)	Volume Fraction of Cementite
Armco Iron	973 K, 1 hr; air-cooled	980 ± 50	0.0004
AISI 1020 steel	Austenitized at 1173 K, 15 min; oil-quenched; 673 K, 1 hr; air-cooled	1710 ± 100	0.020
AISI 1045 steel	Spheroidized: 1173 K, 15 min; oil-quenched; 673K, 1 hr; air-cooled	4120 ± 130	0.067
AISI 1095 steel	Spheroidized: 1173 K, 15 min; oil-quenched;673 K, 1 hr; air-cooled	6080 ± 350	0.142

Table 2.2. Friction Coefficients

			Specimen (rotating cylinder)			
			Armco iron	1020 steel	1045 steel	1095 steel
Slider (stationary cylinder)	Armco iron	μ_i	0.13	0.20	0.24	0.20
		μ_s	0.71	0.75	0.69	0.76
		μ^*	----	----	----	----
	1020 steel	μ_i	0.18	0.20	0.13	0.12
		μ_s	0.55	0.68	0.57	0.65
		μ^*	0.80	----	----	----
	1045 steel	μ_i	0.16	0.17	0.17	0.12
		μ_s	0.52	0.53	0.71	0.69
		μ^*	0.77	0.71	----	----
	1095 steel	μ_i	0.17	0.17	0.14	0.17
		μ_s	0.51	0.54	0.58	0.67
		μ^*	0.76	0.73	----	----

μ_i = initial coefficient friction

μ_s = steady state coefficient of friction

μ^* = peak value of the friction coefficient

Table 2.3. Wear Coefficients

		Specimen (rotating cylinder)			
		Amco iron	1020 steel	1045 steel	1095 steel
Slider (stationary cylinder) Amco iron	K_{sp}	46.0 ± 37.2	127.0 ± 45.0	331.0 ± 268.0	1210.0 ± 120.0
	K_{sl}	25.1 ± 17.5	6.94 ± 2.33	16.4 ± 14.0	17.1 ± 0.5
1020 steel	K_{sp}	6.10 ± 2.75	143.0 ± 88.0	25.3 ± 5.0	42.3 ± 17.6
	K_{sl}	5.23 ± 2.60	85.4 ± 48.4	2.57 ± 2.27	1.80 ± 1.33
1045 steel	K_{sp}	3.59 ± 1.69	15.6 ± 5.9	94.2 ± 17.8	565.0 ± 269.0
	K_{sl}	2.89 ± 2.37	13.9 ± 7.2	49.4 ± 7.5	60.0 ± 17.4
1095 steel	K_{sp}	2.11 ± 0.89	8.83 ± 4.04	7.32 ± 5.10	15.1 ± 7.6
	K_{sl}	2.35 ± 0.95	4.97 ± 2.72	5.24 ± 3.78	14.7 ± 10.3

K_{sp} = wear coefficient of specimen; K_{sl} = wear coefficient of slider

All K values are to be multiplied by 10^{-4}.

Some of the specimens were sectioned along the sliding direction to measure the slope of the asperity from micrographs since the asperities of the machined surfaces were orientation dependent.

In the study of the effects of ion implantation on friction and wear by Shepard [43], extremely well polished surfaces were slid against each other to investigate the surface damage after predetermined amounts of sliding. These surfaces were observed using scanning electron microscopy.

2.3 Experimental Results and Observations

The friction and wear coefficients of the iron-carbon system are tabulated in Tables 2.2 and 2.3, respectively. There are several important results worth considering in detail. First of all, the coefficient of friction changes as a function of the distance slid, especially at the early stages of sliding. It usually has a low initial value and gradually increases until reaching a steady state value. After it reaches a maximum value the friction coefficient sometimes drops down if the stationary slider is much harder than the moving specimen. The same pair of materials does not show the drop in the coefficient of friction when their roles are reversed. The initial coefficient of friction is always in the range of about 0.1 to 0.2 regardless of the materials tested and whether or not lubricants are used. Second, the steady state coefficient of friction and the wear rates are higher when identical metals are slid against each other than when a harder stationary slider is slid against a moving softer specimen. However, when a softer stationary slider is slid against a harder moving

specimen, the steady state coefficient of friction is nearly the same as those of the identical materials sliding against each other. In this case the wear rates of unidentical pairs of materials are much greater than those of identical metals.

These changes in the friction and wear behavior are related to the changes in the surface topography as shown in Figs. 2.1 and 2.2, which are the micrographs of the slider surface and the specimen surface, respectively. These figures show that when the stationary slider is harder than the specimens, the hard surface is polished to a mirror finish and the high spots of the softer surface also acquire the same mirror finish. When the delamination process is completed underneath the polished surface, new high spots will be polished to a mirror finish. This does not happen when the stationary slider is softer than the specimen or when identical metals are slid against each other. In these cases many plowing grooves are observed [3] and the surface always stays rough.

From these experimental results the following observations are made:

(1) The coefficients of friction vs. sliding distance (or time) may be summarized by using two typical plots shown in Fig. 2.3. The behavior of Fig. 2.3a always holds when identical metals are slid against each other. The drop in the coefficient of friction in Fig. 2.3b is associated with mutual polishing of the mating surfaces [3, 44]. The behavior shown in Fig. 2.3b results primarily when the hardness of the stationary slider is much greater than the moving specimen.
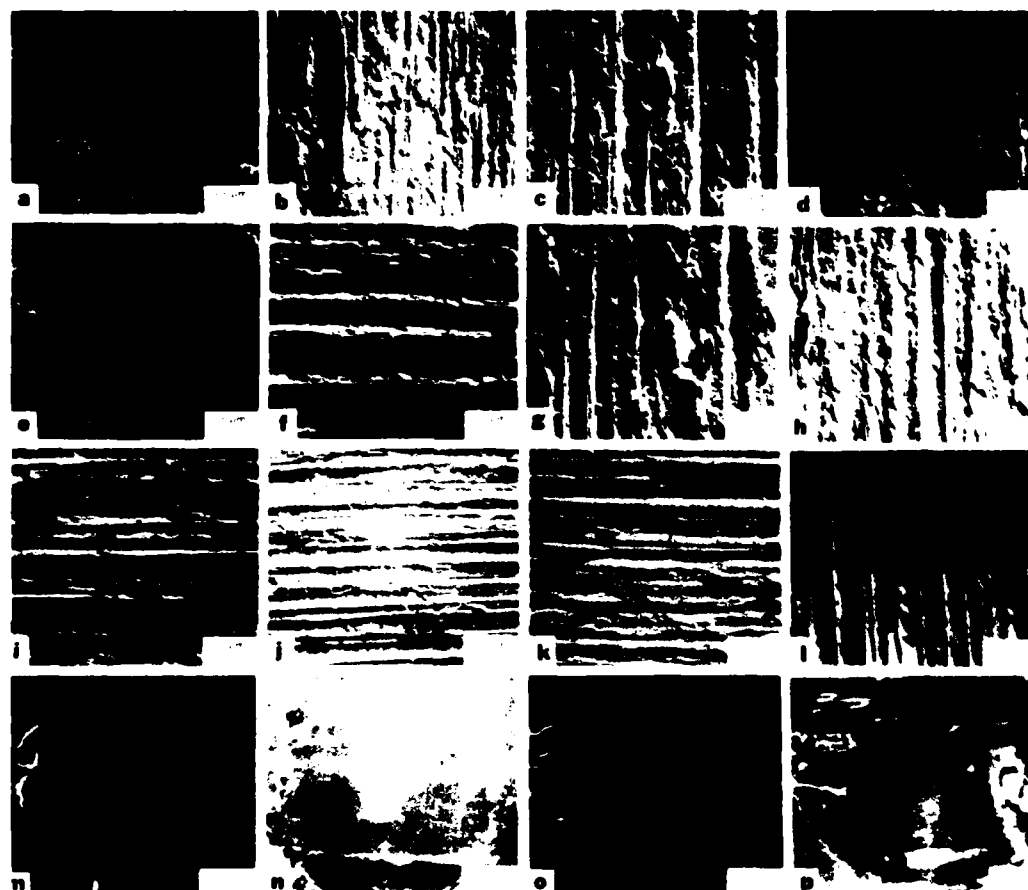
Fig. 2.1   Scanning electron micrographs of the surfaces of worn sliders:
(a), (b), (c), (d) iron on iron, 1020, 1045, and 1095 steel,
respectively; (e), (f), (g), (h) 1020 on iron, 1020, 1045, and
1095 steel, respectively; (i), (j), (k), (l) 1045 on iron, 1020,
1045, and 1095 steel, respectively; (m), (n), (o), (p) 1095 on
iron, 1020, 1045, and 1095 steel, respectively.
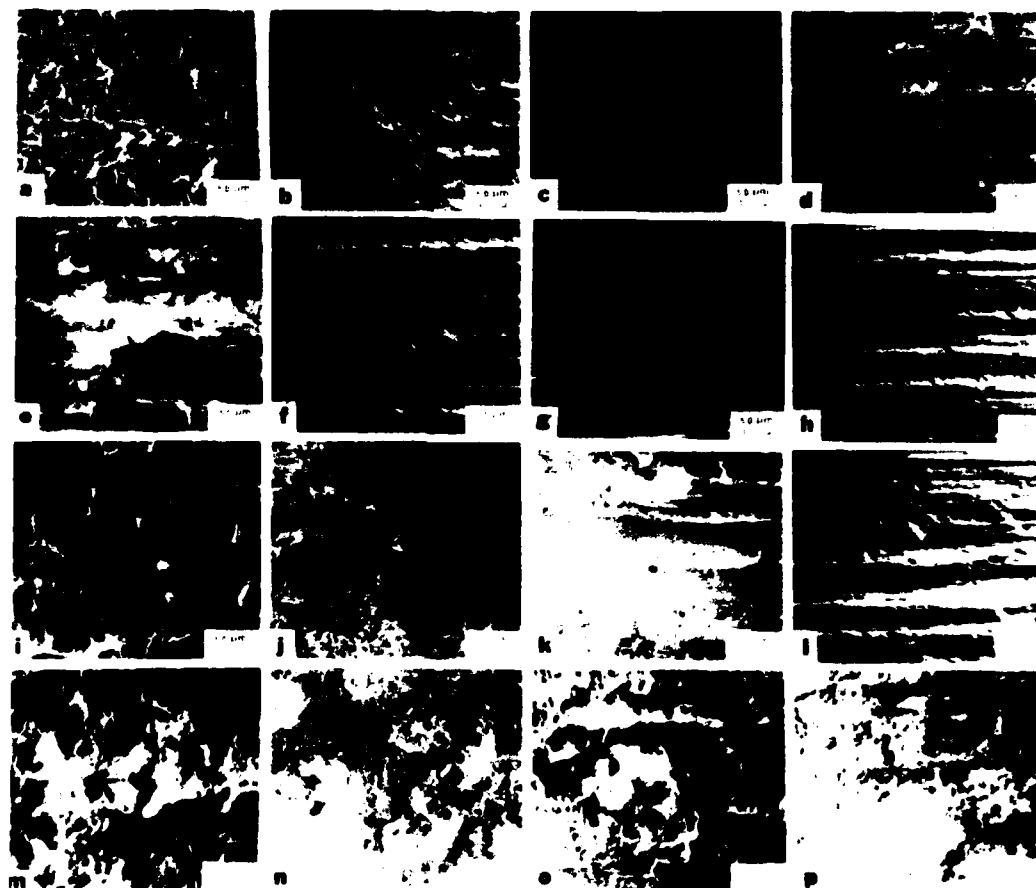
Fig. 2.2 Scanning electron micrographs of the surfaces of worn specimens:
(a), (e), (i), (m) iron on iron, 1020, 1045, and 1095 steel,
respectively; (b), (f), (j), (n) 1020 on iron, 1020, 1045, and
1095 steel, respectively; (c), (g), (k), (o) 1045 on iron, 1020,
1045, and 1095 steel, respectively; (d), (h), (l), (p) 1095 on
iron, 1020, 1045, and 1095 steel, respectively.
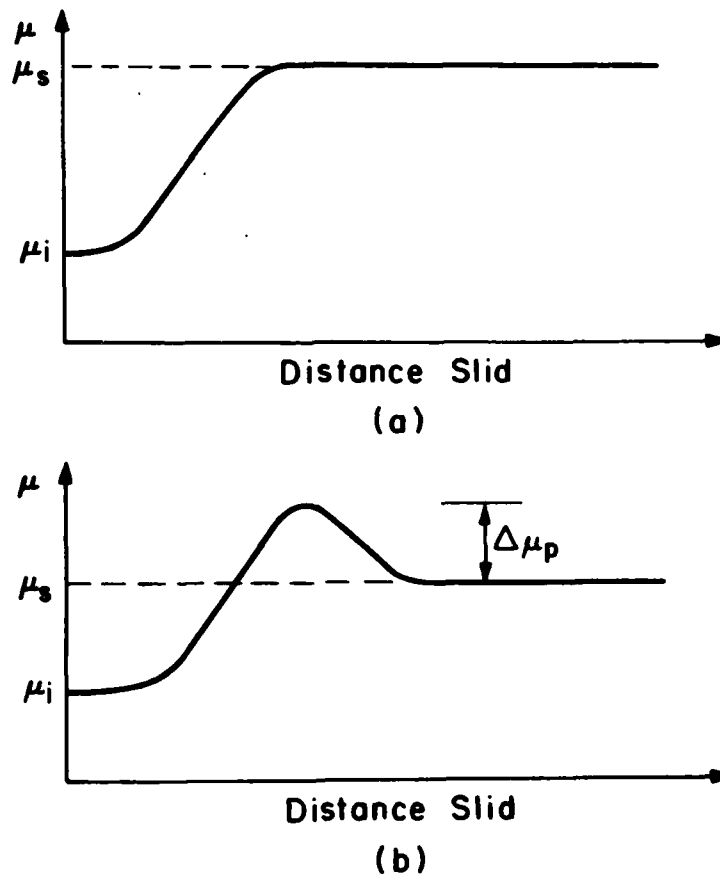
Fig. 2.3 Coefficient of friction vs. sliding distance: (a) for an Armco iron slider sliding against an Armco iron specimen (μ_i = 0.13, μ_s = 0.71); (b) for an AISI 1095 steel slider sliding against an Armco iron specimen (μ_i = 0.17, μ_s = 0.51, $\Delta\mu_p$ = 0.25).

(2) When wear particles are brushed from the sliding interface, the coefficient of friction decreases to a low value and gradually reaches a steady state value again, as schematically illustrated in Fig. 2.4. (The effect of wear particles on the friction coefficient was also reported by Abrahamson et al. [30] and more recently by Kuwahara and Masumoto [45].

(3) The coefficient of friction can differ by as much as 0.2 even for the same pair of materials (which are chemically identical) depending on which is a stationary slider and which is a moving specimen (see Table 2.2).

(4) The initial value of the kinetic coefficient of friction μ_i is in the neighborhood of 0.1 to 0.2 (but largely in the range of 0.12 to 0.17) for many materials tested, i.e., gold on gold, steel on steel, brass on steel, etc. [3, 44], and also regardless of whether or not lubricants are used.

(5) When the friction test is done with extremely well polished surfaces, plowing grooves are formed from the onset of testing (see Figs. 2.5 and 2.6).

2.4 Postulated Genesis of Friction

The experimental results clearly indicate that the observed friction coefficients cannot be explained in terms of the adhesion theory alone. The effect of entrapped wear particles and the existence of μ_i which is independent of environmental conditions and materials tested cannot be explained by the adhesion theory. The theory is further defied by the dramatic changes in the coefficient of friction when the role of the slider and the specimen is reversed.
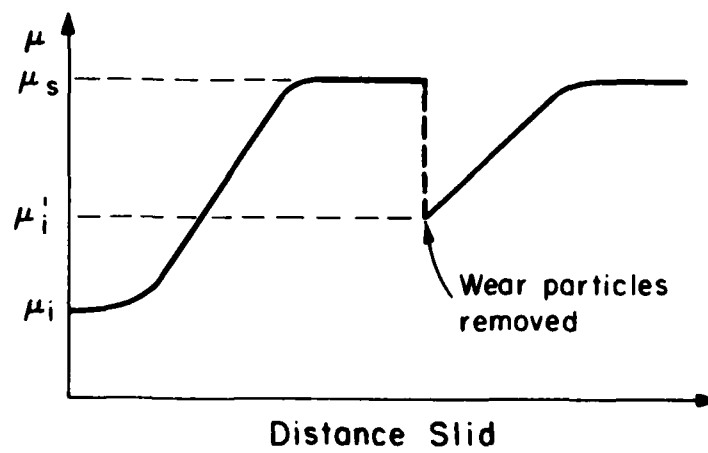
Fig. 2.4 Effect of removing wear particles for an Armco iron slider
sliding against an Armco iron specimen (μ_i = 0.13, μ_s = 0.71,
μ_i' = 0.4).

5 μm

Fig. 2.5 Typical wear track of an iron disk after 1 revolution of sliding
(3 cm): lubricated test in air; load - 400 g [Ref. 43].

Fig. 2.6 Typical wear scar of an iron pin after 1 revolution of sliding:
lubricated test in air; load = 400 g [Ref. 43].

Based on the experimental results discussed in the preceding
section the following postulate is advanced to explain the genesis of
friction between the sliding surfaces:

"The coefficient of friction between the sliding surfaces
is due to the various combined effects of asperity
deformation, μ_d, plowing by wear particles and hard
surface asperities, μ_p, and adhesion between the flat
surfaces, μ_a. The relative contribution of these components
depends on the condition of the sliding interface, which is
affected by the history of sliding, the specific materials
used, the surface topography and the environment."

In this section this postulate will be described further.
Quantitative analysis of each of these friction components is given in
later sections from a theoretical point of view.

In order to clarify the above postulate, the time dependent behavior
of friction will be considered qualitatively by sub-dividing it into
the following stages (see Fig. 2.7).

(a) Stage I -- In this early stage the coefficient of friction
seems to be dictated by plowing of the surface by asperities. Adhesion
does not play any significant role in this state due to the contaminated
nature of the surface. The deformation of asperities does take place
at the onset of sliding which affect the static coefficient of friction.
However, it appears that in Stage I, asperity deformation is not the
major factor that determines the coefficient of friction, since they
deform as soon as sliding commences and the surface is easily polished
with the generation of new asperities in Stage I (see Fig. 2.8).
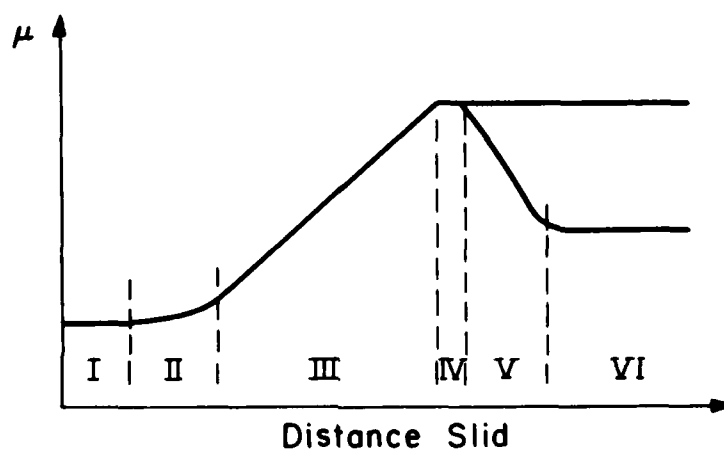
Fig. 2.7 Six stages in the frictional force vs. distance
slid relationship.
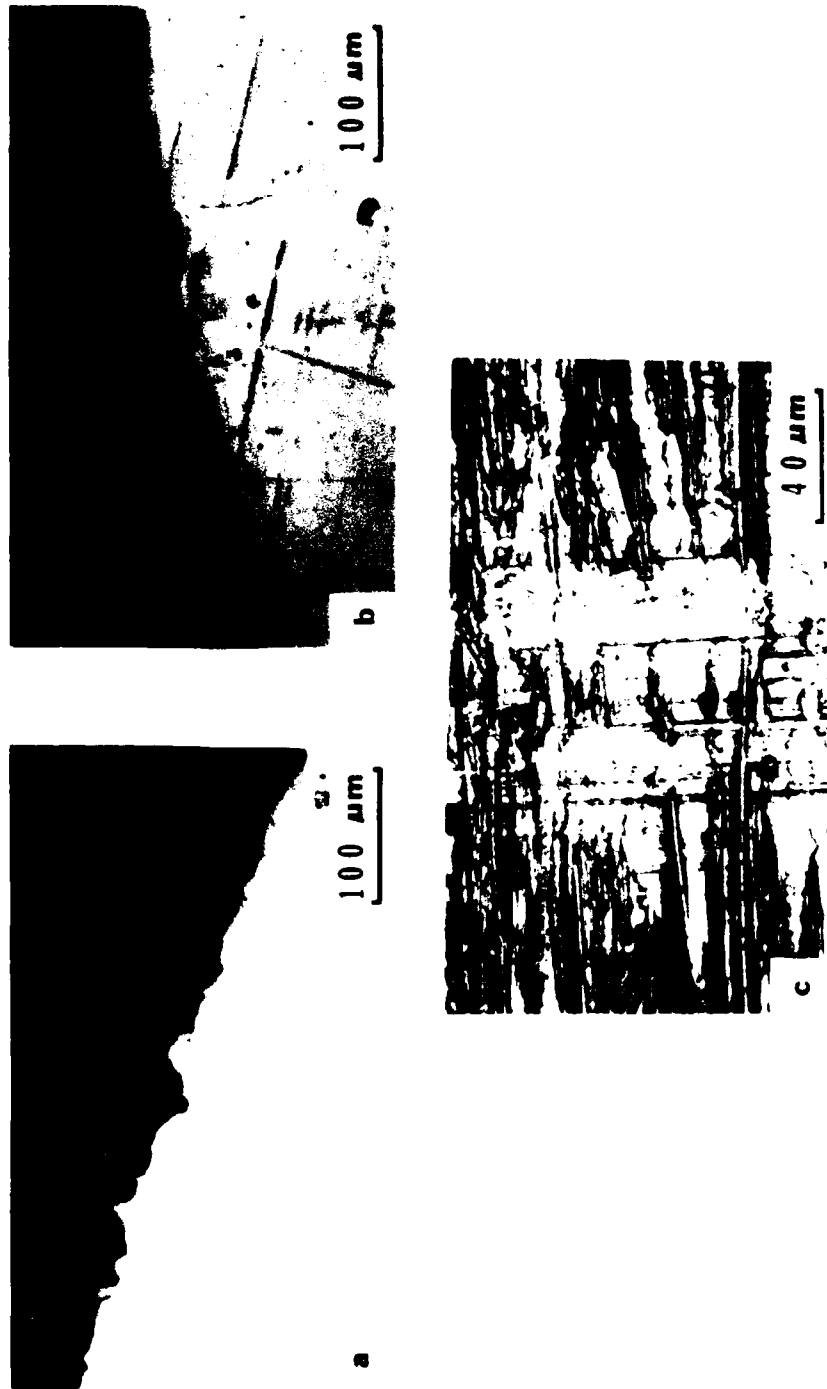
Fig. 2.8 Deformation of rough asperities on 1020 steel specimen: (a) initial surface; (b) after 1 revolution; (c) surface appearance.

Consequently the coefficient of friction in this state, μ_i, is largely independent of material combinations, the surface conditions and the environmental conditions.

(b) Stage II -- In this second stage, the frictional force begins to rise slowly due to increase in adhesion. When the interface is lubricated, Stage I persists for a long time and Stage II may not be present. The slope in Stage II can be steeper if the wear particles generated by the asperity deformation and fracture are entrapped between the sliding surfaces and plow the surfaces.

(c) Stage III - This stage is characterized by a steep increase in slope due to the rapid increase in the number of wear particles entrapped between the sliding surfaces as a consequence of higher wear rates. The slope can also be affected by the increase in adhesion due to the increase in clean interfacial areas. The force required to deform the asperities will continue to contribute to the frictional force in this stage as long as surface asperities are present. The wear particles are generated when the process of wear particle formation by subsurface deformation, crack nucleation and crack propagation postulated by the delamination theory of wear [2] is completed. Some of the wear particles get entrapped between the surfaces, causing plowing. The plowing will be greater when the wear particles are entrapped between metals of nearly equal hardness, because they will penetrate into both surfaces, preventing any slippage between the particle and the surface.

(d) Stage IV - This stage is reached when the number of wear particles entrapped between the interface remains constant. This occurs

when the number of the newly entrapped particles equal the number of entrapped particles leaving the interface. The adhesion contribution to friction also remains constant in Stage IV. The asperity deformation is not as important as plowing since the asperities deform readily and reach the equilibrium state in shape which is independent of the initial surface roughness. When two like metals are slid against each other or when the mechanism responsible for Stage V does not play a significant role, the coefficient of friction in Stage IV is the steady state frictional coefficient between the two metals.

(e) Stage V -- In some cases, such as when a very hard stationary slider is slid against a soft specimen, the asperities of the hard surface are gradually removed, creating a mirror finish as shown in Fig. 2.9. In this case the frictional force decreases due to the decrease in plowing and asperity deformation. Plowing decreases since wear particles cannot anchor on a polished hard surface.

(f) Stage VI -- Eventually when the hard surface becomes a mirror smooth to a maximum extent, the softer surface also acquires the same mirror finish and the frictional force levels off. The surfaces are never completely smooth since there are always "pot holes" due to the creation of delamination wear particles. These craters provide anchoring points for wear particles. When the hard surface is not stationary but moving against the softer surface, the hard surface remains rough, probably because polishing cannot take place due to geometric reasons. In this case, Stages V and VI are not present.

Mirror
Finish

Craters ("Pot holes")
due to the
Wear Sheet Formation
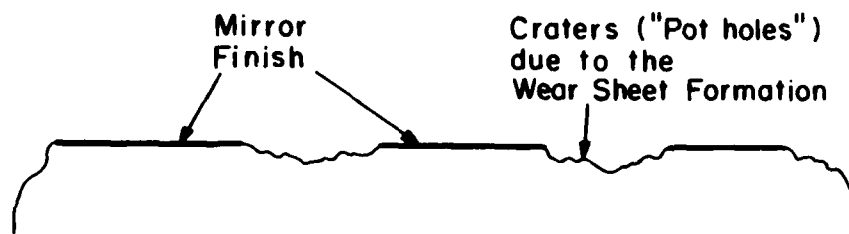
Fig. 2.9 A hard stationary surface polished by a soft surface.

2.5 Analysis of the Friction Generating Mechanisms

The three basic mechanisms (i.e., asperity deformation, plowing
and adhesion) that are responsible for the generation of friction will
be analyzed in this section. The asperity deformation initially deter-
mines the static coefficient of friction. Also, it affects the dynamic
coefficient of friction, since asperities are continuously generated
due to delamination of wear sheets. However, the contribution of the
asperity deformation to the dynamic coefficient of friction is not large
relative to those by plowing and adhesion, since the asperities deform
readily (perhaps in one asperity contact), whereas the generation of
asperities has to await the formation of delamination wear particles
which often requires a large number of cyclic loading by the asperities
of the opposing surface. On the other hand, plowing takes place con-
tinuously whenever wear particles are entrapped between the sliding
surfaces or when the asperities of the counterface plow in all cases
when clean flat surfaces come into contact during steady state sliding.
The relative magnitude of these components will be determined approxi-
mately by using the slip-line field.

2.5.1 Analysis of the Asperity Deformation, μ_d

Consider the two representative asperities approaching
toward each other as shown in Fig. 2.10. When these asperities come
into contact with each other, they have to deform in such a manner
that the resulting displacement field is compatible with the sliding
direction and that the sum of the vertical components of the surface
traction at the contacting asperities must be equal to the applied
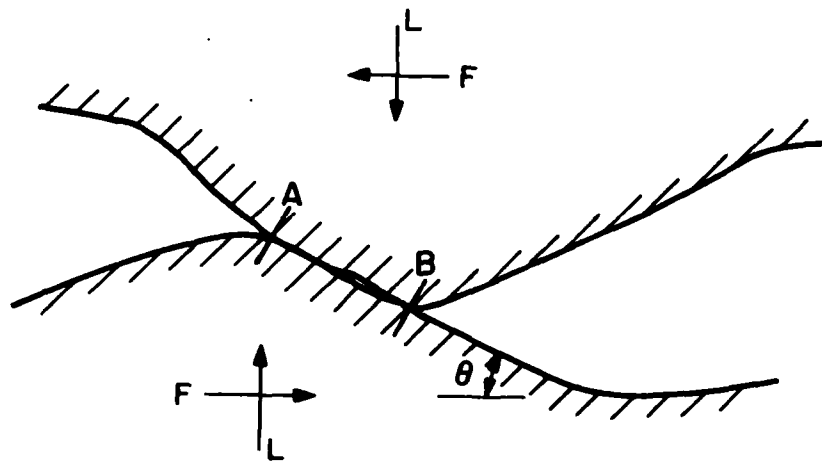
Fig. 2.10 Two interacting surface asperities.

normal load. A possible slip-line field that satisfies the kinematic
condition is given in Fig. 2.11. The solution demands that the shear
stress along OA be whatever is necessary to satisfy the condition that
$\alpha = \theta$, which is necessary to constrain the resulting deformation in
the sliding direction. This would be possible even under the lubri-
cated conditions if the interface OA is not perfectly smooth but rough
enough to allow mechanical interlocking. The derivation of the normal
and tangential force corresponding to the slip-line field shown in
Fig. 2.11 is given in Appendix A.

The general solution is sketched in Fig. 2.12. If it is assumed
that the asperity deformation is the only phenomenon that takes place
at the interface and is entirely responsible for the frictional force
under a given load, the coefficient of friction due to asperity deform-
ation μ_d varies from 0.39 to 1 as the slope of asperities increases
from 0 to 45°. These values are closer to the static coefficient of
friction than the dynamic friction coefficient measured during the
early stage of sliding, i.e., Stage I [46].

In dynamic situations most of the normal load is carried by the
entrapped wear particles and the flat contacts. Therefore, the actual
contribution of the asperity deformation to the frictional force is
expected to be a small fraction of the estimated value. This may be
estimated indirectly from experimental results, as discussed later in
this chapter.

It should be noted that the slip-line analysis done to determine
μ_d is not very different from those of Green [13], who presented
similar solutions to justify the adhesion theory by considering the
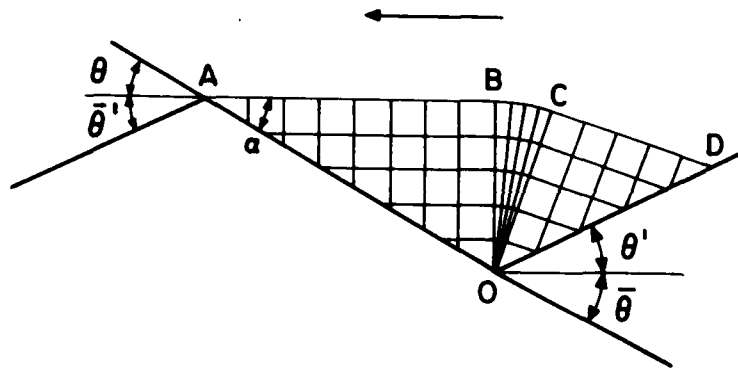
Fig. 2.11 A geometrically compatible slip-line field. It can be seen that $\theta > \bar{\theta}$, $\theta' > \theta$, and $\theta = \alpha$.
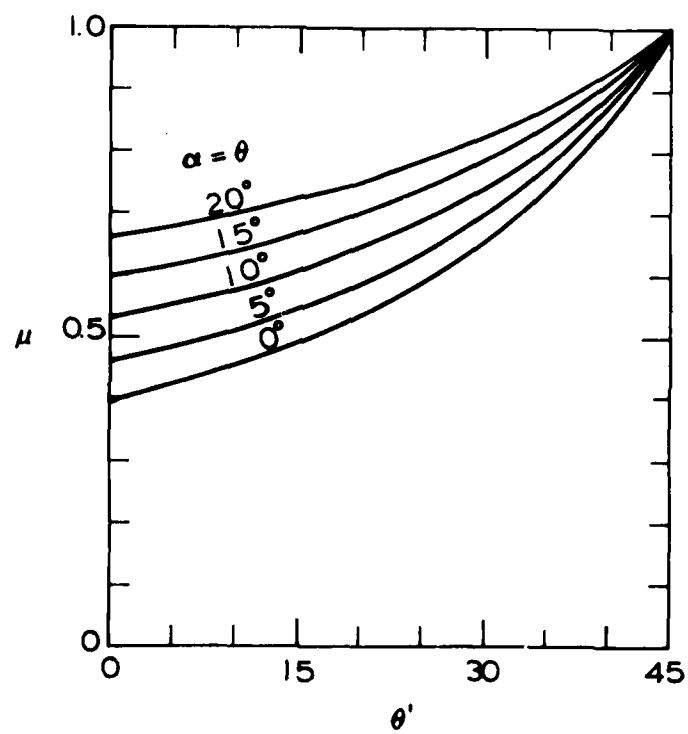
Fig. 2.12 Slip-line field solution for friction as a function
of the slope of asperities.

deformation of asperities under the influence of the load exerted by welded asperity junctions of various strengths. An important difference, however, is that in the analysis presented in this chapter the asperity deformation is assumed to be governed by the kinematic considerations regardless of the nature of bonding between the contacting asperities. Therefore, μ_d does not depend sensitively on adhesion and represents the frictional force due to the deformation of all interacting asperities. Before the onset of sliding between two surfaces μ_d determines the static coefficient of friction.

2.5.2 Analysis of Adhesion Component of the Friction Coefficient, μ_a

A frictional force can arise due to the adhesion of two nearly flat surfaces. Unlike the deformation of asperities this frictional force is a function of the adhesion between the two opposing surfaces. The adhesion force arises either due to the welding of two nearly flat portions of the surface or when the atoms are brought together to close proximity for interatomic interactions but without welding. The adhesion at the slopes of two interacting asperities may be neglected in this analysis since they have already been considered in deriving in μ_d. Also they are kinematically constrained deformations, being independent of the quality of adhesion.

Experimental results show that μ_a is not present (or is at least negligible) at the onset of sliding, probably due to the presence of contaminants on the surface. With the deformation of asperities and exposure of fresh new surfaces the adhesion between nearly flat surfaces is expected to increase. The exact adhesion area cannot be determined

a priori, since the applied normal load may also be carried by inter-
acting asperities and entrapped wear particles, although the limiting
cases can be analyzed.

Consider two nearly flat surfaces coming into contact as shown
in Fig. 2.13. (Sometimes this type of contact is called a "rubbing"
contact). Depending on the nature of adhesion along the interface ED,
the force required to move the interacting surfaces with respect to each
other will vary. When there is no adhesion the force will be zero and
when there is complete adhesion it will reach a maximum. The solution
to this problem can be obtained again using the slip-line fields
similar to that shown in Fig. 2.13. The exact geometric shape of the
slip-line field will depend on the boundary condition at ED. The
solution sought can be adapted from the recent work of Challen and
Oxley [19] who derived an expression for the friction coefficient as

$$\mu_a = \frac{A \sin \alpha + \cos (\cos^{-1} f - \alpha)}{A \cos \alpha + \sin (\cos^{-1} f - \alpha)} \tag{2.1}$$

where

$$A = 1 + \frac{\pi}{2} + \cos^{-1} f - 2\alpha - 2 \sin^{-1} \frac{\sin \alpha}{\sqrt{1-f}} \tag{2.2}$$

f = strength of the adhesion at ED as
    expressed at a fraction of the shear
    flow of strength of the softer material

α = the slope of the hard asperity
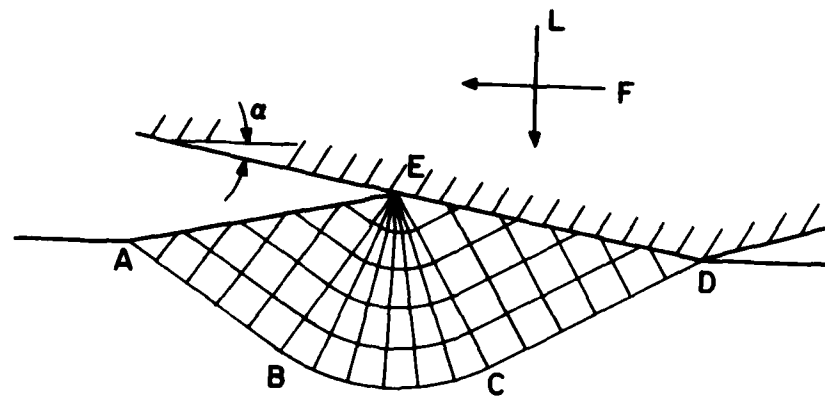
Fig. 2.13 A slip-line field for a rubbing contact.

For nearly flat surfaces $\alpha \to 0$. Therefore, Eqs. 2.1 and 2.2 reduce to

$$\mu_a = \frac{f}{A + \sin(\cos^{-1} f)} \tag{2.3}$$

$$A = 1 + \frac{\pi}{2} + \cos^{-1} f \tag{2.4}$$

μ_a varies from 0 to 0.39 as f changes from 0 to 1.

The friction coefficient determined by Eqs. 2.1 and 2.2 are based on the assumption that all the applied normal load is carried by the flat interfaces. However, since part of the normal load is also carried by purely elastic contacts, the interacting asperity junctions discussed in the preceding section, and the entrapped wear particles, μ_a under typical sliding conditions should be less than 0.4. The experimental results obtained with the hard AISI 1095 steel slider and the soft Armco iron specimen showed that the steady state coefficient of friction reached a value of 0.51 when both surfaces were polished smooth and thus the friction was caused primarily by adhesion. The agreement between the theory and the experiment is reasonable since asperity interactions and plowing by wear particles must have also contributed to the frictional force.

2.5.3 Analysis of Plowing, μ_p

The plowing component of the frictional force can be due to the penetration of hard asperities or due to the penetration of wear particles. The plowing due to wear particles is schematically

illustrated in Fig. 2.14. When two surfaces are of equal hardness, the particle can penetrate into both surfaces. As the surfaces move with respect to each other, grooves will be formed in one or both of the surfaces. When one of the surfaces is very hard and smooth, the wear particle will simply slide along the hard surface and no plowing can occur. However, when the hard surface is very rough, wear particles can anchor in the hard surface and plow the soft surface.

The friction due to plowing was investigated by Sin et al. [47], who showed that the contribution of plowing to the friction coefficient is very sensitive to the ratio of the radius of curvature of the particle to the depth of penetration. The plowing force may be expressed as $P = pA_g$, where A_g is the cross-sectional area of the grooved track and p the flow stress. Considering that the contact interface is only on the front half of the particle [48], we may derive the expression for the friction coefficient by plowing μ_p as (Appendix B):

$$\mu_p = \frac{2}{\pi} \left[\left(\frac{2r}{w}\right)^2 \sin^{-1} \frac{w}{2r} - \left\{\left(\frac{2r}{w}\right)^2 - 1\right\}^{1/2} \right] \qquad (2.5)$$

where w is the width of the penetration and r is the radius of curvature of the particle. The ratio of w/r measured by sectioning the worn specimen is in the neighborhood of 0.8. Substituting this value into Eq. 2.5, the plowing coefficient of friction is found to be 0.2. This value is in the same range as the decrease in the friction coefficient observed by removing the wear particles from the Armco iron/Armco iron and Armco iron/AISI 1995 steel interfaces, which were 0.31 and 0.16
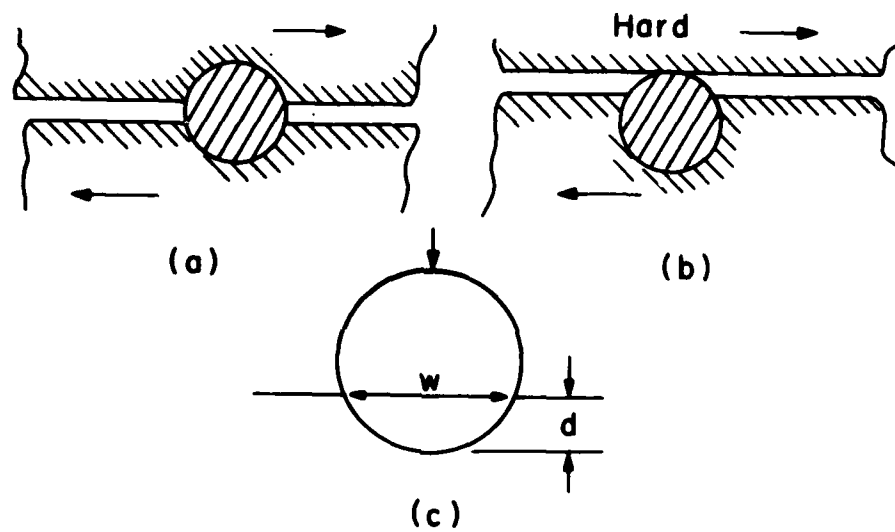
Fig. 2.14   Idealized model of wear particle interaction between
two sliding surfaces: (a) surfaces of equal hardness;
(b) one smooth very hard surface; (c) geometry of the
wear particle.

respectively. The range of possible values of μ_p as a function of the ratio w/2r is shown in Fig. 2.15.

Plowing not only increases the total frictional force and delamination wear, but also creates small wear particles which in turn affect the subsequent wear of sliding surfaces. Plowing action forms ridges along the sides of plowed grooves. When these ridges are deformed flat and subjected to repeated loading, some of these become loose wear particles with continued sliding. This is schematically illustrated in Fig. 2.16.

2.6 Relative Contributions of μ_d, μ_a, and μ_p to the Overall Frictional Behavior

If the postulate for friction coefficient presented in this chapter is correct, then the relative values of various friction components are as follows:

μ_d -- From 0.43 to 0.75 when the entire applied normal load is carried by typical surface asperities with a slope of 4° to 20°. It appears that μ_d is responsible for the static coefficient of friction, but does not contribute to the initial coefficient of friction μ_i in Stage I. The reason μ_d is not a major factor in Stage I is that once the original asperities deform asperity interactions cannot take place. This friction component can contribute partially to the steady state coefficient of friction if new asperities are continuously generated as a consequence of delamination wear process.

63
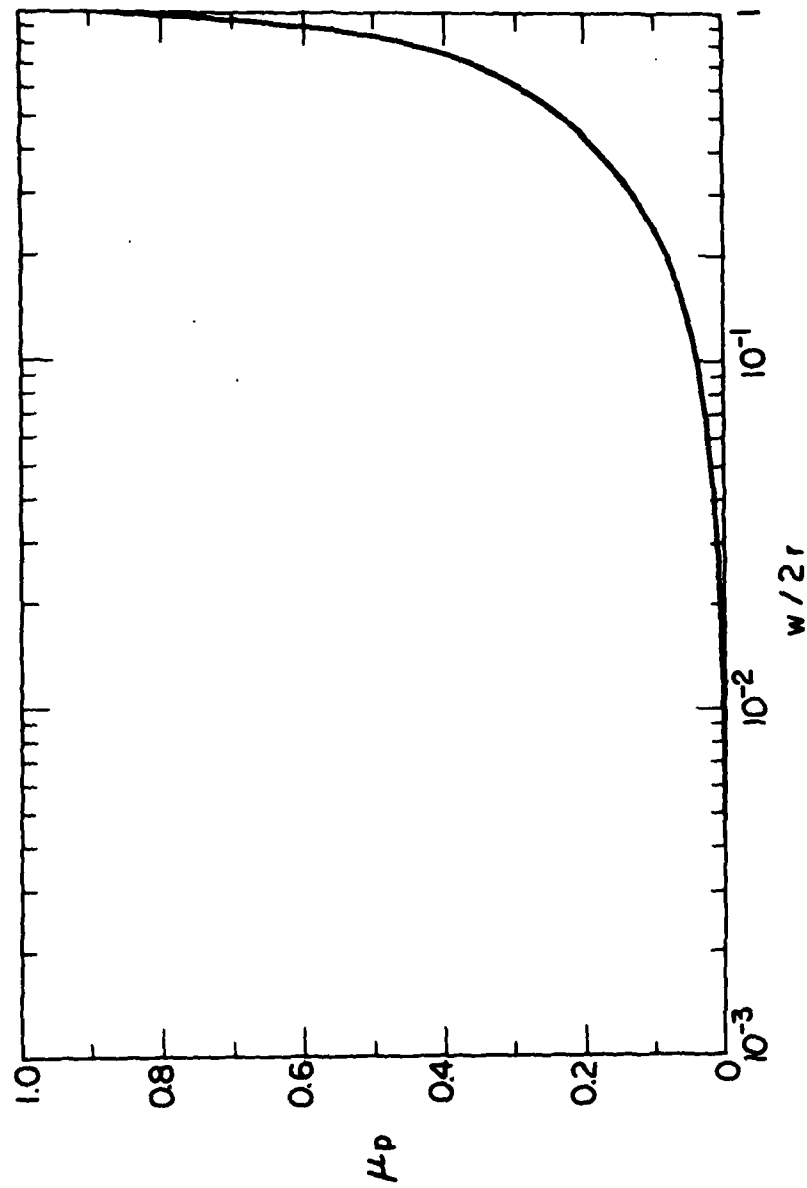
Fig. 2.15 Plowing component of the friction coefficient as a function of the ratio of the width to the diameter of the entrapped wear particle.

Groove

(a)

Wear particle associated
with plowing

(b)
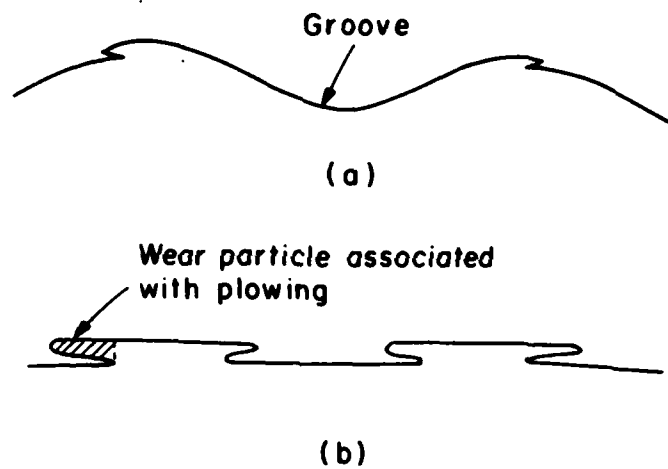
Fig. 2.16 Schematic illustration of wear particle formation due
to plowing: (a) ridges formed along the sides of the
plowed groove; (b) flattened ridges.

μ_a -- From about 0 to 0.4 depending on the nature of adhesion between the flat part of the interacting surfaces. The low value is for a well lubricated surface with light lubricant, while the high value is for identical metals sliding against each other without any surface contaminants and oxide layers.

μ_p -- From nearly 0 to 1.0 from a theoretical point of view depending on the depth of penetration, but normally less than 0.4 in a typical situation. The high values are associated with two identical metals sliding against each other with deep penetration by wear particles, while the low value is obtained when either wear particles are totally absent from the interface or a soft surface is slid against a hard surface with a mirror finish.

The determination of the total friction coefficient in a given condition can be rather complex. It is difficult to determine the relative contributions of μ_d, μ_a and μ_p to the total frictional coefficient, because analyses for μ_d and μ_a were done assuming that the total normal load is carried by either asperities or flat contact areas. In real situations the normal load will be apportioned among the asperity contacts, flat adhesion junctions, and the entrapped particles. However, it is quite plausible in many real situations that each one of these mechanisms which contribute to friction can take place sequentially rather than concurrently. Consider, for example, a flat junction and an asperity in contact as shown in Fig. 2.17. When the
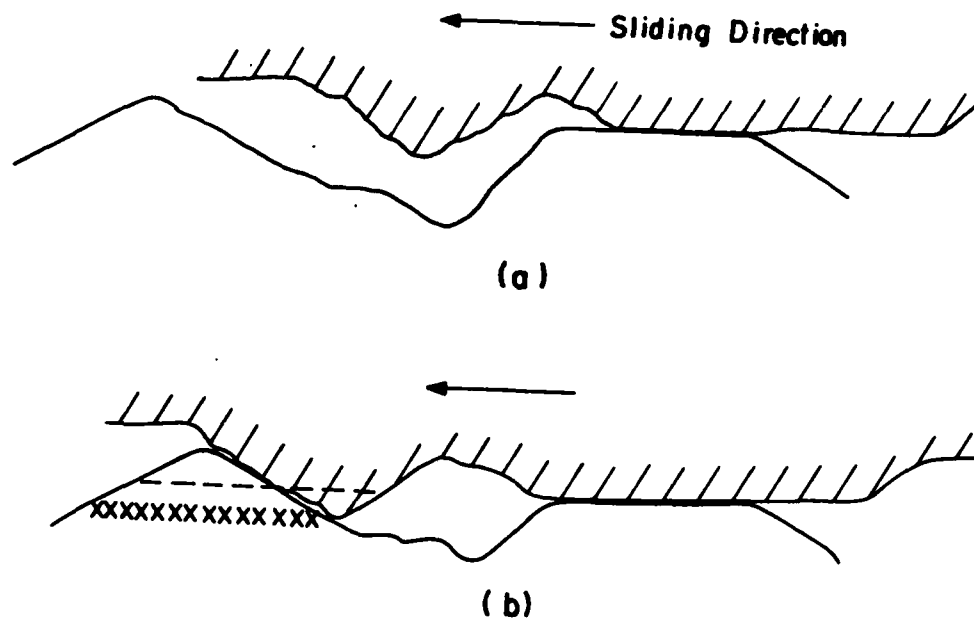
Fig. 2.17 Two sliding surfaces in contact: (a) first contact of flat surfaces; (b) flat surface contact and asperity contact.

flat areas come into contact first and form an adhesion junction, the analysis performed for μ_a is strictly valid. When the asperities also come into contact with further sliding, a large fraction of the normal load is still carried by the flat junctions due to their higher normal "stiffness," i.e., the force required to cause unit displacement along the vertical direction. In this case in order to continue the sliding action the asperities will simply have to shear along the dotted line if the materials are identical or along the crossed line if the top slider is much harder than the bottom slider. In this case only a tangential force is required to deform the asperity plastically along the direction of sliding.

The coefficient of friction μ is represented in a "Friction Space" as a function of adhesion, plowing and roughness as shown in Fig. 2.18. The adhesion is expressed in terms of the non-dimensional interfacial shear strength f of the flat contacts which was defined by Eq. 2.2. The roughness is plotted in terms of the slope of the surface, while the plowing is given in terms of the ratio of the width of wear particle (or hard asperity) penetration to its radius. The lowest surface corresponds to the the case of no asperities, i.e., $\theta = 0$, which forms the lower bound. The θ_i surface corresponds to the initial machined surface, while the θ^* surface represents the surface roughness when the peak of μ occurs. As the surface gets rougher and/or the number of the steady state asperities increases, μ will increase and the friction value will move in the Friction Space along the μ-axis. The friction surfaces θ^* is plotted from the actual experimental results obtained with Armco iron sliding against AISI 1095 steel.
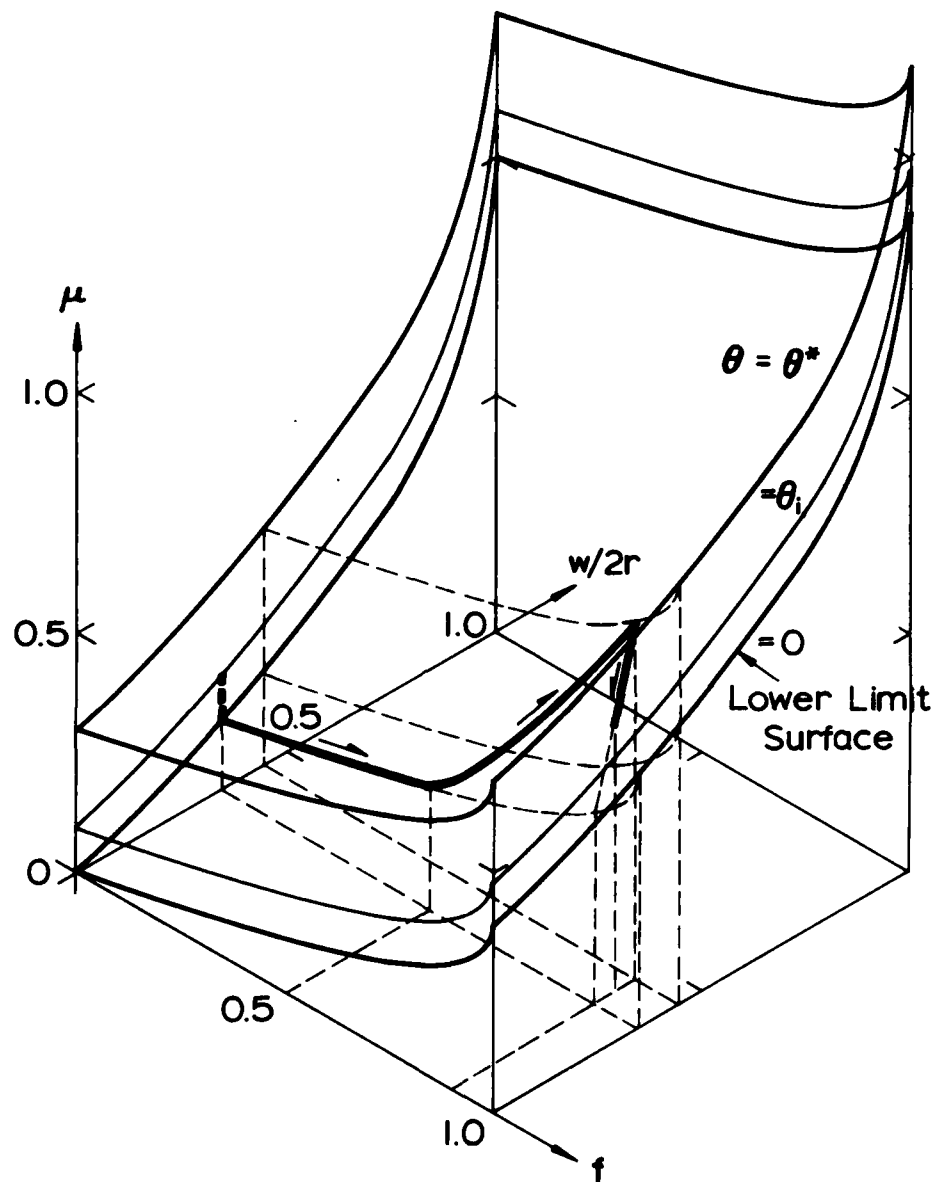
Fig. 2.18 "Friction Space" showing the coefficient of friction as a function of adhesion between flat contacts, wear particle penetration, and surface roughness: $f = \tau_s/k$, where τ_s is the shear stress at the interface and k is the shear flow strength of the soft metal; θ is the slope of asperities; w/2r is the ratio of the width of asperity penetration to the diameter of the particle.

In this case, the asperity contribution to friction was 0.3

Although this figure is not precise, it gives a reasonable picture of what happens in a given situation. The paths of the friction coefficient change shown in Fig. 2.3 are shown in this Friction Space in Fig. 2.18. The friction is shown to start from the initial roughness plane θ_i to nearly flat surface, i.e., $\theta = 0$ and traces along the paths indicated in Fig. 2.3. In many cases the θ_i surface may be above the $\theta*$ friction space, depending on the initial surface finish relative to the steady state surface roughness.

The foregoing argument may be applied to the specific case of gold sliding against gold. When unlubricated gold specimens without any oxide layer are slid against each other, the frictional force is due to the sum of μ_a and μ_p or the sum of a fraction of μ_d, μ_a and μ_p, depending on the situation. It is most likely that the μ_a term will always be present since two flat surfaces in contact may be the most stiff system in supporting the normal load. For example, if the normal load is first borne by flat contacts only, friction will be entirely due to adhesion, μ_a, which will reach a maximum value. Then if asperities of the opposing surfaces come in contact, an additional frictional force will be required to deform the asperities. In addition to these frictional forces the third frictional component may also affect the frictional behavior if the wear particles become wedged in between the sliding surfaces. Therefore, the coefficient of friction between gold on gold may be as high as 1.4 to 1.6 and fluctuate between a maximum and a minimum value.

Lubricated surfaces can have a coefficient of friction whose magnitude will be determined by the degree of plowing and asperity interaction. Lubricated surfaces without any asperities are found to have a coefficient of friction of approximately 0.04 for a hard surface and 0.12 for a soft iron surface. However, when wear particles are entrapped between the sliding surfaces, the plowing component of the frictional force can be present raising the friction coefficient.

In the past the high friction coefficient between like metals has been explained in terms of greater adhesion due to their greater solubility [49]. However, the evidence presented in this paper shows that the so-called compatibility of metals is dictated more by their mechanical behavior rather than by their chemical behavior. This is quite reasonable since the diffusion rate at the typical sliding junctions is so low due to its low temperature that the solubility between the metals cannot account for the observed wear rates [50].

In their classical book on tribology, Shaw and Macks also considered the possibility that the frictional behavior is affected by the asperities, plowing and adhesion. However, the details of the mechanisms proposed in this paper and their work differ substantially. In their book, the asperity was assumed to increase the friction due to the vertical motion of asperities as they slide over each other; the plowing of the sliding surfaces by wear particles was not considered and the importance of the penetration depth was not specifically included; the adhesion, plowing and asperity contributions were assumed to be always constant; and the sliding distance dependent phenomenon was not considered. The work reported in this paper clearly shows

(or hypothesizes) that the adhesion between sliding surfaces is not always present; that the deformation of asperity, rather than a simple sliding-over the asperities affects the frictional behavior, which is kinematically constrained; that wear particles affect the coefficient of friction more significantly than adhesion in many cases; and that the coefficient of friction is not a constant but rather moves about in the "Friction Space" during sliding.

2.7 Summary

The coefficient of friction is shown to be composed of three components: μ_d due to the deforming asperities; μ_p due to plowing by wear particles and hard surface asperities; μ_a due to adhesion. The contribution to the overall coefficient of friction by plowing and asperity deformation can be greater than that by adhesion, which has been largely ignored by the classical adhesion theory. Thus, to assess the effect of friction on crack propagation and therefore on wear all the mechanisms should be included to determine the load at each asperity contact.

3. THE LIMITATIONS OF THE LEFM APPROACH
TO SUBSURFACE CRACK PROPAGATION

3.1 Introduction

As reviewed previously five processes are involved in delamination wear: transmission of forces, deformation, crack nucleation, crack propagation, and wear sheet formation. The wear rate of material is generally determined by the slowest or rate controlling process among these steps. The recent work on the delamination theory of wear has suggested that in many engineering materials the critical process is crack propagaticn [36, 37, 41].

3.2 Crack Propagation Studies in the Past

Once cracks have been nucleated in the subsurface of sliding materials, they must propagate to produce wear sheets. Without crack propagation sheet-like wear particles may not form. The nucleation and growth of several cracks may be involved in the formation of a single wear sheet. Sometimes the growth and coalescence of a large number of neighboring voids will lead to the formation of a wear particle.

Fleming and Suh [37] have analyzed the propagation of a subsurface crack parallel to the surface using a linear elastic fracture mechanics (LEFM) model. This treatment was based on the fact that a subsurface crack is closed in the plastic region in front of the asperity contact and a portion of the crack is subjected to tensile stress in the elastic region behind the contact zone. The stress intensity factors were calculated by an elliptical distribution of loads at the contact using

an approximate method based on weighting factors. A model was
constructed for the correlation of fatigue crack propagation and wear
rates. However, the correlation is poor since the stress intensity
factors calculated are too low to cause crack growth.

Following the Fleming and Suh's work others such as Hills and
Ashelby [38] and Rosenfield [39] have attempted to apply the fracture
mechanics approach to wear. Both approaches are quite similar and they
used the slightly different boundary loading conditions from that of
Fleming and Suh. While Fleming and Suh concentrate on the tensile
stress zone right behind the contact, Hills and Ashelby and Rosenfield
consider the possibility of Mode II propagation of a crack in a com-
pressive field.

In considering a crack subjected to a combined shear-compression
stress they have assigned a friction coefficient between the crack
surfaces in a manner suggested by Swedlow [51]. In addition to stress
intensity calculation at a crack tip Hills and Ashelby have tried to
explain a possible mode of crack propagation under this condition fol-
lowing McClintock [52]. On the rail cracking problem McClintock has
used a boundary integral relaxation method to calculate the plasticity
at the tip of a small horizontal crack in the rail head. A wheel
passage was shown to give initial sliding, followed by locking,
sqeezing the plastic zone, reversed sliding, locking, and finally
unloading.

Recently, Keer et al. [40] have applied the integral equation
method to an elastic half-space containing a horizontal subsurface
crack and a surface breaking vertical crack. They were loaded by the

applied stress due to the asperity contact. Using these models they have assessed the tendencies of the cracks to propagate, to change direction, and to interact with each other. For a horizontal subsurface crack the cracks only in a tensile field have been studied.

Although the methods and the location of cracks in each study appear to be different, one thing is common: the predicted values of stress intensity factor are too low to cause crack growth. Since sub-surface delamination cracks appear to grow under combined shear-compression loads, it may not be relevant to relate to fatigue crack propagation rates in Mode I. However, the experimental data on Mode II and combined Modes I and II crack growth are not currently available for most materials. Nevertheless, it is unlikely that the loading condition would significantly change the crack propagation behavior. Moreover, a recent study by Ritchie [53] has shown that wear resistance in an ultra high strength steel (300-M) bears no direct relationship to crack propagation resistance, whereas a direct correlation is found with resistance to crack initiation. Therefore, it is still premature to relate subsurface crack propagation to fatigue crack propagation. At least following questions require further investigation:

   (1) The accuracy in the methods of stress intensity factor
        calculation.

   (2) The appropriateness of the linear elastic fracture mechanics
        (LEFM) approach in terms of plasticity aspect.

In this chapter the stress intensity factors will firstly be calculated using the finite element method. This will include the discussions on the criteria for crack growth under sliding and

compression and on the direction of extension of cracks. Then, the plasticity aspect at the crack tips will be considered to check the appropriateness of the LEFM.

3.3 Stress Intensity Factors by Finite Element Method

Various analytical techniques have been employed in recent years to determine stress intensity factors for through or edge cracks, and for cracks embedded in infinite or semi-infinite elastic solids. However, the analytical solutions are not available for most cracked surfaces except for a limited number of simple problems. Therefore, the finite element method is suggested as the best candidate for obtaining stress intensity factors, whenever exact solutions are not available.

The finite element method is one of the most powerful and rigorous techniques available in computing stress fields, especially when the load applied is arbitrary and the geometric shape is irregular. Since the method is conceptually simple, applicable to large classes of geometries, materials and loading conditions, and can be made quite accurate, finite element methods are rapidly adopted in structural analysis. The details of the method are described in the literature [54] and will not be repeated here.

3.3.1 Finite Element Model

3.3.1.1 Crack Tip Elements

Recently several authors have employed the 8-noded and 20-noded isoparmetric elements in near tip modeling of 2-dimensional and 3-dimensional cracks. Henshell and Shaw [55] and Barsoum [56] have

demonstrated that when the mid-side nodes in these elements are placed at the quarter point, the elements will have the inverse square-root singularity characteristic of linear fracture mechanics. The latter author used both the quadratic quarter point element and the triangular element formed by collapsing one side (Fig. 3.1), and showed that the triangular element leads to far better results.

Later it has been shown by Barsoum [57] that the triangular elements possess the same singularity in the interior as well as on the boundary. On the other hand, quadratic elements have the singularity only on the boundary. In addition, when two corner nodes and a midpoint node in an 8-noded element are collapsed in such a way that they initially are at the same location, but are allowed to spearate when the element deforms, then this element has a $1/r$ or $1/r + 1/\sqrt{r}$ singularity depending on whether the side-nodes are at the midpoints or at the quarter points.

The computational procedure for stress intensity factors by the finite element method is described in detail in Appendix C. It is shown that the stress intensity factors can directly be determined from the stresses calculated by the FEM when the triangular isoparametric elements with the mid-size nodes placed at the quarter point position are employed as crack tip elements. In this method both near tip stress fields for the crack tip element and for the theoretical stress function are compared.

3.3.1.2 Finite Element Meshes

The model used for sliding wear study is that of an infinite half-plane, two-dimensional solid in plane strain, loaded by
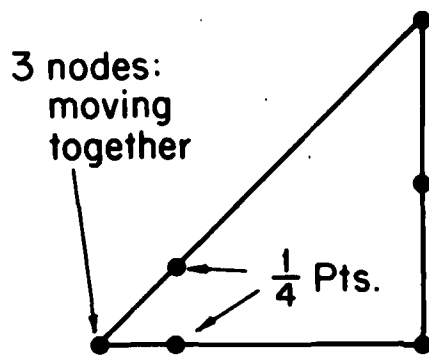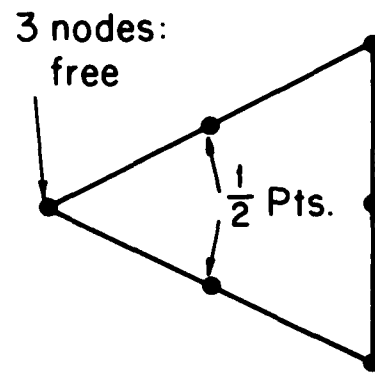
Fig. 3.1 Singular finite elements.

a stationary, rigid and straight-sided asperity. A cutout of the semi-infinite plane along ABCD was used (Fig. 3.2). The material and loading constants used were as follows: Young's modulus, $E = 1.96 \times 10^5$ MPa = 2×10^4 kg/mm^2; Poisson's ratio, $\nu = 0.28$; maximum normal stress applied, $P_o = 980$ MPa = 100 kg/mm^2. This material corresponds to steel.

Fig. 3.3 shows the geometry of the problem where a crack of length 2c lies parallel to the sliding direction of the asperity contact of length 2a and below the surface at a depth of d. Three different values of crack length were studied: c = 1/4a, a, 3a. Figs. 3.4 to 3.6 show the finite element meshes for each case containing 154 elements and 498 nodes, 146 elements and 414 nodes, and 144 elements and 488 nodes, respectively.

3.3.2 Results of Finite Element Calculation

In order to investigate the effects of asperity contact moving along the surface on subsurface cracking, a number of parametric study was conducted. For the cases of c = 1/4a and 3a shown in Figs. 3.4 and 3.6, respectively, the depth of crack, d, and the friction coefficient, μ, at the asperity contact were varied under the moving asperity contact.

When a crack is located in a tensile field, it is expected to open as described by Fleming and Suh [37]. The displacement field calculated for the case of c = a shown in Fig. 3.5 shows that the crack is really in opening mode. If the asperity moves to left, then part of the crack surfaces will tend to contact each other. When this happens a special treatment for crack faces is required. Without any constraint along
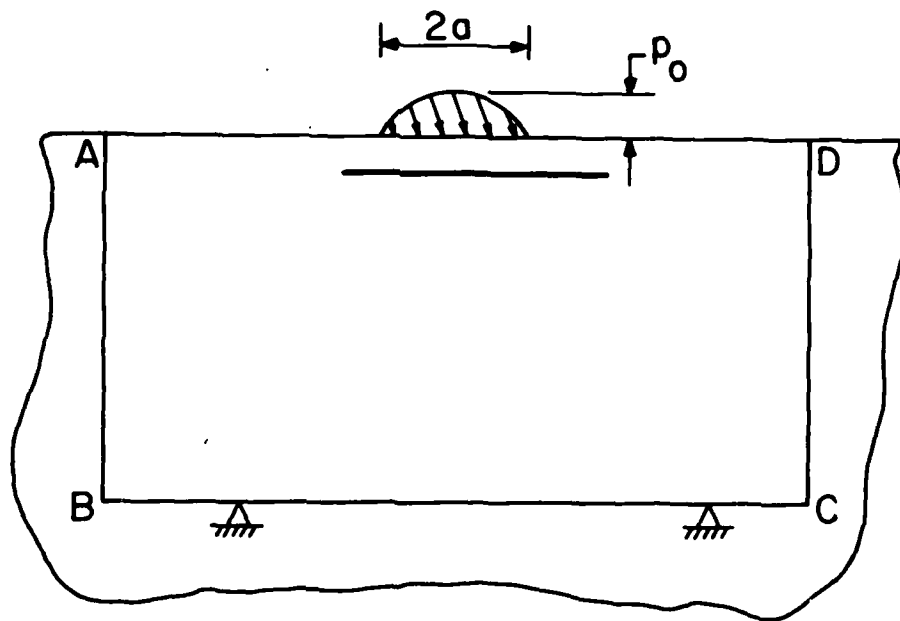
Fig. 3.2 A model of a subsurface crack in sliding contact used for the finite element analysis.
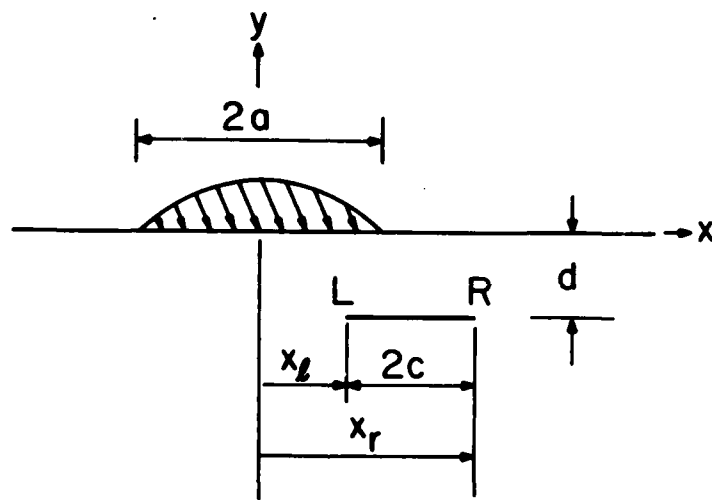
Fig. 3.3 Geometry of the problem.
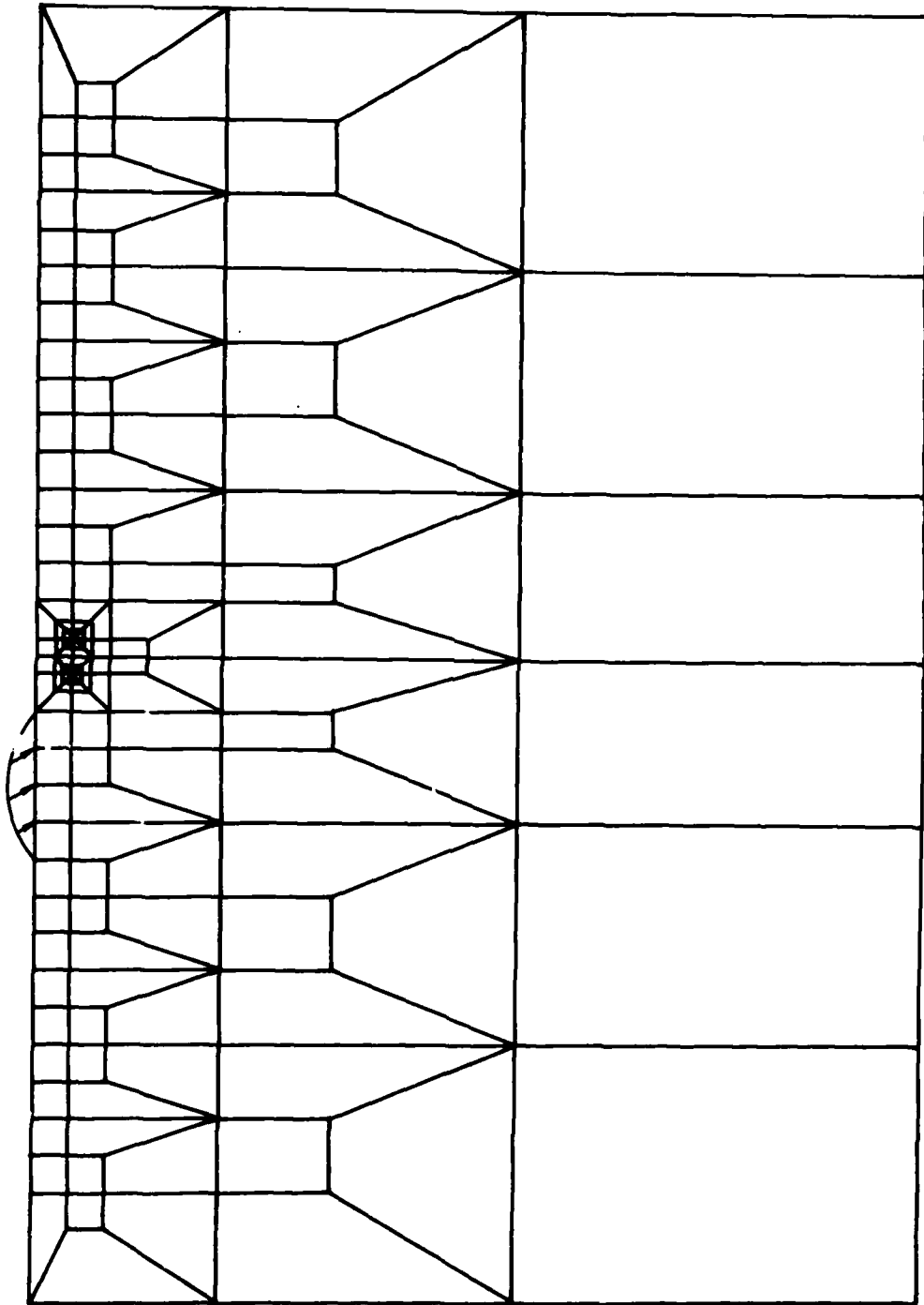
Fig. 3.4 Finite element mesh for c = 1/4a.
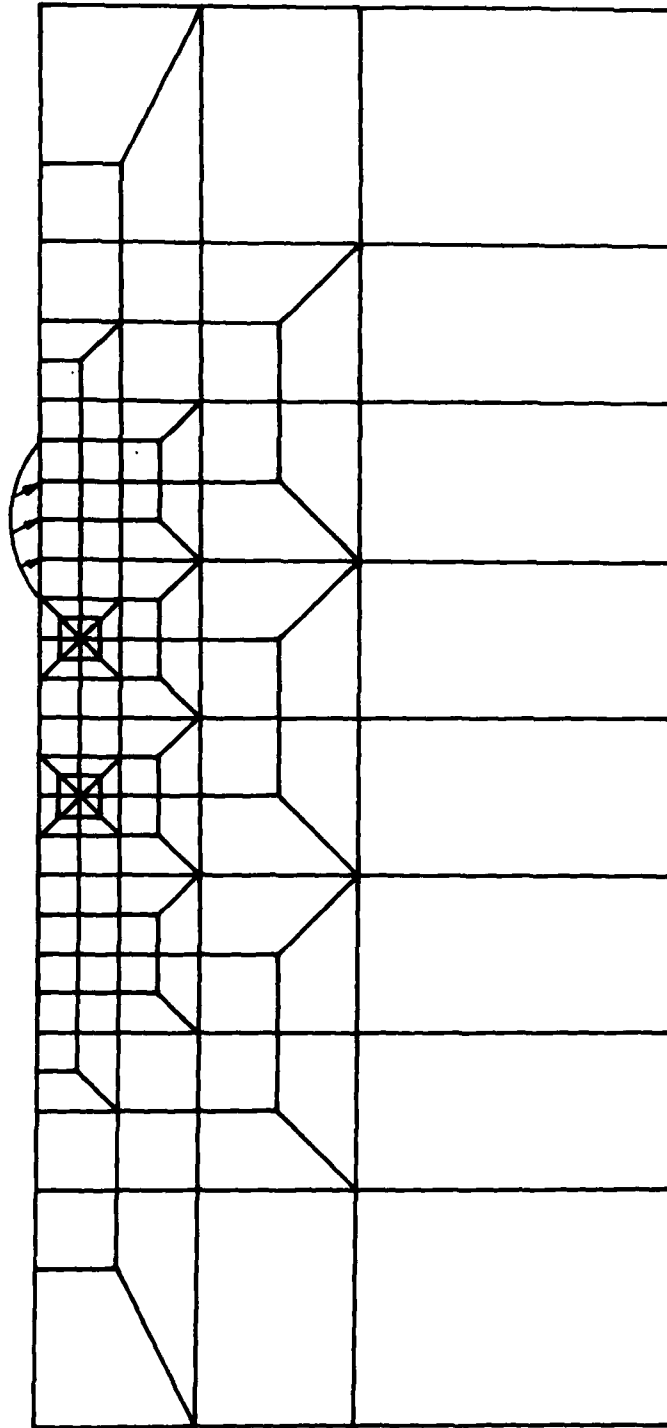
Fig. 3.5 Finite element mesh for c = a.
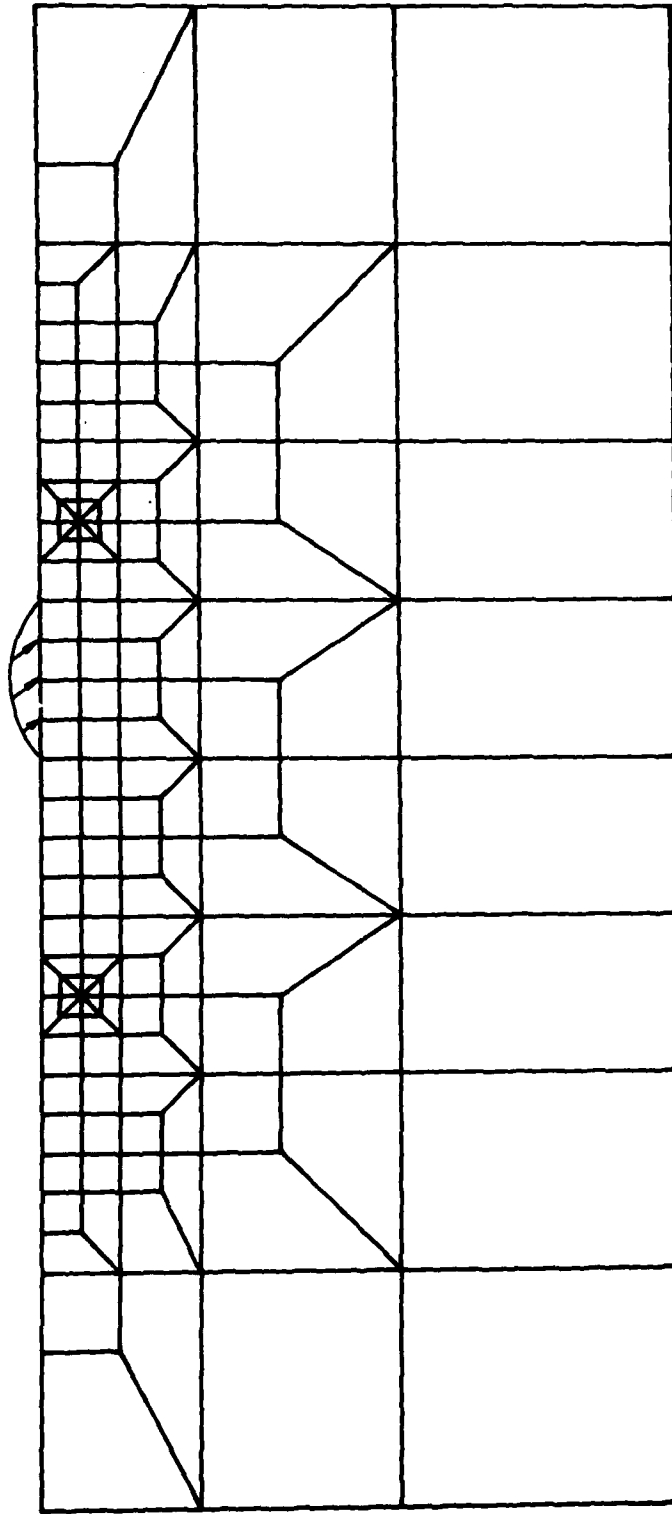
Fig. 3.6 Finite element mesh for c = 3a.

the crack, the upper surface will displace down below the lower surface when loading since the material over the crack is connected to the whole body only at both ends of the crack. To prevent this, the vertical displacements of the upper crack surface were constrained lest it should move down below the lower face. Although we may impose the friction boundary condition along the crack surfaces (see Appendix D), only the displacement boundary condition was considered in the study.

In Figs. 3.7 to 3.18 the Mode II stress intensity factors for $c = 1/4a$ and $3a$ are plotted as a function of crack tip location. For a given depth of crack K_{II} increases to reach some maximum value and then decreases as the asperity moves towards the right. From the figures the following results can be deduced:

(1) The maximum values of K_{II} occur when the crack tips lie right below the asperity contact.

(2) The closer the crack is to the surface, the larger become the maximum values of K_{II}.

(3) A longer crack has larger values of K_{II}.

These results cannot directly be compared with the results of Keer et al. [40] since they have studied cracks only in a tensile region for subsurface horizontal cracks. Nevertheless, their results show that cracks even in the tensile region have the same properties as those of (2) and (3) listed above. However, this study indicates that cracks in the tensile region have much smaller values of K_{II}.
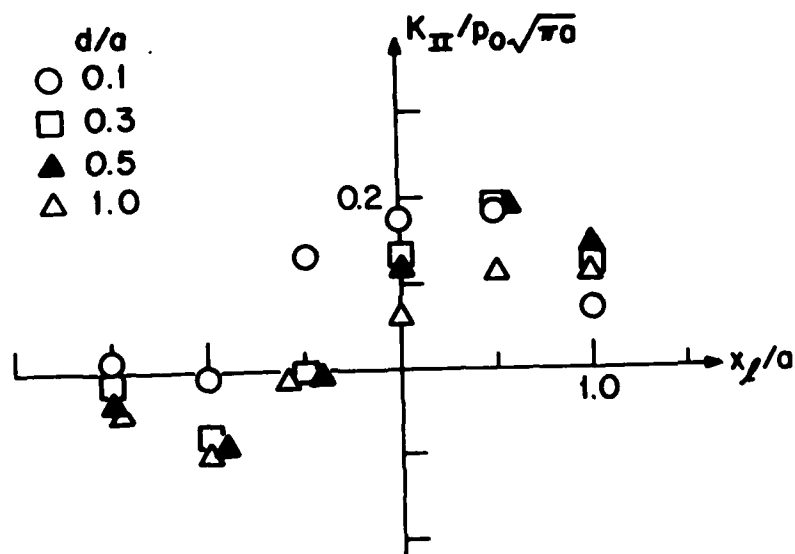
Fig. 3.7 Normalized Mode II stress intensity factor vs. distance from asperity centerline: c = 1/4a; μ = 0.25; left tip.
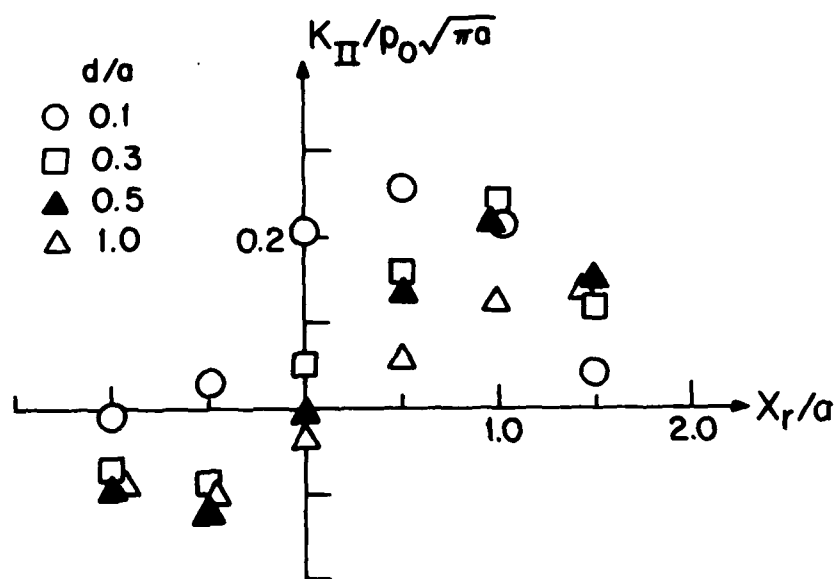
Fig. 3.8 Normalized Mode II stress intensity factor vs. distance
from asperity centerline: c = 1/4a; μ = 0.25; right tip.
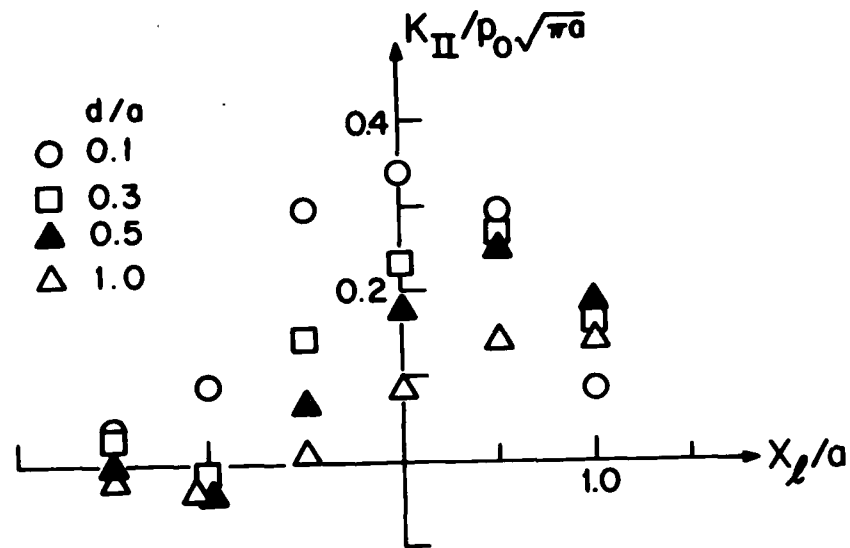
Fig. 3.9 Normalized Mode II stress intensity factor vs. distance from asperity centerline: c = 1/4a; μ = 0.5; left tip.
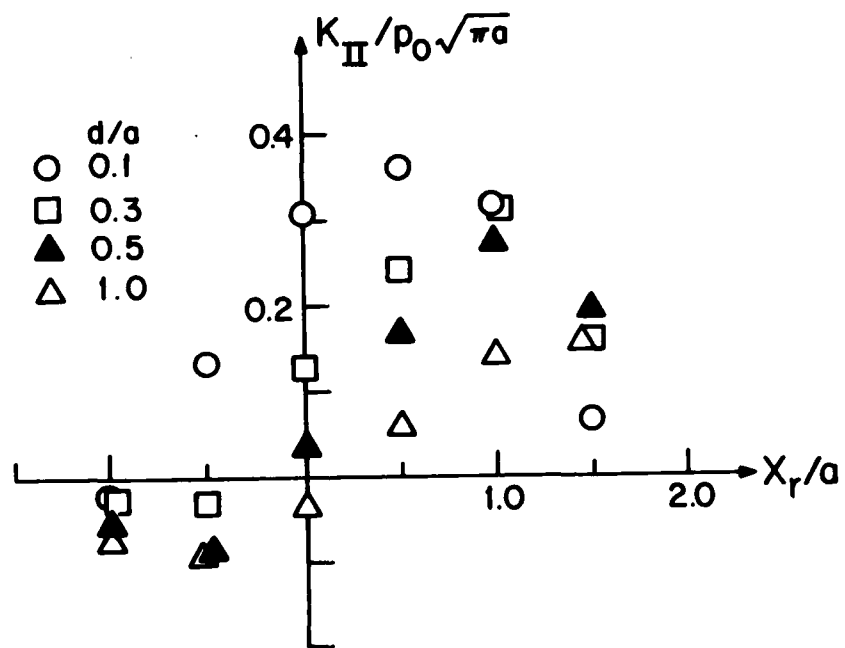
Fig. 3.10 Normalized Mode II stress intensity factor vs. distance from asperity centerline: $c = 1/4a$; $\mu = 0.5$; right tip.
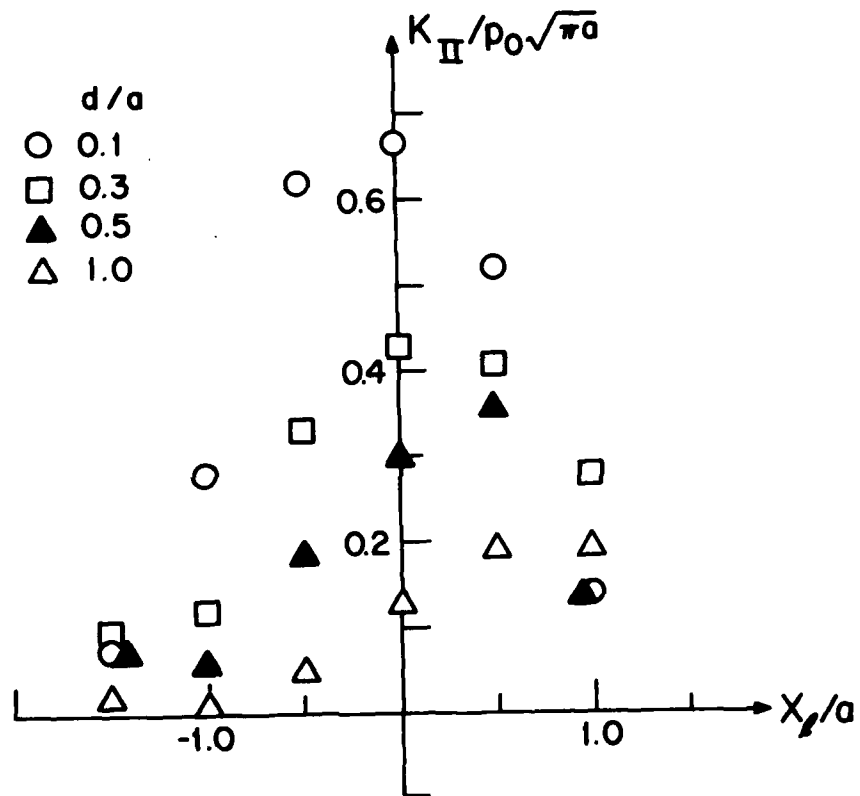
Fig. 3.11 Normalized Mode II stress intensity factor vs. distance from asperity centerline: $c = 1/4a$; $\mu = 1.0$; left tip.
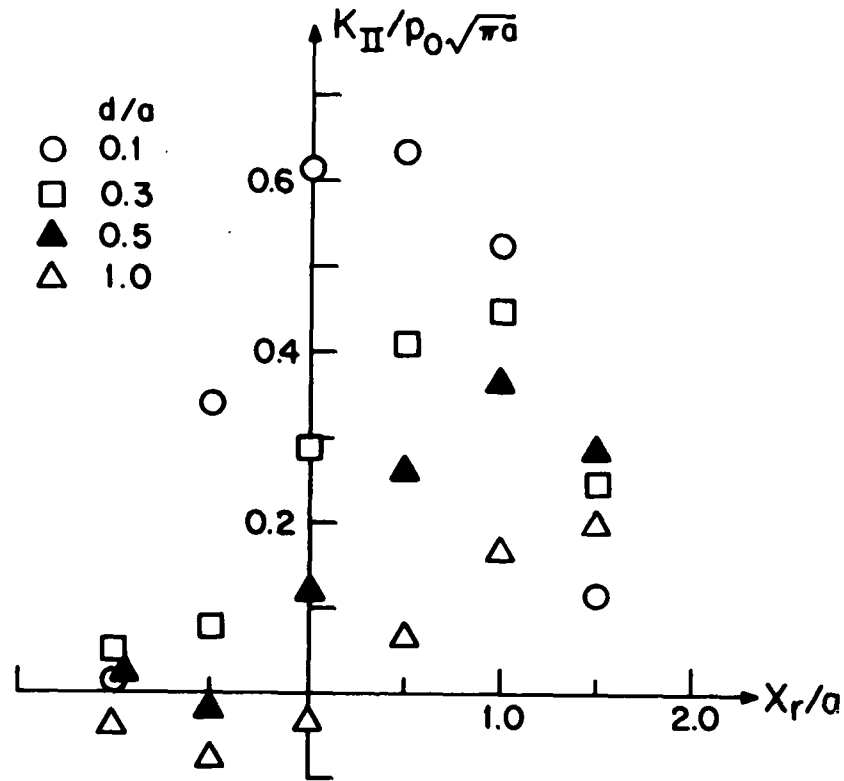
Fig. 3.12 Normalized Mode II stress intensity factor vs. distance
from asperity centerline: $c = 1/4a$; $\mu = 1.0$; right tip.
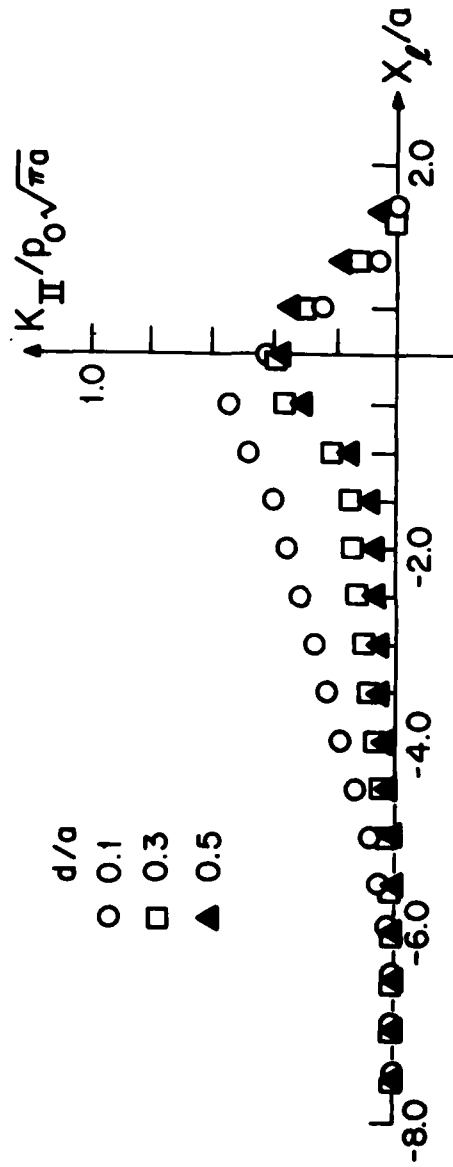
Fig. 3.13 Normalized Mode II stress intensity factor vs. distance from asperity centerline: c = 3a; μ = 0.25; left tip.
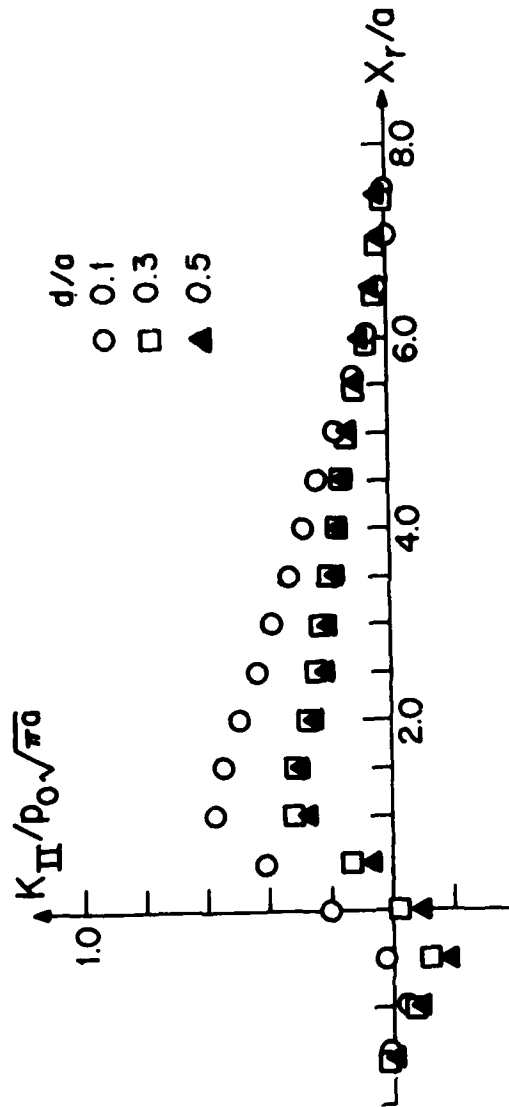
Fig. 3.14 Normalized Mode II stress intensity factor vs. distance
from asperity centerline: c = 3a; μ = 0.25; right tip.
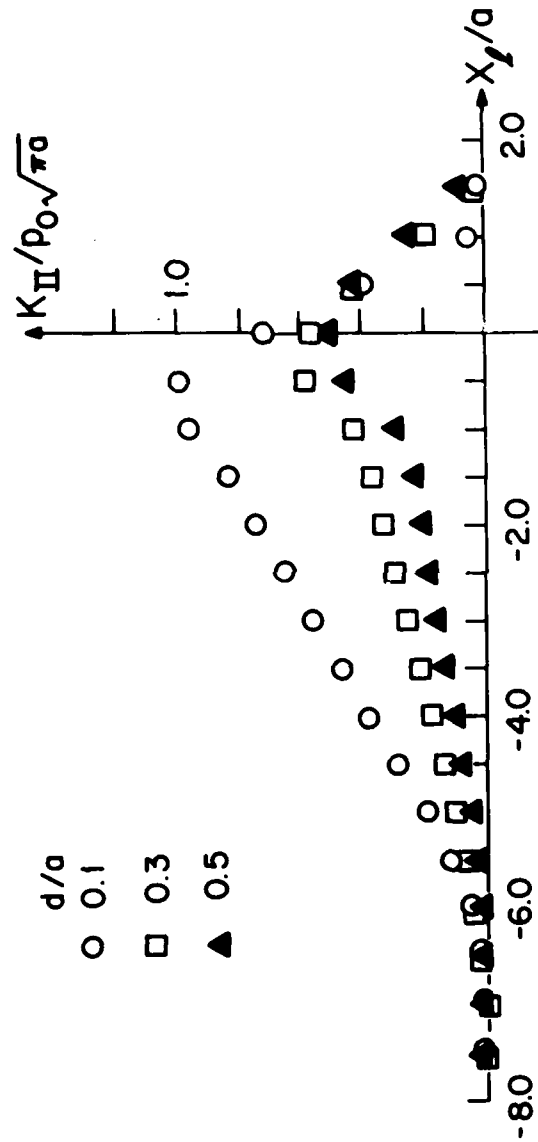
Fig. 3.15 Normalized Mode II stress intensity factor vs. distance from asperity centerline: c = 3a; μ = 0.5; left tip.

1.0

1.1

1.25   1.4   1.6

2.8   2.5

3.2   2.2

3.6

4.0   2.0

1.8

MICROCOPY RESOLUTION TEST CHART
NATIONAL BUREAU OF STANDARDS-1963-A

94
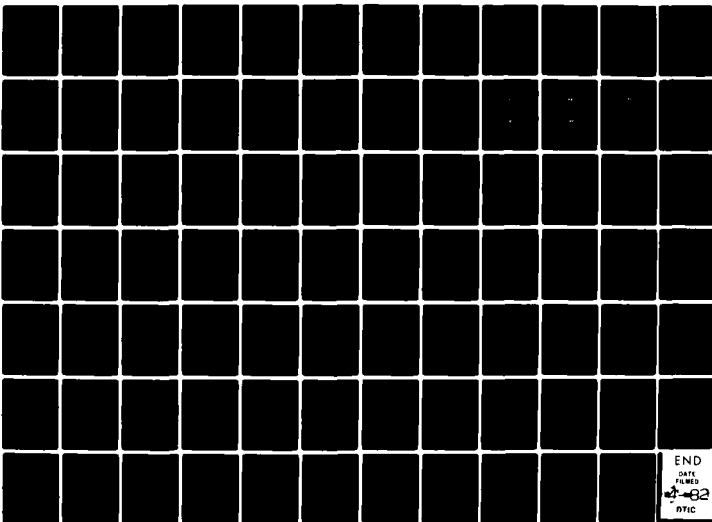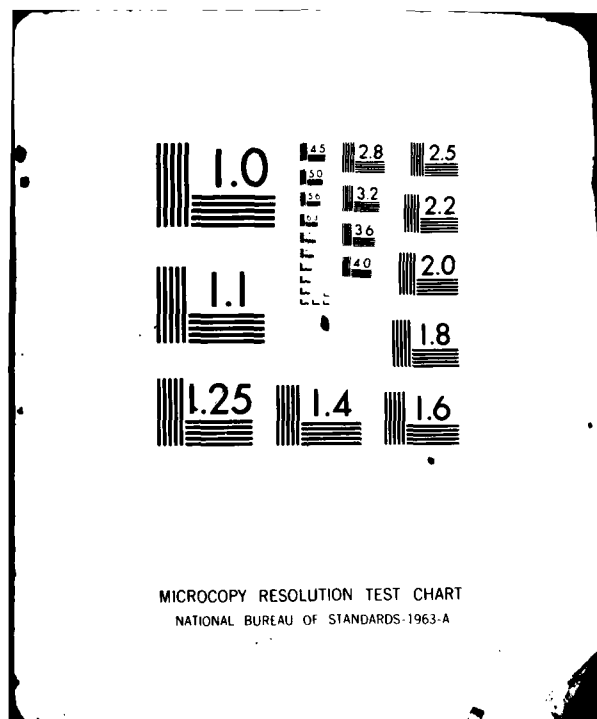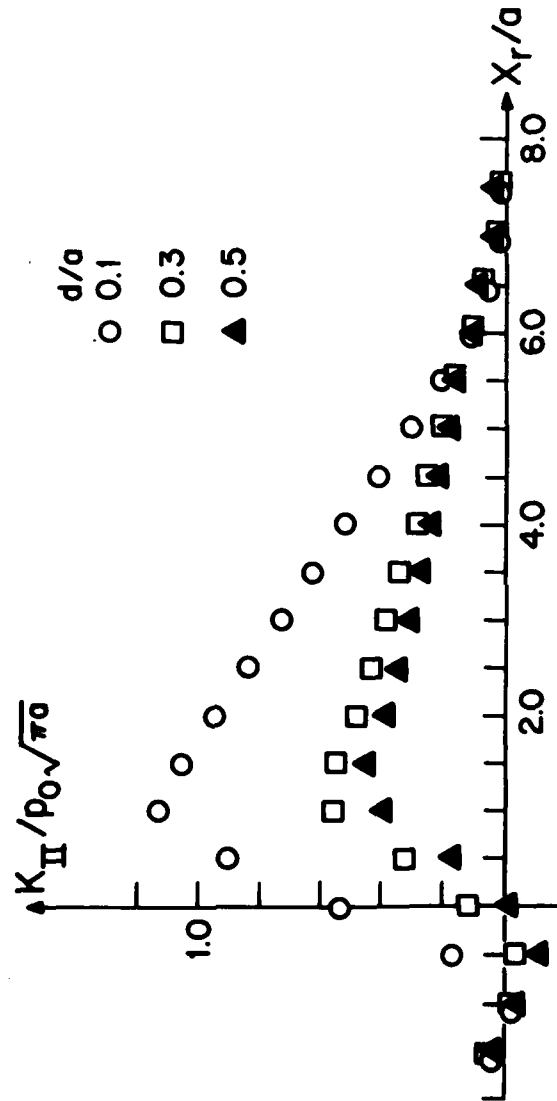
Fig. 3.16 Normalized Mode II stress intensity factor vs. distance
from asperity centerline: c = 3a; μ = 0.5; right tip.
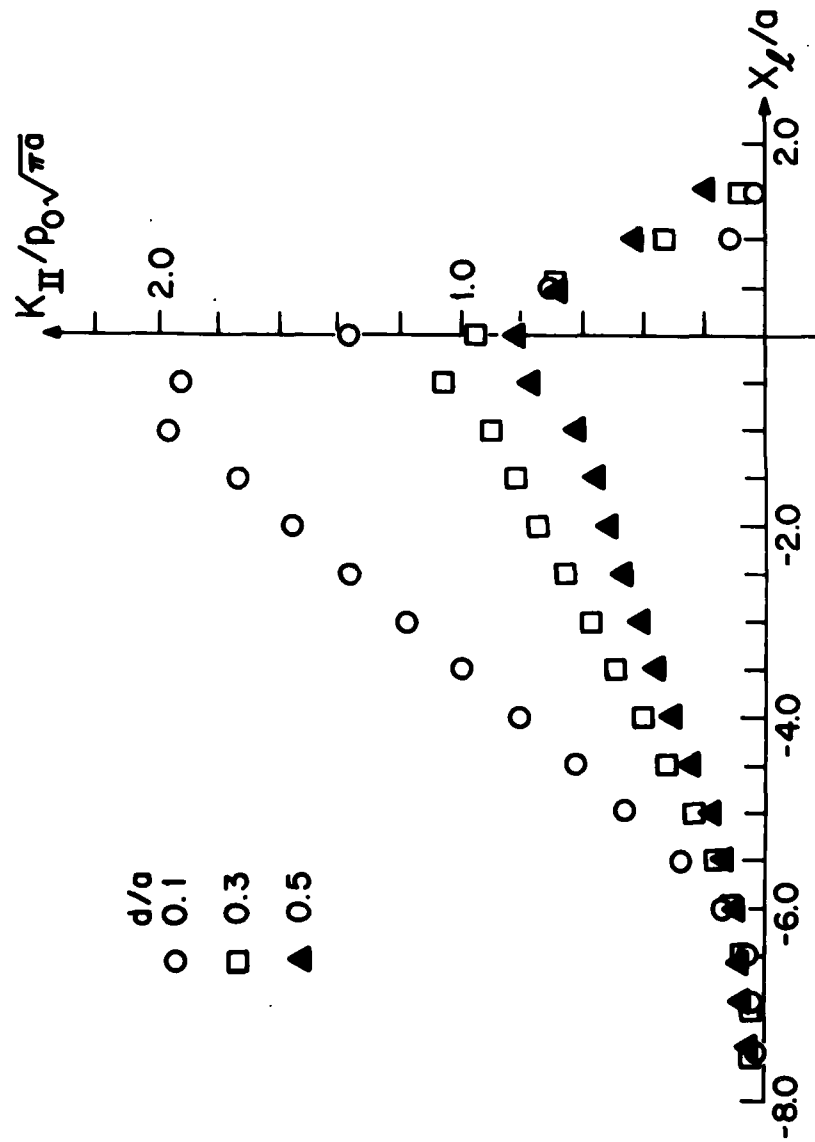
Fig. 3.17 Normalized Mode II stress intensity factor vs. distance from asperity centerline: $c = 3a$; $\mu = 1.0$; left tip.
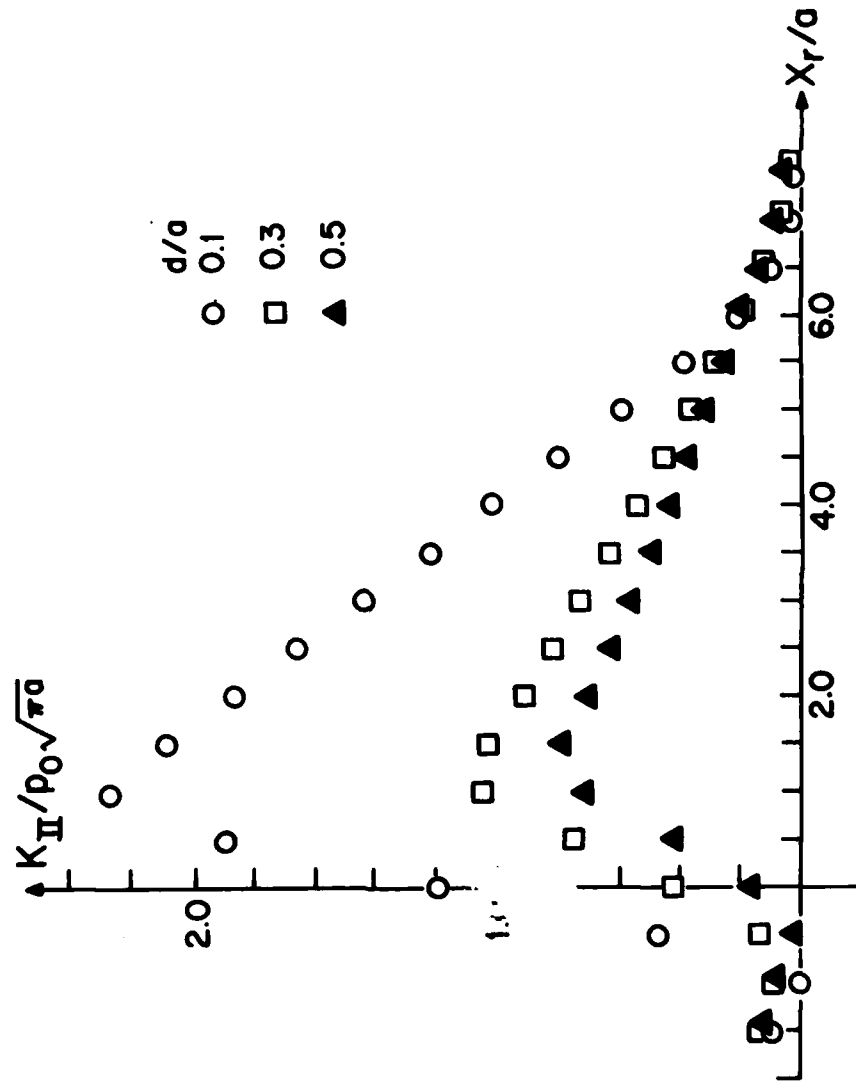
Fig. 3.18 Normalized Mode II stress intensity factor vs. distance from asperity centerline: $c = 3a$; $\mu = 1.0$; right tip.

3.4 Crack Trajectory - Fracture Criteria in Mixed Mode

Until recently, no suitable failure criterion could be found for the mixed mode fracture. Instead, attention has been given only to the problem of predicting the direction of crack extension when a body with cracks is loaded. There are two major criteria: maximum hoop stress [58] and minimum strain energy density [59]. The maximum hoop stress criterion states that crack growth will occur in a direction perpendicular to the maximum principal stress. On the other hand, the minimum strain-energy-density factor criterion postulates (1) that the initial crack growth takes place in the direction along which the strain-energy-density factor possesses a stationary value, and (2) that crack initiation occurs when the factor reaches a critical value. Comparison of the two criteria by several authors has shown that for tensile loading the differences between them are small. For compressive loading, however, not only these two do not agree well but also neither criterion correlates well with physically observed behavior [51].

When these criteria are applied to the subsurface cracks in a compressive zone they predict crack extension direction to be about -70° (110° from x-axis) at the left tip and about 70° at the right tip from the direction parallel to the surface, implying that crack extension occurs toward the surface at both tips. However, experimental results by Jahanmir [41] show that the subsurface cracks grow parallel to the surface most of the time before they become loose. McClintock [52] has suggested, in the investigation of crack behavior in the rail head under rolling condition, that cracks in a compression field are most likely to grow in shear. In fact, Forsyth [60] has observed that fatigue cracks

have two growth regimes. In Stage I, cracks formed on the slip planes
of the persistent slip bands grow when they are most closely aligned
with the maximum shear stress directions.

The crack growth in the shear direction has been observed and
suggested in many cases. In the study of ductile fracture with rotation
Tipnis and Cook [61] have shown that ductile fracture occurs in the
shear zones by either the tail mechanism when an inclusion consists of
a hard core and two soft tails, or the void mechanism when inclusion-
matrix decohesion or brittle fracture of an inclusion occurs, because
most engineering materials contain inhomogeneities which provide nucleating
points for the fracture. While, Smith [62] and Shieh [63] were able to
find the compressive shear cracks which propagate in the slip bands.
Further, Besuner [64] has suggested that if the cyclic principal stresses
are primarily compressive, then there is no reason for a crack to align
itself at right angles to a compressive maximum principal stress.
Therefore, it is necessary to investigate the variation of the maximum
shear stress with angle θ, which is treated below.

In 2-dimensional deformation field the stresses at the crack tip
are expressed as [58]

$$\sigma_r = \frac{1}{2\sqrt{2\pi r}}[K_I \cos\frac{\theta}{2}(3 - \cos\theta) + K_{II} \sin\frac{\theta}{2}(3 \cos\theta - 1)]$$

$$\sigma_\theta = \frac{1}{\sqrt{2\pi r}} \cos\frac{\theta}{2}[K_I \cos^2 \frac{\theta}{2} - \frac{3}{2} K_{II} \sin\theta] \qquad (3.1)$$

$$\sigma_{r\theta} = \frac{1}{2\sqrt{2\pi r}} \cos\frac{\theta}{2}[K_I \sin\theta + K_{II}(3 \cos\theta - 1)]$$

and the maximum shear stress τ_{max} is given by

$$\tau_{max} = \frac{1}{2\sqrt{2\pi r}}[K_I^2 \sin^2\theta + 2K_I K_{II} \sin 2\theta + K_{II}^2(4 - 3\sin^2\theta)]^{1/2} \quad (3.2)$$

τ_{max} will have maximum values when the conditions of $\partial\tau_{max}/\partial\theta = 0$ and $\partial^2\tau_{max}/\partial\theta^2 < 0$ are satisfied. If we denote θ_m for the angle θ which satisfies the conditions and substitute into Eq. 3.1, then the stresses become $[\sigma_r]_{\theta_m}$, $[\sigma_\theta]_{\theta_m}$, and $[\tau_{r\theta}]_{\theta_m}$ respectively. Thus, using the Mohr's circle transformation, the maximum of τ_{max} and the angle between θ_m-direction and this maximum shear direction can be determined. When the distance r goes to zero, this direction ultimately becomes the direction of crack propagation.

If the above criterion is applied to the results obtained in the previous section for the subsurface cracks, it predicts the angle to be between -5 and 5 degrees. These values are very small and therefore can practically be assumed zero, implying that cracks propagate in a plane coincident with the original cracks parallel to the surface.

3.5 Crack Tip Plasticity Consideration

Whether the linear elastic fracture mechanic (LEFM) approach is appropriate depends on the plastic zone size at the crack tip. If this size is too big or comparable with such dimension as the distance from the crack tip to a free surface, LEFM is no longer valid and plasticity plays a significant role. In this case the local stress and strain history may become important in determining the fracture criterion [65].

The estimate of the plastic zone size for Mode II loading is given by

$$r_p = \frac{1}{2\pi} \left(\frac{\Delta K_{II}}{k}\right)^2 \tag{3.3}$$

where ΔK_{II} is the stress intensity factor range in Mode II and k is the shear yield strength of the material. Tables 3.1 and 3.2 show the changes in stress intensity factor and estimated plastic zone sizes as a function of the depth of crack location for a small crack during one cycle of loading. Values for all parameters are the same as given before: $k = 245$ MPa $= 25$ kg/mm^2, $a = 10$ μm. From these two tables it can be seen that the plastic zone sizes estimated are comparable with the depth of crack and the stress intensity factor ranges calculated are close to or less than the threshold intensity ΔK_{th} [66]. Of course, there is no data in Mode II available. However, an approximate analysis treated in Appendix E indicates that the threshold intensity factor in Mode II is very close to that in Mode I.

There are two difficulties in accepting the linear elastic fracture mechanics approach to the subsurface crack problem. The cracks quite near the surface can have large values of ΔK_{II}, but they cannot propagate in a brittle manner due to the development of large plastic zones. On the other hand, cracks far below from the surface cannot grow since the stress intensity factors for these are much smaller than the threshold although the plastic zones are small and the plasticity restriction does not apply. Therefore, plasticity should come into the analysis of subsurface crack behavior under the moving asperity.

Table 3.1. Stress Intensity Factor Range, ΔK_{II} ($MNm^{-3/2}$), at Left and Right Tips for a Small Crack (c = 1/4a)

d/a		μ: 0.25	0.5	1.0
0.3	Left	1.05	1.07	1.44
	Right	1.28	1.34	1.54
0.5	Left	1.08	1.11	1.15
	Right	1.35	1.40	1.49
1.0	Left	0.67	0.68	0.70
	Right	0.89	0.94	1.06

a = half length of asperity contact

d = depth of crack location

μ = coefficient of friction

Table 3.2. Ratio of Plastic Zone Size to Depth of Crack at
Left and Right Tips for a Small Crack (c = 1/4a)

d/a		μ: 0.25	0.5	1.0
0.3	Left	0.96	1.00	1.48
	Right	1.44	1.56	2.08
0.5	Left	0.76	0.80	0.88
	Right	1.20	1.28	1.48
1.0	Left	0.12	0.12	0.12
	Right	0.20	0.24	0.32

In summary, linear elastic fracture mechanics is found to be useful in assessing the crack tip stress concentration and in determining the crack trajectory by mixed mode fracture criteria. However, the size restriction by plasticity consideration and the small stress intensity factors calculated (which is less than the threshold) suggest that the plastic fracture mechanics approach is required.

4. THE MECHANISM OF SUBSURFACE CRACK PROPAGATION -

PLASTICITY APPROACH

4.1 Introduction

It was shown in the previous chapter that linear elastic fracture mechanics is inadequate in explaining the mechanism of subsurface crack propagation. In this chapter the mechanism of crack propagation is investigated through the elastic-plastic finite element analysis. The first part of it deals with the nature of plastic deformation under moving load condition when there is no crack. Then, the elastic-plastic response of a crack in the subsurface is studied and the mechanism of crack propagation is discussed.

4.2 The Elastic-Plastic Finite Element Model

In this study ADINA (Automatic Dynamic Incremental Nonlinear Analysis, a finite element computer program for the static and dynamic displacement and stress analysis of solids, fluid-structure systems and structures) was used as in the elastic analysis case in Chapter 3 [67]. The material model used in the study was as follows: infinitesimal, material nonlinear only [68]. The isothermal elastic-plastic incremental constitutive relations are shown in Appendix F.

The model used to calculate the elastic-plastic response under the moving load condition was the same as that for the elastic case. No dynamic effect was considered in the analysis. The material was assumed to be slightly work-hardening ($E_T = 10^{-4}$ E). The material properties used were as follows: isotropic, slightly work-hardening,

$E = 1.96 \times 10^5$ MPa $= 2 \times 10^4$ kg/mm^2, $E_T = 19.6$ MPa $= 2$ kg/mm^2,

$\nu = 0.28$, $\sigma_y = 3\sqrt{k} = 424$ MPa $= 43.3$ kg/mm^2.

The finite element mesh used for the study of plastic deformation without a crack was the same as shown in Fig. 3.5. For the investigation of crack propagation only a short crack (c = 1/4a) shown in Fig. 3.4 was used. Due to the prohibitively expensive computer cost only a limited parameter study was conducted for the case of a = 10 μm, $p_0 = 4k$, and μ = 0.25.

The problem was solved incrementally by moving the load step by step. For an accurate solution, the load increments per step should be sufficiently small. However, such a load step requires a large number of calculations that make the analysis very expensive. Therefore, larger load steps were used with iteration to obtain efficient and accurate solutions.

The use of iteration can introduce some difficulties. The convergence process may be slow, requiring a large number of iterations that can be expensive. Also, some iterative methods do not converge for certain types of problems or large load increments.

In ADINA program the following procedures are implemented for the iterative solution of the incremental equilibrium equations: (a) modified Newton iteration with/without Aitken acceleration and a divergence procedure and (b) the Broyden-Fletcher-Goldfarb-Shanno (BFGS) method. These are described in detail in Reference 69 by Bathe and Cimento. The modified Newton iteration procedure is based on the stiffness matrix at time t, $^t\underline{K}$, while the BFGS method updates the matrix based on the iteration history. When divergence is detected for the modified Newton

method, the divergence scheme is incorporated, which uses smaller load increments. According to Bathe and Cimento iteration divergence can occur whenever the system stiffens during the solution increment. For the present study the BFGS method was used because it has better convergence properties.

4.3 Numerical Results

4.3.1 Plastic Deformation and Residual Stresses

Fig. 4.1 shows the plastically deformed region under a moving asperity during the first and fourth cycle, respectively. Under the moving load the material just in front of the load gets plastically deformed and some part of the plastic region behind it becomes unloaded. Due to this internal unloading the shape of the plastically deformed region under moving load is quite different from that under static load (see Fig. 4.2). Furthermore, the repeated loading-unloading makes the plastic region smaller as shown in Fig. 4.1(b). According to the numerical investigation of a rolling contact by Anand [70], a steady state after a few revolutions of a disk would eventually reach a purely elastic state for a strain-hardening material whereas elastic-plastic steady state condition could be expected for elastic-perfectly plastic materials at higher loads. Therefore, the case shown in the figure may eventually reach a purely elastic steady state since the material is slightly work-hardening.

The residual stress σ_x^r is given in Fig. 4.3 as a function of depth from the surface. It can be seen that the variation in σ_x^r is almost negligible after 3 or 4 cycles. Also, the dominant residual stress is
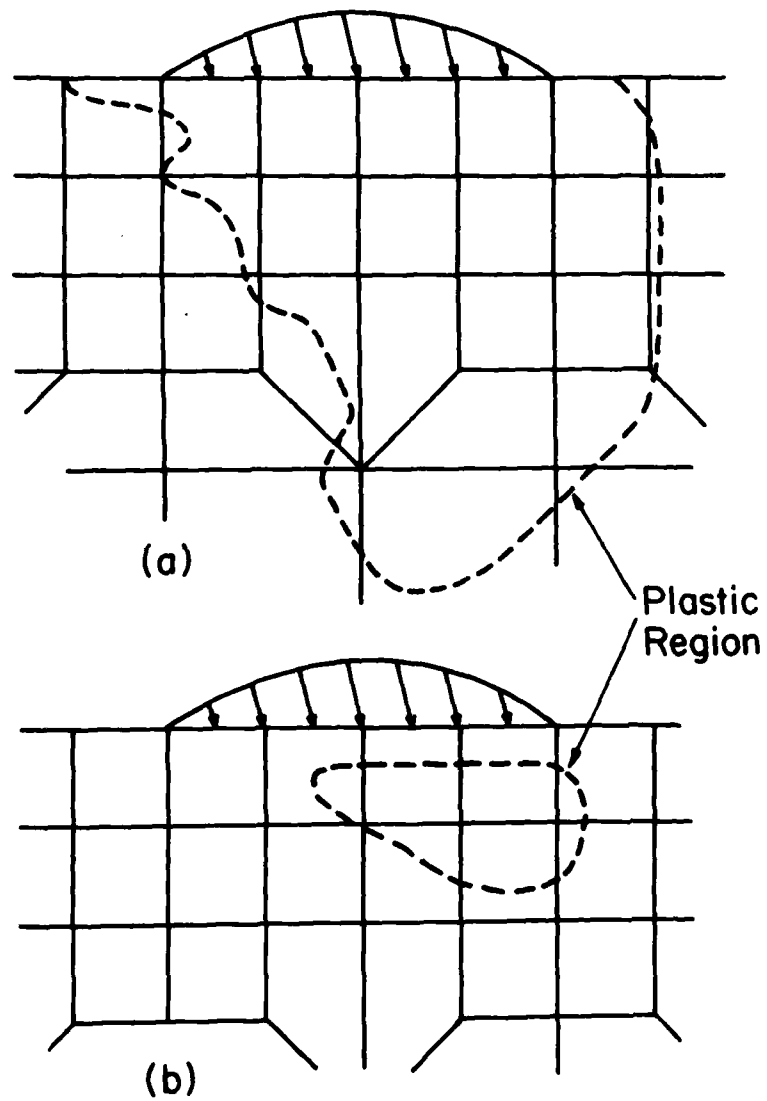
Fig. 4.1 Plastically deformed region under a moving asperity:
(a) during the first cycle; (b) during the fourth
cycle.
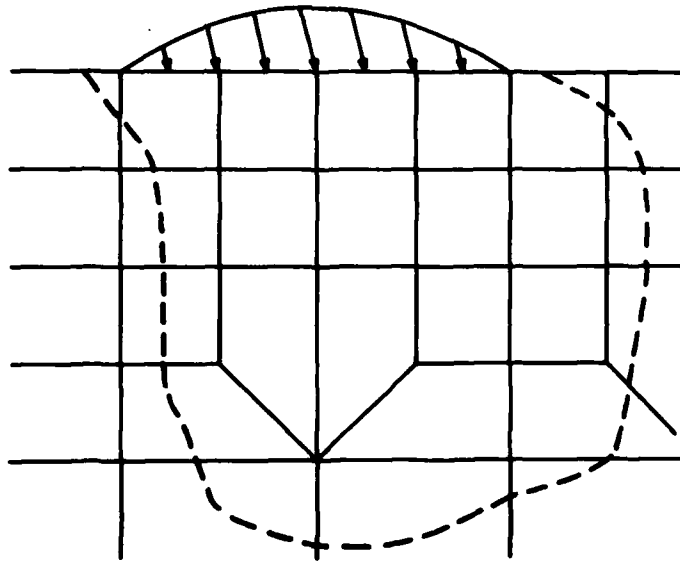
Fig. 4.2 Plastic zone under a stationary asperity.
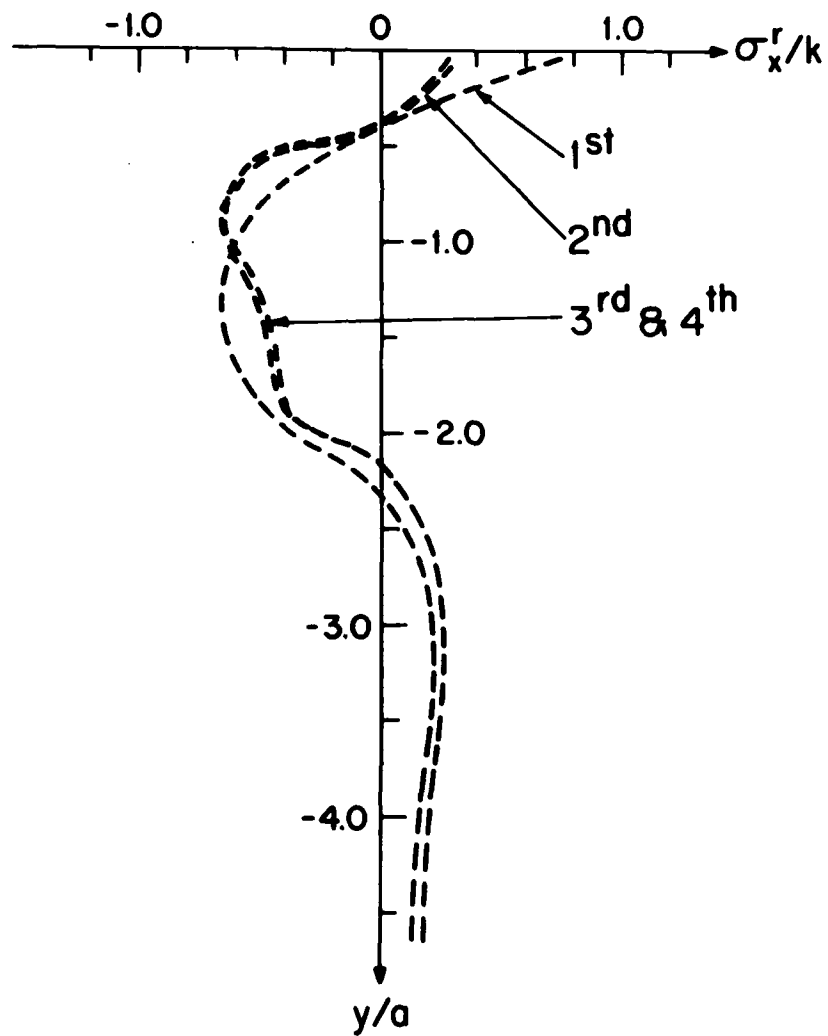
Fig. 4.3 Variation of residual stress σ_x^r as a function of depth under a moving asperity.

compressive in a direction parallel to the surface. The other components of residual stresses, $\sigma_y{}^r$ and $\tau_{xy}{}^r$, are very small, which should be zero to satisfy equilibrium [100]. Since these two are the only components that can affect crack opening and sliding, it can be concluded that residual stresses do not affect crack propagation.

Due to the compressive residual stress the stress σ_x is always compressive right behind the asperity contact except very near the surface. If there is a crack running perpendicular to the surface, the crack may grow downward only a small amount of less than one quarter of the asperity contact length. Then, it will cease to grow further downward because of the compressive stress σ_x that prevents the crack opening. Therefore, it may be considered that the magnitude of the residual stress $\sigma_x{}^r$ is large enough to make the steady state stress σ_x compressive, which prevents cracks from running downward.

4.3.2 Crack Tip Field Under Moving Load

Proper crack tip modeling is quite important in simulation of crack tip deformation and propagation. As discussed in the previous chapter a triangular element has a 1/r singularity when three nodes are at a crack tip, being allowed to separate during deformation, and the side-nodes are at the midpoints (see Fig. 3.1b). This type of singularity representation is suitable for the HRR field [71-73] when the material model is elastic-perfectly plastic.

In the field of finite element analysis of structures Nagtegaal et al. [74] have found that some frequently used elements, including the three-noded triangle and the four-noded isoparametric element, are not

suited for analysis in the fully plastic range. For example, load-displacement curves obtained by finite element calculations generally exceed known limit loads, and in some cases the solutions have no limit load at all. Also, deLorenzi and Shih [75] have shown that the eight-noded elements in general have the same deficiency. The exact limit load for a beam in bending was, however, obtained when eight-noded isoparametric elements with straight edges were used. Further study by the same authors suggests that the element coupled with the appropriate near-tip configuration possessing a 1/r singularity is ideally suited for elastic-plastic crack analyses [76].

When the plastic elements mentioned above are used in the case of tensile loading, they allow the modeling of crack tip blunting as the nodal points separate during deformation. However, when a crack tip is in the combined compression and shear loading, all nodes at the tip must be constrained properly. Without any constraint too many crack tip nodes may result in a geometrically incompatible state. Results of preliminary calculations for different crack tip modeling have suggested that only one element with 1/r singularity in the direction of propagation and several singular elements of other type around the element should be a good mesh design. This is shown in Fig. 4.4.

If the crack tip is constrained in such a way that all nodes move together during deformation (i.e., if all crack tip elements are the type of $1/\sqrt{r}$ singularity), the equivalent strain at the nearest integration points can reach as high as about 200 for a crack located at d = 0.5a. (3 x 3 integration order was used.) In Figs. 4.5 and 4.6 the shear strain γ_{xy} is plotted as a function of distance from the crack tip under
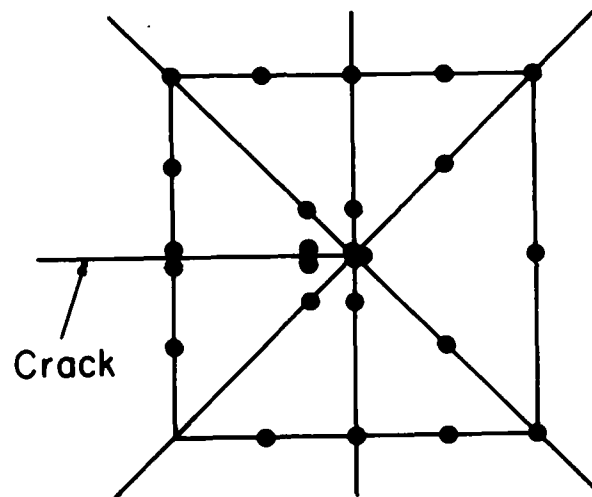
Fig. 4.4 Finite element mesh around a crack tip.
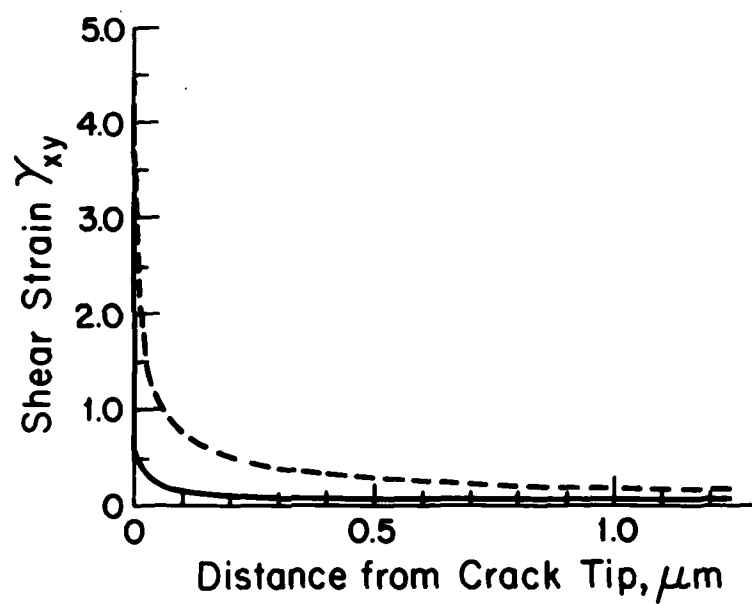
Fig. 4.5   Shear strain vs. distance from the left crack
tip when one-node crack tips are used.
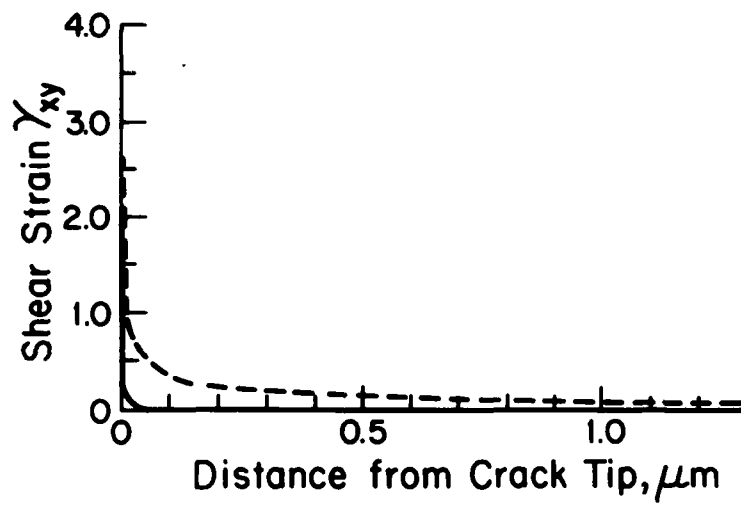
Fig. 4.6 Shear strain vs. distance from the right crack
tip when one-node crack tips are used.

moving load for both leading and trailing tips. The shear strains are initially low when sliding begins and reach very high values, remaining nearly at these levels. It can be seen that the shear strain at the left tip is about twice as high as the strain at the right tip. If the strains are so large, then the material at tips cannot support such strains and fracture will occur immediately. Although this model shows that the strains at the tip can reach infinity, it cannot adequately describe the details of crack tip deformation.

The plastic singular element can allow the modeling of crack tip shear deformation when it is used for shear loading. Fig. 4.7 shows the development of plastic zone along with the moving load step by step when this element is used. At the beginning the shape of the plastically deformed zone is more or less the same as shown in Fig. 4.2 for the case of no crack inside except right around crack tips. Due to the presence of a crack the stress field changes very much when the load moves over the crack. It can also be noticed that there are some spots inside the plastic region where unloading has taken place. With the repeated loading-unloading it is expected that the overall plastic zone should become smaller as in the case of no crack shown in Fig. 4.1.

Examination of the displacements of the nodal points on the crack surfaces shows that the upper surface initially slides forward and then it slides backward. This is consistent with the result by McClintock [52] who investigated the behavior of a subsurface crack in rolling contact problem. In Table 4.1 the relative sliding displacements of crack tip nodel points are shown for two different depths of crack location. It shows that the relative displacement increases with sliding, then
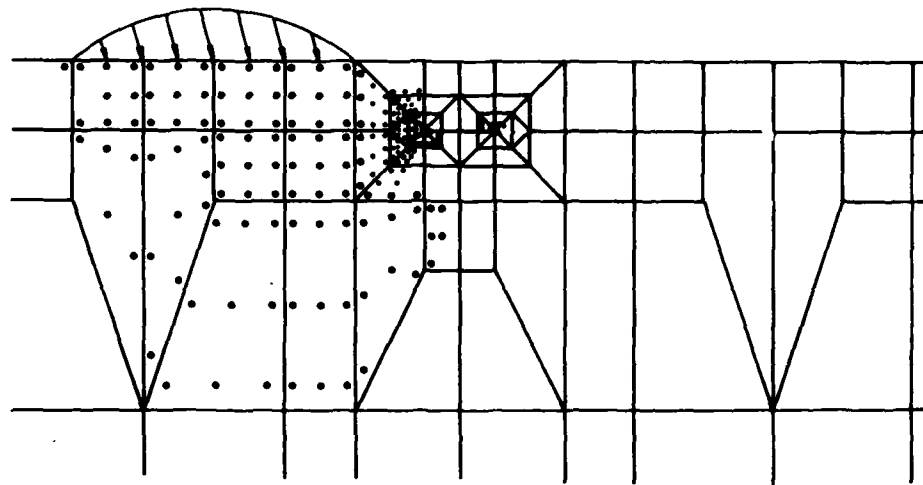
(a)
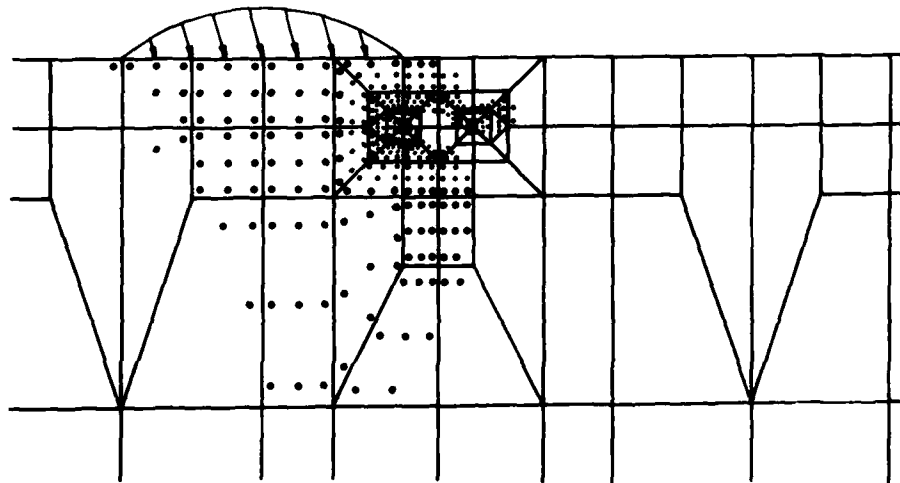
(b)

Fig. 4.7 Variation of plastically deformed zone around a crack
under a moving asperity: a = 10 μm, d = 0.5a, μ = 0.25,
P_o = 4k = 980 MPa. Dots indicate the integration points.
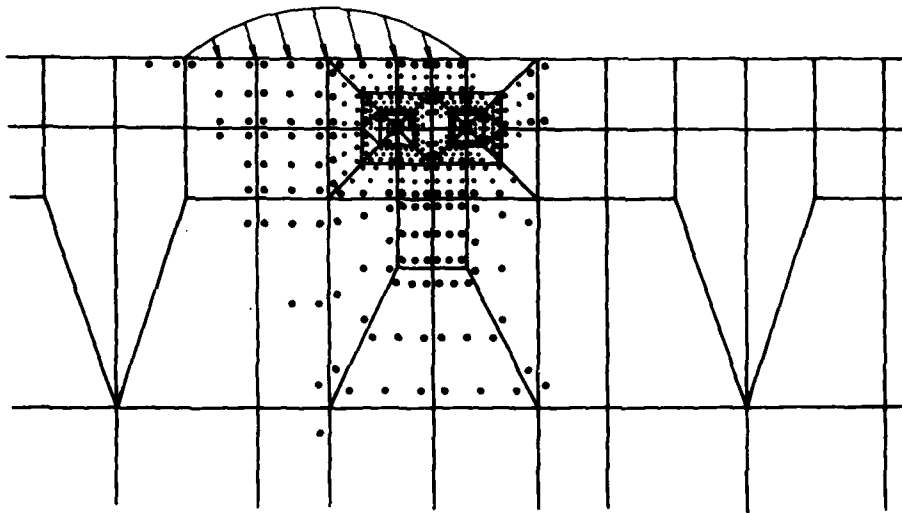
(c)
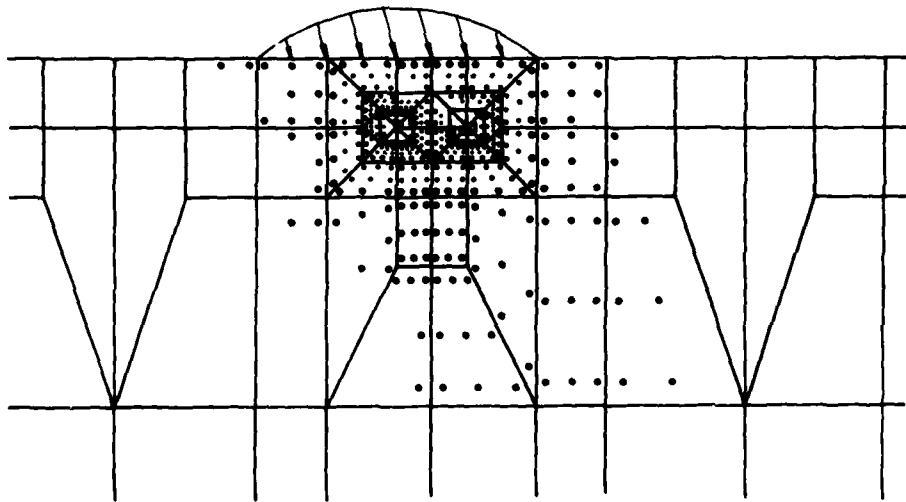
(d)

Fig. 4.7 (Cont'd)
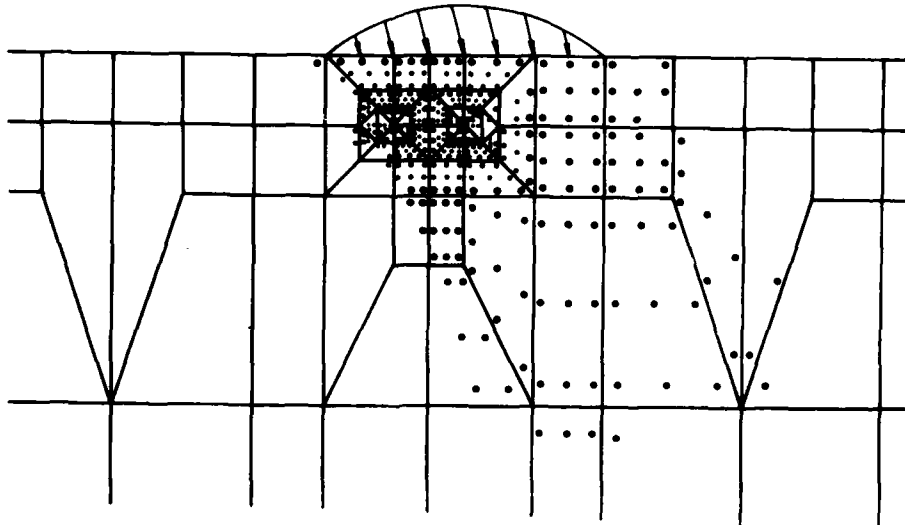
(e)
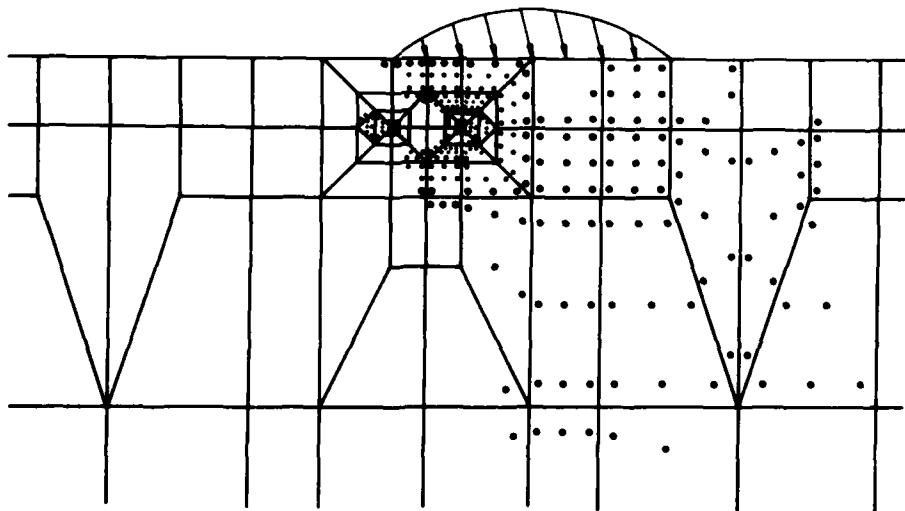
(f)

Fig. 4.7   (Cont'd)
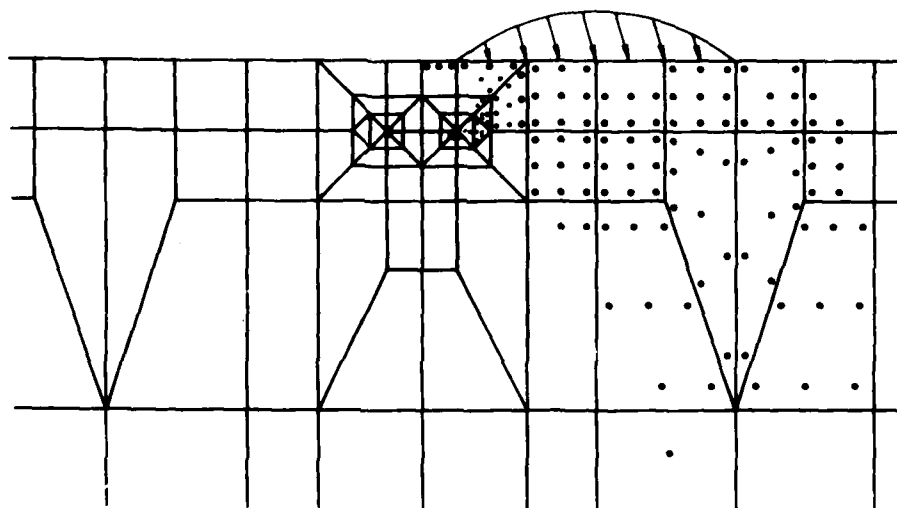
(g)
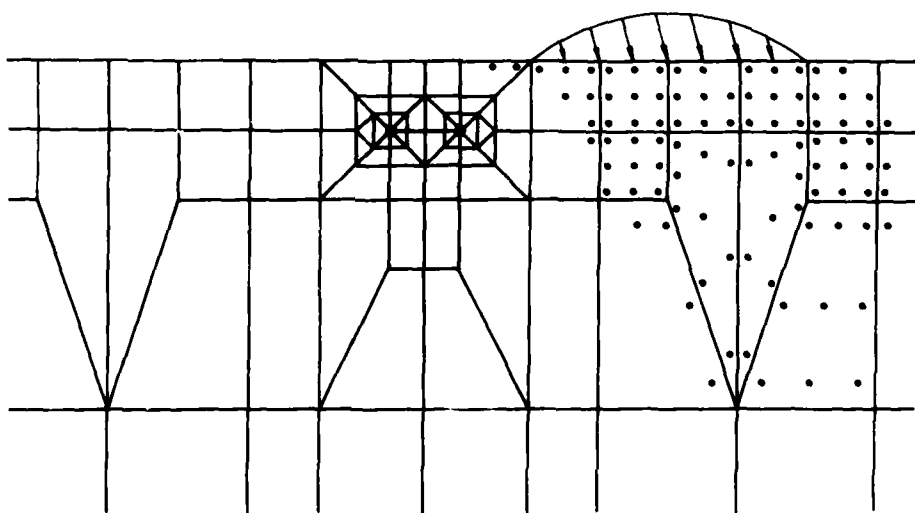
(h)

Fig. 4.7   (Cont'd)

Table 4.1. Relative Crack-Tip Sliding Displacement (μm)

(a) d = 0.5a

	a	b	c	d	e	f	g	h*
Right Tip	0.0009	0.0023	0.0033	0.0027	0.0015	-0.0009	-0.0008	-0.0001
Left Tip	0.0013	0.0030	0.0035	0.0028	0.0004	-0.0012	-0.0005	-0.00003

(b) d = 0.25a

	a	b	c	d
Right Tip	0.0003	0.0012	0.0077	0.0093
Left Tip	0.0002	0.0031	0.0141	0.0138

*Each step corresponds to the relative position shown in Fig. 4.7.

decreases, and finally changes the sign. Followings can also be observed from the table: (1) the crack closer to the surface has large values, and (2) the left tip usually has large values of relative sliding displacements.

In Figs. 4.8 and 4.9 the crack tip shear strains are plotted along the distance from the crack tip for different stage of the loading position as the asperity contact moves from left to right. The distribution of shear strain increases until it reaches a maximum value and then decreases. After it attains a minimum, it increases again. At very near the tip the shear strain changes from positive to negative, and then to positive again. For a crack located at d = 0.25a, the shear strain can reach more than 120% at a point of 0.00625 μm away from the tip.

4.4 Discussion on Crack Propagation

The elastic solutions for cracks have a stress singularity of the type $1/\sqrt{r}$. The singular terms of the solutions are valid within a region of radius r_e near a crack tip. Because of the singularity in the stresses, the yield condition is quickly reached at the crack tip. If the plastic deformation is limited to a region of radius r_p and $r_p << r_e$, the distortion of stresses on r_e caused by the plastic deformation within r_p is negligible. In this case the stress distribution in the elastic region is uniquely specified by the stress intensity factors and the crack propagation is completely characterized by the critical stress intensity factor. However, the results of the plastic zone estimation in Chapter 3 and the elastic-plastic stress calculation in the previous section clearly
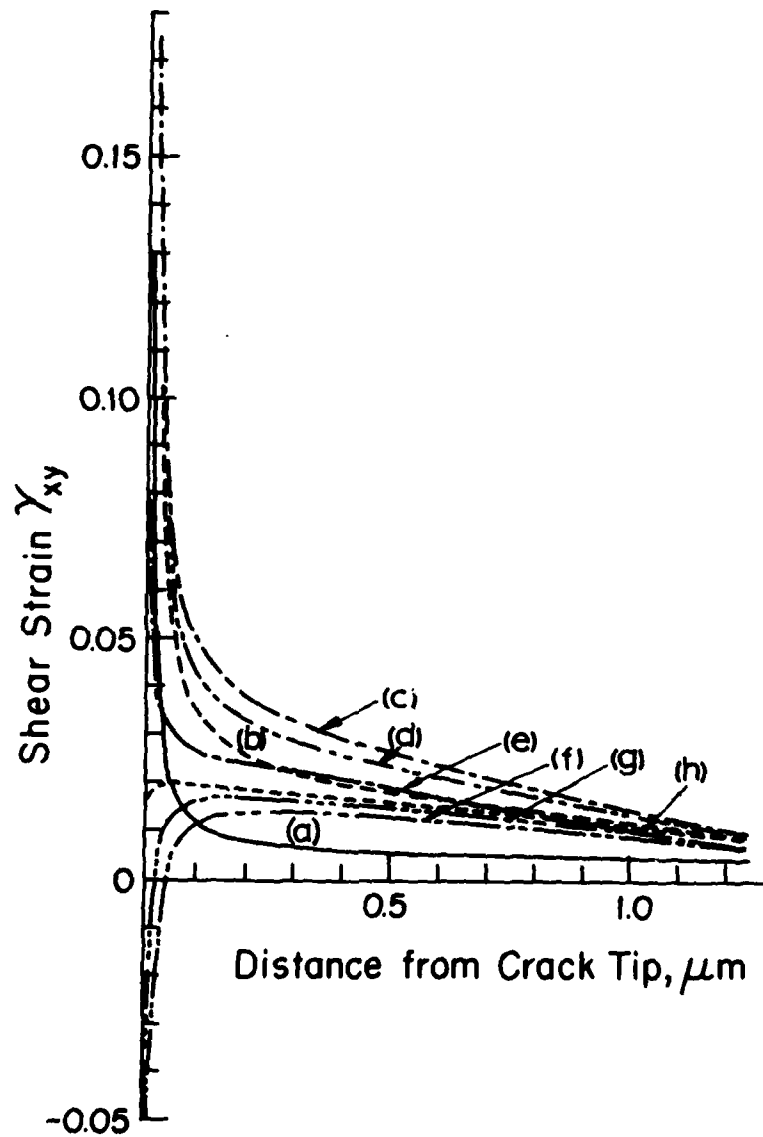
Fig. 4.8 Shear strain vs. distance from the left crack tip
when plastic elements are used. (a), (b), (c),
(d), (e), (f), (g), and (h) refer to the position
of the left tip relative to the asperity contact
shown in Fig. 4.7.
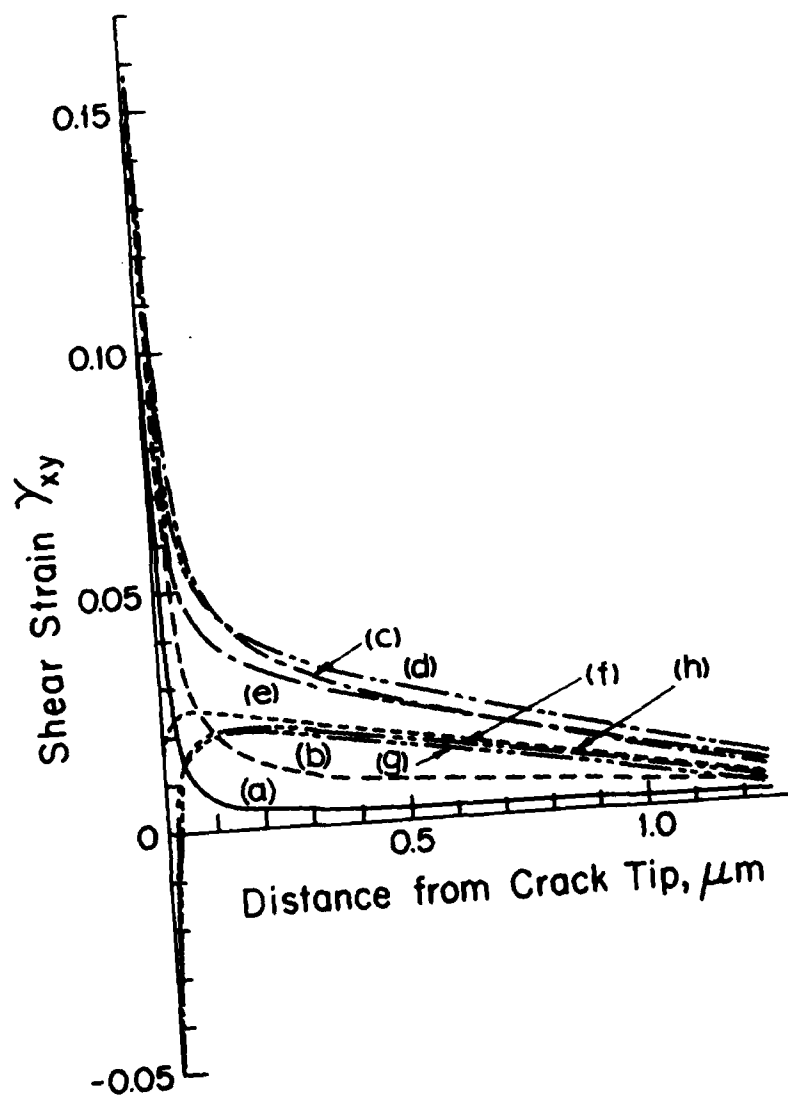
Fig. 4.9   Shear strain vs. distance from the right crack tip
when plastic elements are used.   (a), (b), (c),
(d), (e), (f), (g), and (h) refer to the position
of the right tip relative to the asperity contact
shown in Fig. 4.7.

indicate that LEFM is no longer valid for the present sliding contact problem and plastic fracture mechanics must be used.

4.4.1 Fracture Parameters beyond Linear Elastcity: A Review

In recent years considerable effort has been devoted to extend fracture mechanics into the elastic-plastic regime. These started by examining the stress distribution under fully plastic conditions and small-scale yielding. Among several fracture parameters the J integral and the crack opening displacement (COD) have attracted the attention of many researchers since these are viable candidates from the computation and measurement point of view [77].

For nonlinear elastic material, it is possible to express the potential energy release rate as the line integral, J, [78, 79], evaluated around a contour, Γ, which circumscribes the crack tip in the counter-clock wise sense, starting from a point on the bottom edge of a crack:

$$J = \int_\Gamma (W \, dy - T_i \frac{\partial U_i}{\partial x} \, ds) \qquad (4.1)$$

where

W = the strain energy density = $\int \sigma_{ij} d\varepsilon_{ij}$,

T_i = the traction vector defined according to the outward normal n along Γ, $T_i = \sigma_{ij} n_j$,

U_i = displacement in the direction of T_i,

ds   =   incremental arc length along Γ, and

x,y =   rectangular coordinates.

The properties of J, for nonlinear elastic material, are (1) that it is path independent, (2) that it characterizes the crack-tip stress and displacement fields, and (3) that it is a measure of the elastic energy release rate, G. For linear elastic material, J is identical to G.

Considerable work on developing the J integral as an analytical tool for plastic fracture mechanics has been performed by Begley and Landes [80, 81] using a compliance technique. Following this many investigators have been involved in fracture characterization by J. For example, almost all the papers in the book, Elastic Plastic Fracture, ASTM STP 668, are devoted to J integral approach. Among them some authors have shown that J has a linear relation with COD [82-84].

The crack-opening displacement (COD), first proposed by Wells [85] in 1961, is another powerful tool in elastic-plastic fracture mechanics. The suggestion of Wells is essentially equivalent to assuming that an intensity of plastic strain, critical for fracture, exists adjacent to the crack border [65], leading to a near tip strain fracture criterion [86]. The COD concept has been supported by several authors experimentally and analytically [87-90]. Analytical models as Pelloux's alternating shear model [87] and Kuo and Liu's unzipping model [90] indicate that crack growth is approximately one half of the crack tip opening displacement if rewelding at a crack tip does not occur. Depending on the included angle of the deformed tip crack growth can reach COD.

4.4.2 The Crack Propagation Model in Wear

As reviewed briefly the J integral and the crack-opening displacement are the most frequently used parameters in characterization of crack tip behavior in plastic fracture mechanics. However, some difficulties are associated with these parameters. First, the path independence of J integral, which is derived using deformation theory of plasticity, has not been proved analytically for incremental plasticity. With regard to the characterization of the crack tip field, McClintock has shown that the different degrees of constraint associated with various in-plane configurations would prevent the satisfactory development of a one-parametertheory of plastic fracture mechanics for full plasticity [101]. Elastic-plastic finite element calculations have shown that J is strongly path-dependent for contours very close to the crack tip, which is the region where heavy plastic deformation has taken place [91, 92]. Therefore, the J integral is not appropriate for the present study.

On the other hand, the crack-opening displacement is conceptually simple and straightforward regardless of its appropriateness for a one parameter characterization of crack tip fields, which is still under investigation by many researchers [77, 93]. The analytical treatment, however, is very difficult because of the complexity for elastic-plastic materials and therefore, finite element analyses have been used extensively in studying crack tip profiles. In finite element analysis it is essential to use sophisticated crack tip elements to obtain satisfactory modeling of the deformation. In addition to the computational difficulty, the interpretation of the crack-opening displacement in relation to crack propagation is still to be advanced.

So far almost all the crack tip deformation studies are limited to

Mode I and Mode III. In sliding wear the subsurface cracks are subjected to Mode II loading. The cracks are likely to grow in the direction parallel to the surface. This has already been proved in Chapter 3 even though it was based on elastic solutions. Also the experimental findings of surface texture development due to sliding [94, 95] strongly suggest that the cracks propagate along the slip planes nearly parallel to the surface. Of course, there is a possibility that crack growth should follow the maximum principal stress or the minimum strain-energy-density factor criterion when a crack is in tensile region. However, the existence of a tensile component alone is not sufficient to cause crack growth in the direction that those criteria predict, unless the strength of stress concentration is large enough. Later on this possibility will be discussed further.

The crack-opening displacement concept may equally be applied to the cracks in Mode II. In this mode the relative sliding displacement occurs by means of slip due to crack tip deformation. If the maximum of this displacement is employed as a crack-tip sliding displacement (CTSD), denoted by ΔS, then the crack growth length, ΔC, may be expressed as

$$\Delta C = \Delta S - \Delta C_w \qquad (4.2)$$

where ΔC_w is the length of rewelding. As for ΔC_w there is no satisfactory criterion. According to Kikukawa et al. [88] rewelding is affected by environmental conditions for the Mode I case. However, in Mode II they found that the length of rewelding and therefore, the crack growth length

does not seem to differ discernably between the air and vacuum tests. Moreover, the ratio of ΔC/ΔS was found to be nearly 0.16, which is fairly small in comparison with the ratio of ΔC/COD (∿0.55) for Mode I in their study.

As implied by Kikukawa et al.'s study a crack can grow to the point where the fracture conditions are satisfied. These conditions may be addressed in terms of fracture strain, γ_f. If the material element at a distance r_f from the crack tip attains the fracture strain, actual fracture will occur up to this point. The strain γ_{xy} along the distance r from the crack tip can be written as

$$\gamma_{xy} = K_\epsilon /(r/r_0)^m \qquad (4.3)$$

where K_ϵ is the strain intensity factor, r_0 is a characteristic distance used for non-dimensionalization, and m is the parameter which depends on the strain hardening exponent. For a non-hardening material in the HRR field m is unity. Therefore, r_f may be obtained by substituting γ_f for γ_{xy} in Eq. 4.3

$$r_f = r_0 (K_\epsilon /\gamma_f)^{-m}. \qquad (4.4)$$

Fig. 4.10 shows the shear strain distribution calculated for different depths of crack location as a function of the distance from the left tip. From the figure we may argue that if γ_f is 0.4 or so, then the cracks extend by ∿0.004 μm for d = 5 μm and ∿0.03 μm for d = 2.5 μm.

When a crack grows continuously, it is expected that the deformation
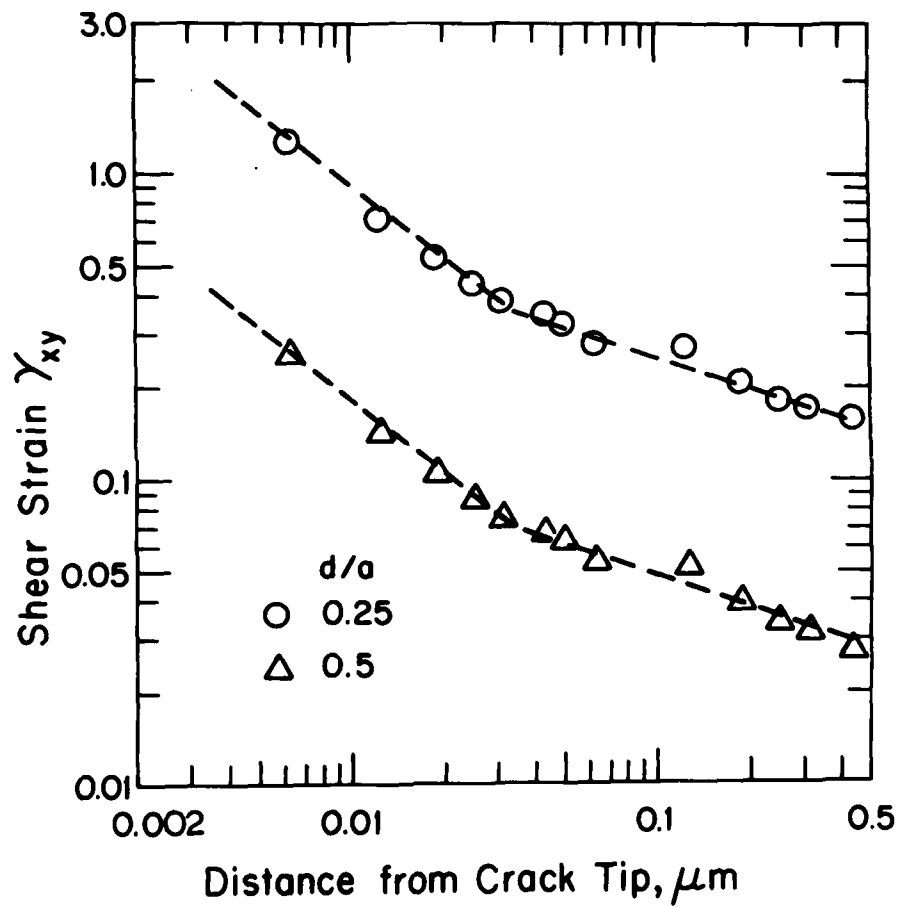
Fig. 4.10 Shear strain as a function of distance from the
left tip for different depths of crack location.

field will change. Analytic investigations of extending cracks are limited to Mode III conditions [65, 79, 96] because of mathematical complexity. For Mode I, only the general functional form of the near tip singular strain field is known for elastic-perfectly plastic materials [79]. These studies have shown that the strain field ahead of an extending crack is dominated by a logarithmic singularity which is weaker than the 1/r singularity experienced at the tip of a stationary crack. Finite element solutions to extending crack problems include simulation of crack advance by using a nodal release technique [97-99]. In this method nodes are released along the crack extension path in a predetermined way, thereby propagating the crack the length of one or more elements. The main objective of the simulation work is to identify possible macroscopic parameters which characterize the deformation field at the growing crack tip. This type of fracture characterization is beyond the scope of the present issue.

In summary, the propagation of subsurface cracks in wear can be characterized by such fracture parameters as the crack-tip sliding displacement and the fracture strain. For accurate numerical results it is essential to use specially designed crack tip elements. The isoparametric triangular elements with 1/r singularity seem to be well fitted to the requirements. Unfortunately, this element is only for elastic-perfectly plastic material.

As noticed the present investigation is limited to the case of $\mu = 0.25$ due to the prohibitively expensive computer cost. For extensive study of crack propagation a low cost method is needed. In the study of crack behavior in the rail head under the rolling condition McClintock [52]

has shown that the boundary integral method is effective with reasonable cost. For his problem the residual stress at the shakedown limit, superimposed on a repeated rolling load small enough for small scale yielding around a horizontal crack buried at the point of maximum shakedown stress, was used for the boundary conditions. Here, we wish to consider stresses above the shakedown limit, so the plastic zone extends to infinity in the x direction. In retrospect, this could have done with periodic boundary conditions. It should be used in the future.

5. THE DELAMINATION WEAR

5.1 Introduction

It was shown in Chapter 2 that asperity deformation, plowing by wear particles and hard asperities, and adhesion are responsible for friction. These friction generating mechanisms are quite important in understanding the delamination wear mechanisms. In Chapter 3 and 4 the subsurface cracks in wear were shown to be likely to grow in a ductile manner. The quantitative model of wear is described using the crack propagation model and the implication of the mechanisms of friction and crack propagation is discussed in this chapter.

5.2 The Wear Model

Consider a subsurface crack lying below the surface as shown in Fig. 5.1. An asperity is moving over the surface from left to right. The wear rate will be dictated by the crack propagation at both ends, L and R. The crack propagation for the i th cycle, ΔC_i, may be expressed as

$$\Delta C_i = f(\mu, d, C, \text{material properties}) \tag{5.1}$$

for both ends. If N is the total number of asperity passes required for removal of one layer, the volume V_1 for one crack of width w lying at a depth d is obtained as

$$V_1 = w \cdot d \cdot \sum_i^N (\Delta C_{L_i} + \Delta C_{R_i}). \tag{5.2}$$
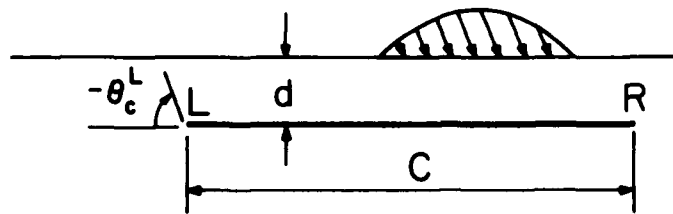
Fig. 5.1 A subsurface crack under a moving asperity.

Therefore, the total volume V for one layer may be given by

$$V = N_c \cdot N_w \cdot w \cdot d \cdot \sum_i^N (\Delta C_{L_i} + \Delta C_{R_i}) \qquad (5.3)$$

where N_c is the number of cracks along the sliding direction and N_w is the number of wear sheets in the direction of contact width. Since $N_w \times w$ is in the order of the contact width L_w, the volume V becomes

$$V = N_c \cdot L_w \cdot d \cdot \sum_i^N (\Delta C_{L_i} + \Delta C_{R_i}). \qquad (5.4)$$

Let λ be the asperity contact spacing, ℓ_c the crack spacing, D the diameter of a specimen, and L the contact length as shown in Fig. 5.2. Using this model the numbers N_c and N can be determined for a specimen and a slider, respectively.

Specimen:

Since the number of asperities per length of contact is L/λ, the number N is determined as

$$N = \frac{S}{\pi D} \frac{L}{\lambda} \qquad (5.5)$$

where S is the sliding distance required for removal of one layer. Also, N_c is given by

$$N_c = \pi D / \ell_c. \qquad (5.6)$$
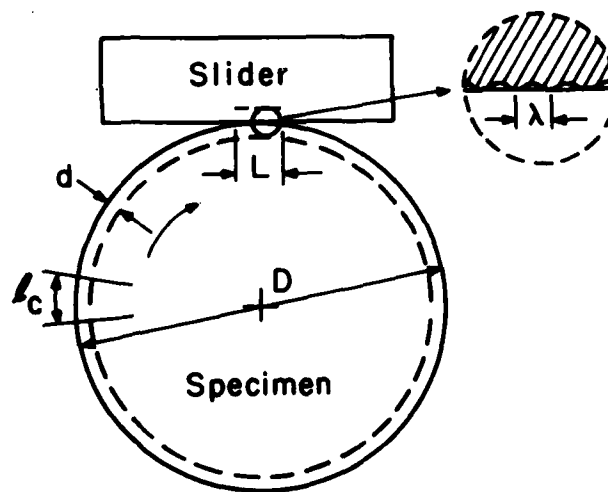
Fig. 5.2 A model of wearing specimen and slider.

The wear rate is, by assuming $L_w = L$, finally obtained as

$$\frac{V}{S} = \frac{L^2 \cdot d \cdot (\Delta \overline{C}_L + \Delta \overline{C}_R)}{\lambda \cdot \ell_c} \qquad (5.7)$$

where $\Delta \overline{C}_L$ and $\Delta \overline{C}_R$ are the average crack propagation rates during N cycles.

Slider:

The numbers N and N_c are given by

$$N = \frac{S}{\lambda} \qquad (5.8)$$

and

$$N_c = \frac{L}{\ell_c} \qquad (5.9)$$

respectively. Therefore, the wear rate for a slider is obtained as

$$\frac{V}{S} = \frac{L^2 \cdot d \cdot (\Delta \overline{C}_L + \Delta \overline{C}_R)}{\lambda \cdot \ell_c} \qquad (5.10)$$

which is the same expression as given in Eq. 5.7 for a specimen. The wear coefficient K can also be obtained by using Archard's equation as

$$K = \frac{3H \cdot L^2 \cdot d \cdot (\Delta \overline{C}_L + \Delta \overline{C}_R)}{W \cdot \lambda \cdot \ell_c} \qquad (5.11)$$

where H is the hardness of the material and W is the applied load. According to Gupta and Cook [14], the number of asperity contacts, n, increases by the 0.91 power and the area of each contact grows only by the 0.09 power of applied normal load. Therefore, we may practically assume the following linear relationship between the real area of contact, A_r or $n\pi r_0^2$, and the applied load,

$$n\pi r_0^2 = W/H \tag{5.12}$$

where r_0 is the average radius of asperity contact. On the other hand, the asperity spacing, λ, is proportional to $L/\sqrt{n}$ if we assume a square array of asperity contacts and therefore,

$$K \propto \frac{3d \cdot (\Delta \overline{C}_L + \Delta \overline{C}_R) \cdot \lambda}{\pi \cdot r_0^2 \cdot \ell_c} \tag{5.13}$$

showing that K is expressed in terms of the crack parameters (d, ℓ_c, $\Delta\overline{C}$'s) and asperity contact parameters (r_0, λ). All the parameters involved in deriving Eq. 5.13 are summarized in Table 5.1.

At present the validity of the wear model described in Eq. 5.11 can only be checked by estimating those parameters. Micrographs of worn specimens show that d is of the order of 5 μm [41]. Estimation of λ from contact geometry was shown to be of the order of 100 μm. (According to Gupta [102], λ is about 300 μm.) For the values of $\Delta\overline{C}$'s the data obtained in Chapter 4 are used and the crack spacing ℓ_c is assumed to be of the same order as of λ. In the following two examples the order of magnitude estimate for K is shown to be in the ball park although it is

Table 5.1. List of the Parameters Used for Deriving Eq. 5.13

λ	asperity contact spacing
ℓ_c	crack spacing
$\Delta \overline{C}$	average crack growth
ΔC_i	crack growth for the i th cycle of loading
d	depth of crack location
n	number of asperity contacts
r_o	average radius of asperity contact
w	crack width
A_r	real area of contact
D	diameter of a specimen
H	hardness of the material
L	apparent contact length
L_w	apparent contact width
N	total number of asperity passes required for removal of one layer
N_c	number of cracks along the sliding direction
N_w	number of wear sheets in the direction of width
S	sliding distance required for removal of one layer
V	total volume of one layer worn
V_1	volume of one crack of width w and thickness d
W	applied normal load

still premature to conclude anything further.

Example 1:

The crack tip sliding diaplacement for d = 5 μm is 0.0035 μm (Table 4.1). If $\Delta\bar{C}_L = \Delta\bar{C}_R = 0.0035$ μm and the apparent contact length L = 2 mm and both the asperity contact spacing λ and the crack spacing ℓ_c are assumed to be 100 μm, then

$$\frac{V}{S} = \frac{(2 \times 10^{-3})^2 (5 \times 10^{-6})(0.007 \times 10^{-6})}{(100 \times 10^{-6})(100 \times 10^{-6})} = 1.4 \times 10^{-11} \text{ m}^3/\text{m}$$

and for H = 100 kg/mm^2 and W = 1 kg,

$$K = \frac{3 \times 100 \times 10^6 \times 1.4 \times 10^{-11}}{1} = 4.2 \times 10^{-3}$$

Example 2:

For d = 2.5 μm, by taking $\Delta\bar{C}_L = \Delta\bar{C}_R = 0.014$ μm again from Table 4.1,

$$\frac{V}{S} = \frac{(2 \times 10^{-3})^2 (2.5 \times 10^{-6})(0.028 \times 10^{-6})}{(100 \times 10^{-6})(100 \times 100^{-6})} = 2.8 \times 10^{-11} \text{ m}^3/\text{m}$$

and

$$K = 8.2 \times 10^{-3}$$

According to the experimental results listed in Table 2.3, K is

between 10^{-2} and 10^{-4} in most cases, indicating that at least the modeling of wear by the crack propagation study is in the right direction. The limitations on the model are discussed below.

5.3 Discussion on Delamination Wear

The delamination wear model described in the previous section was seen to be able to predict the wear behavior of materials. However, the present study is too limited to draw any decisive conclusion. In order to generalize the model a systematic parametric study is required. This should include a large amount of finite element analysis work which is prohibitively expensive.

Some factors such as friction and fracture parameters are seen to affect the delamination wear greatly. High wear rates are expected when the coefficient of friction is high and the fracture strain of the material worn is low. Although our understanding of the mechanisms of friction and crack propagation has been improved much, there are still certain limitations remaining. In this section the implications and limitations of those factors and some other aspects in delamination wear are discussed. Because of the limited result only qualitative discussion can be given. Both the FEM solutions for elastic-plastic solids in Chapter 4 and for elastic solids in Chapter 3 are used to make rough estimates.

5.3.1 Subsurface Crack Propagation

Eq. 5.7 shows that the wear rate is directly proportional to the depth of crack and the average crack growth. The amount of crack growth ΔC depends on the depth d. The results in Chapter 4 indicate

that ΔC increases with decreasing d for a given friction coefficient of 0.25. For higher μ the same tendency is expected.

The reason for the ΔC dependence on d may be explained in terms of shear strain concentration at crack tips. Under the moving load condition it is highly likely that the plastic deformation is much more severe at the crack tips near the surface due to sliding between crack surfaces even for low friction. However, the analysis of crack nucleation [36] has shown that cracks cannot nucleate at very near the surface because of high triaxial state of compressive stress.

For a longer crack much larger shear concentration is expected due to relatively easier sliding of crack surfaces with respect to each other. Of course, this sliding may be retarded when the shear traction *between the crack* surfaces exists. At any rate, the crack propagation rate will increase with increasing total crack length.

When the total crack length reaches a certain size that is critical for unstable crack propagation leading to fracture, the direction of crack propagation will change toward the surface, eventually forming a wear sheet. Fracture criteria for combined mode of loading considered in Chapter 3 may provide a qualitative explanation for this. Let us consider a subsurface crack under a moving asperity shown in Fig. 5.1 again. If the left tip L is in the tensile zone behind the load, then the maximum hoop stress and the minimum strain-energy-density factor criteria predict the crack growth of about -70° at the left tip. When the critical condition is reached with tensile component, the crack will be fractured to the surface. Micrographs of wear sheets about to delaminate show that subsurface cracks always reach the surface at the trailing edge of the crack [35].

Material properties such as strain-hardening property are the
important factors affecting crack propagation ΔC. Also, the anisotropy
of the properties are expected to affect ΔC. Due to repeated loading
effects of cyclic hardening, cyclic softening and the Bauschinger
effect are also important. However, it seems impossible at the present
time to incorporate all these factors in the analysis because of extreme
complexity. The fracture strain is the simplest parameter that can be
used in determining ΔC.

5.3.2 Effects of Friction on Delamination Wear

In order to understand the delamination wear mechanisms the
understanding of such friction mechanisms as asperity deformation, plowing
and adhesion is quite important for the following reasons:

(1) Although the overall coefficient of friction can reach a
large value, the local surface traction at any one of the contacts
cannot have a shear stress larger than that predicted by plasticity for
a given type of contact. That is, the shear stress at a flat contact
cannot exceed 0.4 times the normal stress if all the normal load is
carried by flat contacts. Likewise, the tangential stress exerted by
plowing particles cannot be larger than the normal stress since the
maximum value of plowing compone, t of friction cannot be larger than 1.0.

(2) The deformation of asperities and the plowing action will
always occur, generating wear particles, since delamination wear keeps
creating wear particles and surface asperities.

(3) All these three forms of surface interactions induce the
subsurface deformation, crack nucleation and propagation, eventually

causing delamination wear. When plowing is the primary cause of surface traction, the surface will show many grooves and remain rough. On the other hand, adhesion and asperity interaction will tend to leave a relatively smooth surface.

From the computation point of view, the above considerations can raise an important question: How can the contact be modeled when the coefficient of friction is much larger than that possible in terms of yield criteria? This is more serious when the material model is elastic-perfectly plastic. There is no satisfactory answer to this at present. For a perfectly flat contact, the slip line solution indicates that the normal stress decreases from $(2 + \pi)k$ to $(1 + 0.5\pi)k$ with increasing friction. This implies that the real area of contact should increase twice, on which no definitive experimental evidence is available at this time. When the other two components of friction are present in addition to adhesion, it is even more difficult.

Experimentally it is well known that the wear behavior of materials strongly depends on the coefficient of friction [3, 4]. High shear strain distribution is expected ahead of extending cracks when the coefficient of friction is high. Therefore, the crack propagation rate is larger for higher friction coefficient. The exact relation between friction and wear cannot be given because of limited data. However, the elastic solutions obtained in Chapter 3, although they have already been shown to be inadequate, may be used to discuss the functional relation qualitatively.

In Figs. 5.3 and 5.4 the maximum Mode II stress intensity factors for a given d are plotted as a function of friction coefficient μ.
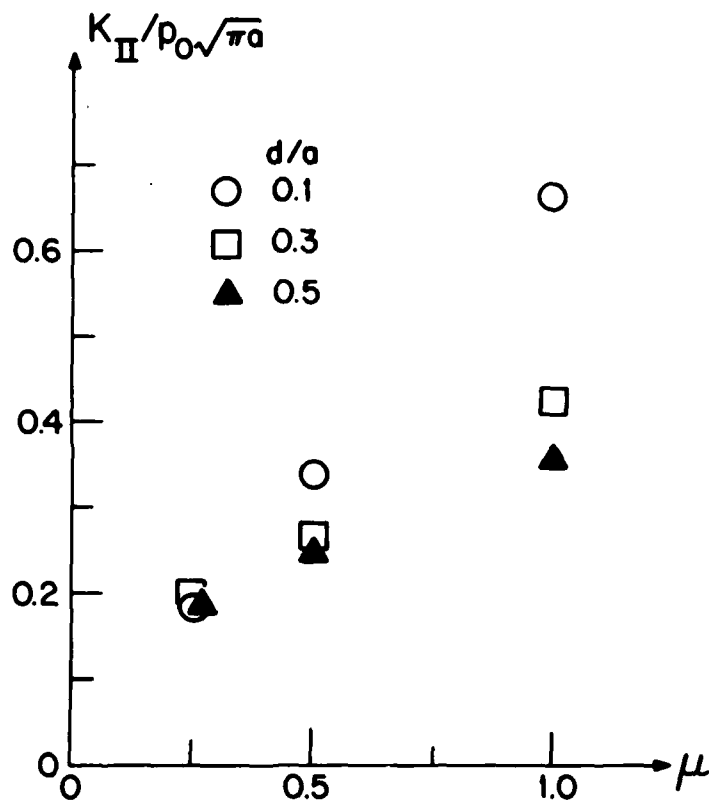
Fig. 5.3 Normalized K_{II} as a function of μ: $c = 1/4a$; left tip.
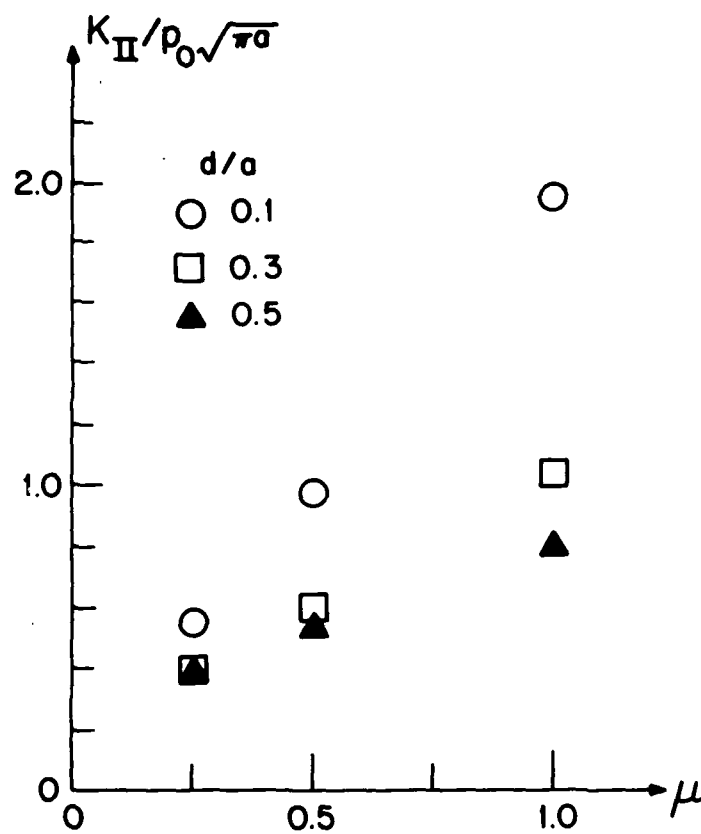
Fig. 5.4 Normalized K_{II} as a function of μ: c = 3a; left tip.

It can be seen that the relation between K_{II} and μ is approximately linear for a given d. If we assume that Paris' crack growth law is still valid in this case, then the crack growth ΔC may be expressed as

$$\Delta C \sim (a\mu)^b \qquad (5.14)$$

where a is a constant. Since the wear volume is determined by the amount of the total ΔC accumulated, wear rates are a power function of friction. The exponent b is a constant which varies from 2 to 4 depending on material for ΔK values in stage II. This should give a rough idea about a functional relation between friction and wear, although the foregoing discussion is very approximate and may not be valid for subsurface crack propagation in wear.

When ΔK is less than the value in stage II or the threshold value, normally this is the case when the applied load is small, Eq. 5.14 is not applicable. For the case we may assume the following functional form:

$$\frac{dC}{dN} = f(r_p) \qquad (5.15)$$

where r_p is the plstic zone size given by Eq. 3.3. To determine the function f the strain distribution in the plstic zone and the fracture strain should be known. However, it does not seem to be possible now. If we assume the following linear form as a first approximation,

$$f(r_p) = \alpha r_p \qquad (5.16)$$

then the exponent b in Eq. 5.14 is 2 and Eq. 5.15 becomes

$$\frac{dC}{dN} = \frac{\alpha}{2\pi} \left(\frac{\Delta K_{II}}{k}\right)^2 \tag{5.17}$$

where α is a constant. Since $\Delta K_{II} = \beta p_o \sqrt{C}$ for a given d, Eq. 5.17 can be written as

$$\frac{dC}{dN} = \frac{\alpha}{2\pi} \left(\frac{\beta p_o}{k}\right)^2 \cdot C \tag{5.18}$$

and integrating both sides after separation yields to

$$C = C_o \exp\left[\frac{\alpha}{2\pi} \left(\frac{\beta p_o}{k}\right)^2 \cdot N\right] \tag{5.19}$$

where C_o and β are constants. Therefore, the wear volume V, using Eq. 5.4, is obtained as

$$V = N_c \cdot L_w \cdot d \cdot 2C_o \exp\left[\frac{\alpha}{2\pi} \left(\frac{\beta p_o}{k}\right)^2 \cdot N\right]. \tag{5.20}$$

All the parameters used for deriving Eq. 5.20 are summarized in Table 5.2. To use this expression to estimate the wear volume, all the constants should be determined first and more fundamentally, the exact form of f in Eq. 5.15 should be known.

5.4 Conclusions

(1) The wear equation in the delamination theory is promising in predicting the wear of materials.

(2) The subsurface crack propagation in wear can be determined

Table 5.2. List of the Parameters Used for Deriving Eq. 5.20

α, β	proportionality constants
ΔK_{II}	Mode II stress intensity factor range
a	proportionality constant
b	exponent
d	depth of crack location
k	shear yield stress of the material
P_o	maximum stress value at the center of asperity contact
C_o	constant of integration
L_w	apparent contact width
N	total number of asperity passes required for removal of one layer
N_c	number of cracks along the sliding direction

by such plastic fracture parameters as crack-tip sliding
displacement and fracture strain.

(3) The wear rate of material is expected to be a power function
of the coefficient of friction when the test conditions are
identical.

6. SUMMARY AND CONCLUSIONS

The experimental and theoretical investigation reported in this study verified the hypothesis of the delamination theory of wear which states that wear occurs as a result of force transmission, plastic deformation, crack nucleation, crack propagation, and wear sheet formation. The theoretical anlyais indicated that the wear rate of metals can be predicted by friction and crack propagation information.

Studies were carried out on the friction mechanisms, showing that the coefficient of friction between the sliding surfaces is due to the combined effects of asperity deformation, plowing by wear particles and hard surface asperities, and adhesion between the flat surfaces. It was found that the frictional behavior of materials is history dependent and can successfully be represented in the "Friction Space" diagram shown in Fig. 2.18. Further, the compatibility of sliding surfaces was found to be governed as much by mechanical properties of materials as by the adhesion between the two surfaces. This investigation indicated that to incorporate all the effects of friction components into modeling of sliding contact for deformation study further research is required, particularly for the case of complicated contact geometry.

Studies on the crack propagation in wear indicated that a subsurface crack grows in the direction parallel to the surface until a critical state is reached at the trailing edge of the crack, turning the direction toward the surface. Considerations on the plastic zone at the crack tip and the threshold stress intensity factors suggested that the linear

elastic fracture mechanics approach is inadequate for subsurface cracks in sliding wear. As expected from the result of Johnson and Jefferis [103] a semi-infinite solid under the cyclic moving load was found not to reach shakedown for p_0 = 4k and μ = 0.25 if the material model is elastic-perfectly plastic. Such fracture parameters as crack-tip sliding displacement and fracture strain were found to be useful for characterization of crack tip field. For a complete characterization of crack propagation further research is required in the field of fracture mechanics as well as in wear.

Finally, the delamination wear equation given as Eq. 5.11, which was derived using the crack propagation model, was found to be promising in predicting the wear of materials. Due to limited data in the crack propagation study for the elastic-plastic solids, anything decisive such as the exact relation between friction and wear cannot be determined. However, the rough estimate by the calculated stress intensity factors indicated that there is a power functional relation between friction and wear although the stress intensity factor approach was shown to be inadequate. When the applied load is small, the plastic zone size estimated by the stress intensity factor may be useful in deriving the crack growth, and therefore, the wear volume, which was shown in Eq. 5.15 through Eq. 5.20. For this purpose, further research should be done to determine the relation between crack growth rate and plastic zone size.

REFERENCES

1. D. Dowson, "The Early History of Tribology," First European Tribology Congress, Inst. Mech. Eng., London, 1973, pp. 1-14.

2. N. P. Suh, "The Delamination Theory of Wear," Wear, Vol. 25, 1973, pp. 111-124.

3. M. Tohkai, "Microstructural Aspects of Friction," S. M. Thesis, Department of Mechanical Engineering, M. I. T., 1979.

4. E. Rabinowicz, "The Dependence of the Adhesive Wear Coefficient on the Surface Energy of Adhesion," Wear of Materials - 1977, ASME, New York, 1977, pp. 36-40.

5. F. P. Bowden and D. Tabor, Friction and Lubrication of Solids, Clarendon Press, Oxford, Part I, 1950, pp. 87.

6. R. Holm, "The Friction Force Over the Real Area of Contacts," Wiss. Veroff. Simens-Werk, Vol. 17, 1938, pp. 38-49.

7. H. Ernst and M. E. Merchant, "Surface Friction Between Metals -- A Basic Factor in the Metal Cutting Process," Proc. Special Summer Conf. on Friction and Surface Finish, 1940, M. I. T. Press, Cambridge, 1969, pp. 76-101.

8. F. P. Bowden and D. Tabor, "The Area of Contact Between Stationary and Between Moving Surfaces," Proc. R. Soc. London, Ser. A, Vol. 169, 1939, pp. 391-405.

9. F. P. Bowden, A. J. W. Moore and D. Tabor, "The Ploughing and Adhesion of Sliding Metals," J. Appl. Phys., Vol. 14, 1943, pp. 80-91.

10. J. S. McFarlane and D. Tabor, "Relation Between Friction and Adhesion," Proc. R. Soc. London, Ser. A, Vol. 202, 1950, pp.244-253.

11. J. S. Courtney-Pratt and E. Eisner, "The Effect of a Tangential Force on the Contact of Metallic Bodies," Proc. R. Soc. London, Ser. A, Vol. 238, 1957, pp. 529-550.

12. D. Tabor, "Junction Growth in Metallic Friction: The Role of Combined Stresses and Surface Contamination," Proc. R. Soc. London, Ser. A, Vol. 251, 1959, pp. 378-393.

13. A. P. Green, "Friction Between Unlubricated Metals: A Theoretical Analysis of the Junction Model," Proc. R. Soc. London, Ser. A, Vol. 228, 1955, pp. 191-204.

14. P. K. Gupta and N. H. Cook, "Statistical Analysis of Mechanical Interaction of Rough Surfaces," J. Lub. Tech., Vol. 94, 1972, pp. 19-26.

15. A. P. Green, "The Plastic Yielding of Metal Junctions Due to Combined Shear and Pressure," J. Mech. Phys. Solids, Vol. 2, 1954, pp. 197-211.

16. P. K. Gupta and N. H. Cook, "Junction Deformation Model for Asperities in Sliding Interaction," Wear, Vol. 20, 1972, pp. 73-87.

17. I. V. Kragel'skii, "Friction Interaction of Solids," Soviet J. Friction and Wear, Vol. 1, 1980, pp. 7-20.

18. T. Kayaba and K. Kato, "Theoretical Representation of the Coefficient of Friction for Multiple Contact Points," Wear, Vol. 52, 1979, pp. 117-132.

19. J. M. Challen and P. L. B. Oxley, "An Explanation of the Different Regimes of Friction and Wear Using Asperity Deformation Models," Wear, Vol. 53, 1979, pp. 22'-243.

20. E. Rabinowicz, "Influence of Surface Energy on Friction and Wear Phenomena," J. Appl. Phys., Vol. 32, 1961, pp. 1440-1444.

21. E. Rabinowicz, "Practical Uses of the Surface Energy Criterion," Wear, Vol. 7, 1964, pp. 9-22.

22. E. Rabinowicz, "The Determination of the Compatibility of Metals Through Static Friction Tests," ASLE Trans., Vol. 14, 1971, pp. 198-205.

23. D. H. Buckley, "Definition and Effect of Chemical Properties of Surfaces in Friction, Wear and Lubrication," Proc. Int. Conf. on the Fundamentals of Tribology, edited by N. P. Suh and N. Saka, 1978, M. I. T. Press, Cambridge, 1980, pp. 173-199.

24. M. C. Shaw and E. F. Macks, Analysis and Lubrication of Bearings, McGraw-Hill, New York, 1949, pp. 457-461.

25. T. Liu, "Sliding Friction of Copper," Wear, Vol. 7, 1964, pp. 163-174.

26. N. P. Suh and P. Sridharan, "Relationship Between the Coefficient of Friction and the Wear Rate of Metals," Wear, Vol. 34, 1975, pp. 291-299.

27. Y. Tsuya, Microstructures of Wear, Friction and Solid Lubrication, Tech. Rep. No. 81, Mechanical Engineering Laboratory, Tokyo, 1976.

28. D. A. Rigney and J. P. Hirth, "Plastic Deformation and Sliding Friction of Metals," Wear, Vol. 53, 1979, pp. 345-370.

29. D. Kuhlmann-Wilsdorf, Dislocation Concepts in Friction and Wear, Tech. Rep. to ONR, Research Laboratories for the Engineering Sciences, University of Virginia, Charlottesville, 1980.

30. E. P. Abrahamson, II, S. Jahanmir and N. P. Suh, "The Effect of Surface Finish on the Wear of Sliding Surfaces," CIRP Ann., Int. Inst. Prod. Eng. Res., Vol. 24, 1975, pp. 513-514.

31. R. Holm, Electrical Contacts Handbook, Springer-Verlag, Berlin, 1958.

32. J. T. Burwell and C. D. Strang, "On the Empirical Law of Adhesive Wear," J. Appl. Phys., Vol. 23, 1952, pp. 18-32.

33. J. F. Archard, "Contact and Rubbing of Flat Surfaces," J. Appl. Phys., Vol. 24, 1953, pp. 981-998.

34. N. P. Suh and co-workers, The Delamination Theory of Wear, Elesevier, 1977.

35. S. Jahanmir and N. P. Suh, and E. P. Abrahamson,II, "Microscopic Observations of the Wear Sheet Formation by Delamination," Wear, Vol. 28, 1974, pp. 235-249.

36. S. Jahanmir and N. P. Suh, "Mechanics of Subsurface Void Nucleation in Delamination Wear," Wear, Vol. 44, 1977, pp. 17-38.

37. J. F. Fleming and N. P. Suh, "Mechanics of Crack Propagation in Delamination Wear," Wear, Vol. 44, 1977, pp. 39-56.

38. D. A. Hills and D. W. Ashelby, "On the Application of Fracture Mechanics to Wear," Wear, Vol. 54, 1979, pp. 321-330.

39. A. R. Rosenfield, "A Fracture Mechanics Approach to Wear," Wear, Vol. 61, 1980, pp. 125-132.

40. L. M. Keer, M. D. Bryant and G. K. Haritos, "Subsurface Cracking and Delamination," Solid Contact and Lubrication, ASME Publication, A. M. D., Vol. 39, 1980, pp. 79-95

41. S. Jahanmir, "A Fundamental Study of the Delamination Theory of Wear," Ph. D. Thesis, Department of Mechanical Engineering, M. I. T., 1977.

42. F. Willett, S. M. Thesis, Department of Mechanical Engineering, M. I. T., in progress.

43. S. Shepard, "The Effects of Ion Implantation on Friction and Wear of Metals," S. M. Thesis, Department of Mechanical Engineering, M. I. T., 1981.

44. N. P. Suh, H.-C. Sin, M. Tohkai and N. Saka, "Surface Topography and Functional Requirements for Dry Sliding Surfaces," CIRP Ann. Int. Inst. Prod. Eng. Res., Vol 29, 1980, pp. 413-418.

45. K. Kuwahara and Masumoto, "Influence of Wear Particles on the Friction and Wear Between Copper Disk and Pin of Various Kinds of Metal," J. Jpn. Soc. Lubr. Eng., Vol. 25, 1980, pp. 126-131.

46. S. Kato, E. Marui, A. Kobayashi and T. Matsubayushi, "Characteristics of Surface Topography and Static Friction on Scraped Surface Slideway, Part I and Part II," J. Eng. Ind., Vol. 103, 1980, pp. 97-108.

47. H.-C. Sin, N. Saka and N. P. Suh, "Abrasive Wear Mechanisms and the Grit Size Effect," Wear, Vol. 55, 1979, pp. 163-190.

48. J. Goddard and H. Wilman, "A Theory of Friction and Wear During the Abrasion of Metals," Wear, Vol. 5, 1962, pp. 114-135.

49. E. Rabinowicz, Friction and Wear of Materials, Wiley, New York, 1965, pp. 51-108.

50. N. P. Suh, New Theories of Wear and Their Implications for Tool Materials," Wear, Vol. 62, 1980, pp. 1-20.

51. J. L. Swedlow, "Criteria for Growth of the Angled Crack," Cracks and Fracture, ASTM STP 601, 1976, pp. 506-521.

52. F. A. McClintock, "Plastic Flow Around a Crack Under Friction and Combined Stress," Fracture 1977, edited by D. M. R. Taplin, Vol. 4, Waterloo, Canada, 1977, pp. 49-64, Pergamon, Oxford, 1978.

53. R. O. Ritchie, "On the Relationship Between Delamination Wear and the Initiation and Growth of Fatigue Cracks in Ultrahigh Strength Steel," Proc. Int. Conf. on the Fundamentals of Tribology, edited by N. P. Suh and N. Saka, 1978, M. I. T. Press, Cambridge, 1980, pp. 127-134.

54. K.-J. Bathe and E. L. Wilson, Numerical Methods in Finite Element Analysis, Prentice-Hall, Englewood Cliffs, 1976.

55. R. D. Henshell and K. G. Shaw, "Crack Tip Finite Elements Are Unnecessary," Int. J. Num. Meth. Eng., Vol. 9, 1975, pp. 495-507.

56. R. S. Barsoum, "On the Use of Isoparametric Finite Elements in Linear Fracture Mechanics," Int. J. Num. Meth. Eng., Vol. 10, 1976, pp. 25-37.

57. R. S. Barsoum, "Triangular Quarter-Point Elements as Elastic and Perfectly Plastic Crack Tip Elements," Int. J. Num. Meth. Eng., Vol. 11, 1977, pp. 85-98.

58. F. Erdogan and G. C. Sih, "On the Crack Extension in Plates Under Plane Loading and Transverse Shear," J. Basic Eng., Vol. 85, 1963, pp. 519-527.

59. G. C. Sih, "Strain-Energy-Density Factor Applied to Mixed Mode Crack Problems," Int. J. Fracture, Vol. 10, 1974, pp. 305-321.

60. P. J. E. Forsyth, "A Two Stage Process of Fatigue Crack Growth," Proc. Crack Propagation Symposium, Cranfield, Vol. 1, 1961, pp. 76-94.

61. V. A. Tipnis and N. H. Cook, "The Influence of Stress-State and Inclusion Content on Ductile Fracture With Rotation," J. Basic Eng., Vol. 89, 1967, pp. 533-540.

62. R. A. Smith, Interfaces of Wear and Fatigue," Proc. Int. Conf. on the Fundamentals of Tribology, edited by N. P. Suh and N. Saka, 1978, M. I. T. Press, Cambridge, 1980, pp. 605-616.

63. W. T. Shieh, "Compressive Maximum Shear Crack Initiation and Propagation," Eng. Fracture Mech., Vol. 9, 1977, pp. 37-54.

64. P. M. Besuner, "Fracture Mechanics Analysis of Rails with Shell-Initiated Transverse Cracks," Rail Steels--Developments, Processing, and Use, ASTM STP 644, 1978, pp. 303-329.

65. F. A. McClintock and G. R. Irwin, "Plasticity Aspects of Fracture Mechanics," Fracture Toughness Testing and Its Applications, ASTM STP 381, 1965, pp. 84-113.

66. V. Weiss and D. N. Lal, "A Note on the Threshold Condition for Fatigue Crack Propagation," Met. Trans., Vol. 5, 1974, pp. 1946-1949.

67. K.-J. Bathe, ADINA--A Finite Element Program for Automatic Dynamic Incremental Nonlinear Analysis, Report 82448-1, Acoustics and Vibration Laboratory, M. I. T., 1975.

68. K.-J. Bathe, Static and Dynamic Geometric and Material Nonlinear Analysis Using ADINA, Report 82448-2, Acoustics and Vibration Laboratory, M. I. T., 1976.

69. K.-J. Bathe and A. P. Cimento, "Some Practical Procedures for the Solution of Nonlinear Finite Element Equations," J. Comp. Meth. in App. Mech. and Eng., Vol. 22, 1980, pp. 59-85.

70. S. C. Anand, "Numerical Investigation of Stresses in the Inelastic Range in a Rolling Contact," *Proc. Second Int. Conf. on Vehicle Structural Mechanics*, Society of Automotive Engineers, 1977, pp. 121-127.

71. J. W. Hutchinson, "Singular Behavior at the End of a Tensile Crack in a Hardening Material," *J. Mech. Phys. Solids*, Vol. 16, 1968, pp. 13-31.

72. J. W. Hutchinson, "Plastic Stress and Strain Fields at a Crack Tip," *J. Mech. Phys. Solids*, Vol. 16, 1968, pp. 337-347.

73. J. R. Rice and G. F. Rosengren, "Plane Strain Deformation Near a Crack Tip in a Power-Law Hardening Material," *J. Mech. Phys. Solids*, Vol. 16, 1968, pp. 1-2.

74. J. C. Nagtegaal, D. M. Parks and J. M. Rice, "On Numerically Accurate Finite Element Solutions in the Fully Plastic Range," *J. Comp. Meth. in App. Mech. and Eng.*, Vol. 4, 1974, pp. 153-177.

75. H. G. deLorenzi and C. F. Shih, "On the Use of 2D Isoparametric Elements for Calculations in the Fully Plastic Range," *Int. J. Fracture*, Vol. 13, 1977, pp. 507-511.

76. H. G. deLorenzi and C. F. Shih, "Application on ADINA to Elastic-Plastic Fracture Problems," *Applications Using ADINA*, Proc. ADINA Conf., 1977, edited by K.-J. Bathe, Report 82448-6, Acoustics and Vibrations Laboratory, Department of Mechanical Engineering, M. I. T., 1977, pp. 349-383.

77. C. F. Shih, H. G. deLorenzi and W. R. Andrews, "Studies on Crack Initiation and Stable Crack Growth," *Elastic-Plastic Fracture,* ASTM STP 668, 1979, pp. 65-120.

78. J. R. Rice, "A Path Independent Integral and the Approximate Analysis of Strain Concentration by Notches and Cracks," *J. Appl. Mech.*, Vol. 35, 1968, pp. 379-386.

79. J. R. Rice, "Mathematical Analysis in the Mechanics of Fracture," *Fracture*, Vol. 2, Academic Press, New York, 1968, pp. 191-311.

80. J. A. Begley and J. D. Landes, "The J Integral as a Fracture Criterion," *Fracture Toughnr ,*, ASTM STP 514, 1972, pp. 1-23.

81. J. D. Landes and J. A. Begley, The Effect of Specimen Geometry on J_{IC}," *Fracture Toughness*, ASTM STP 514, 1972, pp. 24-39.

82. M. G. Dawes, "Elastic-Plastic Fracture Toughness Based on the COD and J-Contour Integral Concepts," *Elastic-Plastic Fracture*, ASTM STP 668, 1979, pp. 307-333.

83. S. N. Atluri and M. Nakagaki, "Stress Analysis of Cracks in Elasto-Plastic Range," Fracture 1977, Vol. 3A, pp. 457-462.

84. R. M. McMeeking and D. M. Parks, "On Criteria for J-Dominance of Crack-Tip Fields in Large-Scale Yielding," Elastic-Plastic Fracture, ASTM STP 668, 1979, pp. 175-194.

85. A. A. Wells, "Unstable Crack Propagation in Metals-Cleavage and Fast Fracture," Proc. Crack Propagation Symposium, Cranfield, Vol. 1, 1961, pp. 210-230.

86. J. S. Ke and H. W. Liu, "Near Tip Strain As a Ductile Fracture Criterion," Int. J. Fracture Mech., Vol. 7, 1971, pp. 487-490.

87. R. M. N. Pelloux, "Crack Extension by Alternating Shear," Eng. Fracture Mech., Vol. 1, 1970, pp. 697-704.

88. M. Kikukawa, M. Jono and M. Adachi, "Direct Observation and Mechanism of Fatigue Crack Propagation," Fatigue Mechanisms, ASTM STP 675, 1979, pp. 234-253.

89. J. R. Rice and M. A. Johnson, "The Role of Large Crack Tip Geometry Changes in Plane Strain Fracture," Inelastic Behavior of Solids, McGraw-Hill, New York, 1970, pp. 641-672.

90. A. S. Kuo and H. W. Liu, "An Analysis of Unzipping Model for Fatigue Crack Growth," Scripta Metallurgica, Vol. 10, 1976, pp. 723-728.

91. R. M. McMeeking, "Path Dependence of the J-Integral and the Role of J as a Parameter Characterizing the Near-Tip Field, Flaw Growth and Fracture, ASTM STP 631, 1977, pp. 28-41.

92. S. N. Atluri, M. Nakagaki and W.-H. Chen, "Fracture Analysis Under Large-Scale Plastic Yielding: A Finite Deformation, Embedded Singularity, Elastoplastic Incremental Finite-Element Solution," Flaw Growth and Fracture, ASTM STP 631, 1977, pp. 42-61.

93. C. F. Shih and M. C. German, "Requirements for a One Parameter Characterization of Crack Tip Fields by the HRR Singularity," Int. J. Fracture, Vol. 17, 1981, pp. 27-43.

94. D. R. Wheeler and D. H. Buckley, "Texturing in Metals as a Result of Sliding," Wear, Vol. 33, 1975, pp. 65-74.

95. H. Krause and A. H. Demirci, "Texture Changes in the Running Surface of Face-Centered Cubic Metals as the Result of Frictional Stress," Wear, Vol. 61, 1980, pp. 325-332.

96. F. A. McClintock, "Ductile Fracture Instability in Shear," J. App. Mech., Vol. 25, 1958, pp.582-588.

97. H. Andersson, "Finite Element Treatment of a Uniformly Moving Elastic-Plastic Crack Tip," J. Mech. Phys. Solids, Vol. 22, 1974, pp. 285-308.

98. K. J. Miller and A. P. Kfouri, "A Comparison of Elastic-Plastic Fracture Parameters in Biaxial Stress States," Elastic-Plastic Fracture, ASTM STP 668, 1979, pp. 214-228.

99. E. P. Sorensen, "A Numerical Investigation of Plane Strain Stable Crack Growth Under Small-Scale Yielding Conditions," Elastic-Plastic Fracture, ASTM STP 668, 1979, pp. 151-174.

100. J. E. Merwin and K. L. Johnson, "An Analysis of Plastic Deformation in Rolling Contact," Proc. Instn. Mech. Engrs., Vol. 177, 1963, pp. 676-690.

101. F. A. McClintock, "Effects of Root Radius, Stress, Crack Growth and Rate on Fracture Instability," Proc. R. Soc. London, Ser. A, Vol. 285, 1965, pp. 58-72.

102. P. K. Gupta, "Topographic Analysis of Friction Between a Pair of Rough Surfaces," Sc. D. Thesis, Department of Mechanical Engineering, M. I. T., 1970.

103. K. L. Johnson and J. A. Jefferis, "Plastic Flow and Residual Stresses in Rolling and Sliding Contact," Proc. of Symposium on Fatigue in Rolling Contact, Instn. Mech. Engrs., 1963, pp. 54-65.

APPENDIX A: SLIP-LINE FIELD SOLUTION FOR SLIDING CONTACT

Fig. A.1 gives a possible slip-line field for the asperity contact between sliding surfaces. The interface OA between asperities and the stress free surface OD are both assumed to be straight with their directions defined by the angles θ and θ' measured from the sliding direction. From the figure it can be noticed that the slip-line ABCD is a β-line. Using the Hencky relations the stresses along the slip-line can be obtained.

At D, $\qquad \phi = \theta' + \frac{\pi}{4}$ and $p = k$. $\hspace{3cm}$ (A.1)

Along AB, $\qquad \phi = \alpha - \theta + \frac{\pi}{2}$ and

$$p_{AB} = k \left(1 + \frac{\pi}{2} + 2\alpha - 2\theta - 2\theta'\right) \hspace{2cm} (A.2)$$

Isolating the junction along ABO as shown in Fig. A.2 we can find the resultant forces as

$$-F_y = L = (AB) \, p \cos (\theta-\alpha) - (AB)k \sin (\theta-\alpha)$$
$$+ (OB)k \cos (\theta-\alpha) - (OB)p \sin (\theta-\alpha) \hspace{1.5cm} (A.3)$$

$$-F_x = F = (AB)p \sin (\theta-\alpha) + (AB)k \cos (\theta-\alpha)$$
$$+ (OB)k \sin (\theta-\alpha) + (OB)p \cos (\theta-\alpha).$$

Using the geometric relations, L and F are expressed as

$$L = (OA) \, (p \cos\theta + k \sin (2\alpha-\theta)) \hspace{2.5cm} (A.4)$$

$$F = (OA) \, (p \sin\theta + k \cos (2\alpha-\theta)).$$
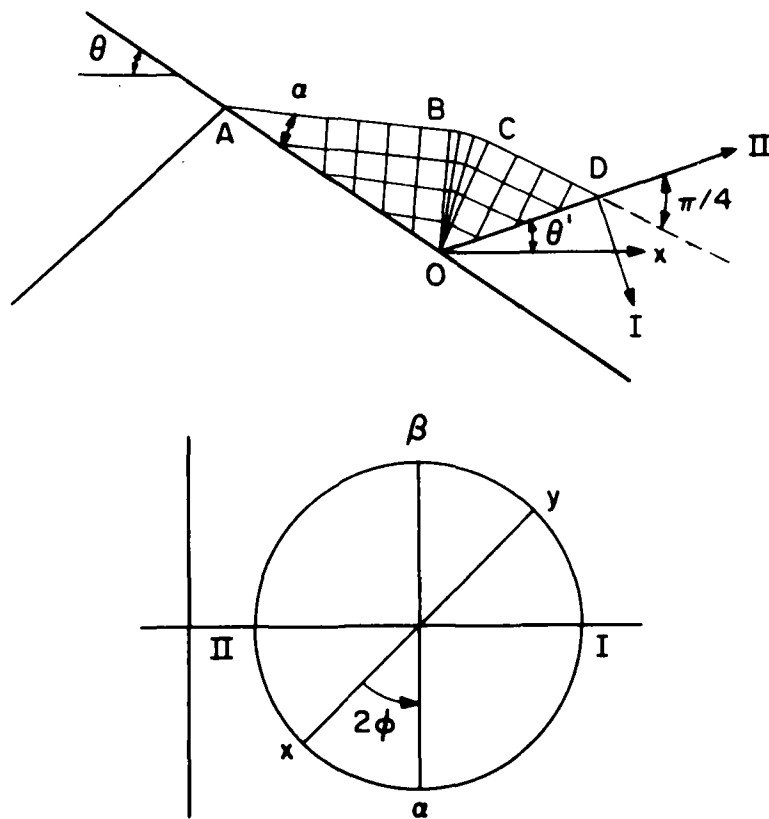
Fig. A.1 A slip- line field for an asperity contact.
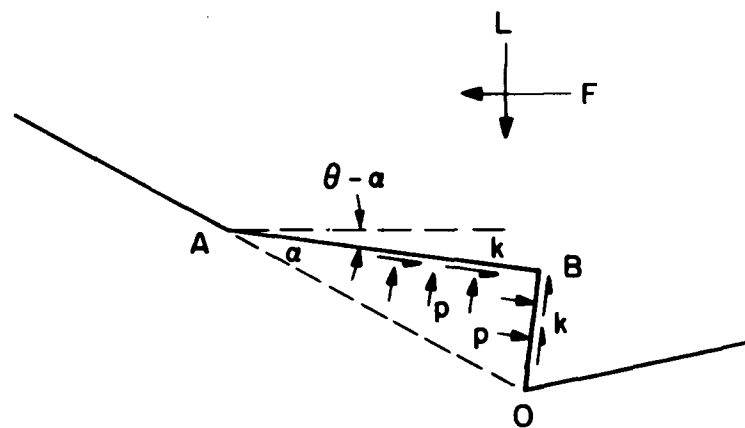
Fig. A.2 Isolation of the junction of the asperity contact
along ABO in Fig. A.1.

Therefore, the coefficient of friction is

$$\mu = \frac{F}{L} = \frac{(1 + \frac{\pi}{2} + 2\alpha - 2\theta - 2\theta') \sin\theta + \cos(2\alpha - \theta)}{(1 + \frac{\pi}{2} + 2\alpha - 2\theta - 2\theta') \cos\theta + \sin(2\alpha - \theta)} \qquad (A.5)$$

When θ, θ', and α are small (θ, θ', $\alpha \to 0$)

$$\mu = \frac{1}{1 + \frac{\pi}{2}} = 0.39.$$

For several values of α, θ, and θ', the coefficient of friction is plotted in Fig. 2.12.

If the junction does not weld along OA the shear stress along OA will be much less than k. The interfacial shear stress is related to the angle α as $\tau = k \cos 2\alpha$. When there is no shear stress along OA, i.e., $\alpha = \pi/4$, the junction will slide along OA until the junction can deform under the influence of the normal load alone. During this sliding the coefficient of friction can be obtained by substituting $\alpha = \pi/4$, into Eq. (A.5) as

$$\mu = \frac{(1 + \pi - 2\theta - 2\theta') \sin\theta + \cos(\frac{\pi}{2} - \theta)}{(1 + \pi - 2\theta - 2\theta') \cos\theta + \sin(\frac{\pi}{2} - \theta)}$$

or

$$\mu = \tan\theta$$

which is the same expression as that derived from the roughness theory of friction.

The slip-line field solution derived above is a general solution. When the sliding occurs, the slip-line field should satisfy the kinematic condition, which corresponds to the case of the slip-line AB being parallel to the sliding direction. Therefore, α is equal to θ.

APPENDIX B: PLOWING COMPONENT OF FRICTION

The plowing force P can be expressed as $P = pA_g$ where p is the flow pressure and A_g is the cross-sectional area of the grooved track. Sin et al. [B.1] have shown that the expression for the plowing component of friction μ_p given by Goddard and Wilman [B.2] is found to agree well with the experimental results. In this appendix the expression is derived following their treatment.

Let us consider a spherical particle of radius r loaded by a normal force L. Then the real area of contact, πr_0^2, is obtained by

$$\pi r_0^2 = \frac{L}{H} \qquad (B.1)$$

where r_0 is the radius of the periphery of the indentation and H is the hardness of the material. When a tangential force is applied, just sufficient to cause very slow sliding, a groove is plowed out by the particle, and the indentation must become deeper to support the same load, because the contact interface is then only on the front half of the particle. If the pile-up above the initial metal surface in front of the moving particle is not too large, the horizontal projected area of contact is virtually semicircular, the radius w/2 being such that:

$$\frac{\pi w^2}{8} = \frac{L}{p} \qquad (B.2)$$

where p is the normal pressure that is smaller than H in this case. Therefore, the plowing force can be calculated using this value of w, and taking into account that the effective flow pressure p_e applicable here may be somewhat larger than p. From the geometry of the plowed groove the cross-sectional area A_g is given by

$$A_g = r^2 \sin^{-1} \frac{w}{2r} - \frac{rw}{2} [1 - (\frac{w}{2r})^2]^{1/2} . \tag{B.3}$$

Since $\mu_p L = p_e A_g$, and using Eqs. (B.2) and (B.3),

$$\mu_p = (\frac{2}{\pi}) (\frac{p_e}{p}) [(\frac{2r}{w})^2 \sin^{-1} \frac{w}{2r} - \{(\frac{2r}{w})^2 - 1\}^{1/2}] \tag{B.4}$$

which becomes the expression given as Eq. (2.5) when $p_e \to p$.

References

B.1. H.-C. Sin, N. Saka and N. P. Suh, "Abrasive Wear Mechanisms and the Grit Size Effect," Wear, Vol. 55, 1979, pp. 163-190.

B.2. J. Goddard and H. Wilman, "A Theory of Friction and Wear During the Abrasion of Metals," Wear, Vol. 5, 1962, pp. 114-135.

APPENDIX C: STRESS INTENSITY FACTORS BY FEM

Elements with the mid-side nodes placed at the quarter point posi-
tion have been employed in Refs. [C.1] and [C.2] to obtain the mode I
stress intensity factor, K_I, for elastic crack problems. It was done
by extrapolating a displacement parameter [C.3], associated with the
crack opening profile, to the crack tip. However, it was shown by
Shih, deLorenzi, and German [C.4] that to have consistency between the
interpolating function and Williams' eigenfunction expansion [C.5]
along the edge ABC in Fig. C.1, the stress intensity factor K_I, must
be related to the nodal displacements u_A, u_B, and u_C with $u_A=0$ in most
cases by

$$K_I = \frac{2G\sqrt{2\pi}}{\kappa+1} \left(\frac{-3u_A + 4u_B - u_C}{\sqrt{L}}\right) \qquad (C.1)$$

where G is the shear modulus, κ = 3-4ν for plane strain and κ = (3-ν)/
(1+ν) for plane stress. For mixed mode loading, the stress intensity
factors can be obtained by relating the stresses given by FEM to those
by eigenfunction expansion. This is treated here.

The geometry of an 8-noded plane isoparametric element is mapped
into the normalized square space (t, s), (-1$\leq$t$\leq$1, -1$\leq$S$\leq$1) through the
transformations (Fig. C.2),

$$x = \sum_{i=1}^{8} h_i x_i$$

$$y = \sum_{i=1}^{8} h_i y_i \qquad (C.2)$$
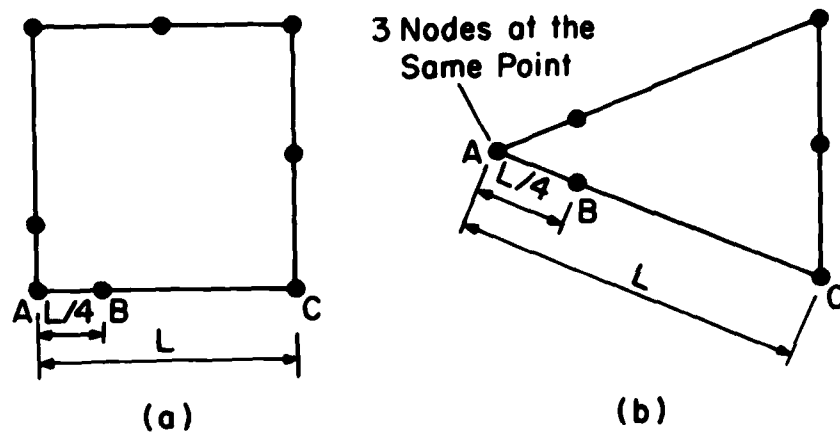
Fig. C.1   Isoparametric quarter point elements.
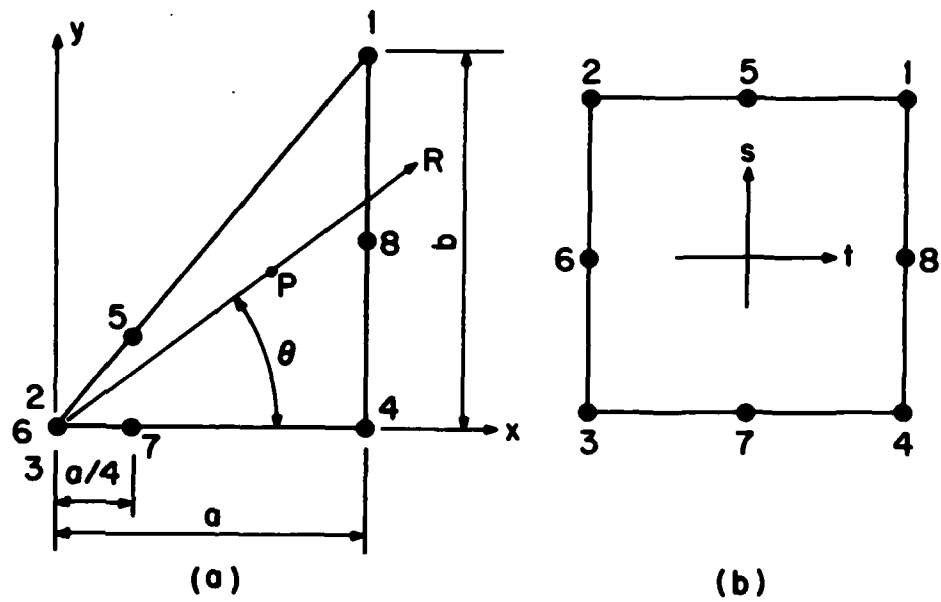
Fig. C.2 Mapping of a triangle into a square.

where h_i are interpolation functions [C.6] and x_i, y_i are the nodal coordinates of the element. For the element shown in Fig. C.2a we have

$$x_1 = x_4 = x_8 = a, \quad x_5 = x_7 = \frac{a}{4}, \ x_2 = x_3 = x_6 = 0 \qquad (C.3)$$

and

$$y_1 = b, \ y_2 = y_3 = y_4 = y_6 = 0, \ y_5 = \frac{b}{4}, \quad y_8 = \frac{b}{2}$$

substituting Eq. (C.3) in Eq. (C.2) by using interpolation functions, and collecting terms we get

$$x = \frac{a}{4} (1 + t)^2 \qquad (C.4)$$

$$y = \frac{b}{8} (1 + s)(1 + t)^2$$

Any point P on the radial line R, is at a distance r from the crack tip,

$$r = (x^2 + y^2)^{1/2} = \frac{b}{8} (1+t)^2 \left[\left(\frac{2a}{b}\right)^2 + (1+s)^2\right]^{1/2}$$

or

$$1 + t = \sqrt{r} / \left\{ \left(\frac{b}{8}\right)^{1/2} \left[\left(\frac{2a}{b}\right)^2 + (1 + s)^2\right]^{1/4} \right\} \qquad (C.5)$$

The Jacobian of transformation $[\underline{J}]$ and its inverse are, respectively, given by

$$[\underline{J}] = \begin{bmatrix} \dfrac{\partial x}{\partial t} & \dfrac{\partial y}{\partial t} \\[2mm] \dfrac{\partial x}{\partial s} & \dfrac{\partial y}{\partial s} \end{bmatrix} = \begin{bmatrix} \dfrac{a}{2}(1+t) & \dfrac{b}{4}(1+s)(1+t) \\[2mm] 0 & \dfrac{b}{8}(1+t)^2 \end{bmatrix}$$

and

$$(C.6)$$

$$[\underline{J}]^{-1} = \begin{bmatrix} \dfrac{2}{a}\dfrac{1}{1+t} & -\dfrac{4}{a}\dfrac{1+s}{(1+t)^2} \\[3mm] 0 & \dfrac{8}{b}\dfrac{1}{(1+t)^2} \end{bmatrix}.$$

The strains are given by

$$\underline{\epsilon} = \left\{ \begin{array}{c} \dfrac{\partial u}{\partial x} \\[3mm] \dfrac{\partial v}{\partial y} \\[3mm] \dfrac{\partial u}{\partial y} + \dfrac{\partial v}{\partial x} \end{array} \right\} \qquad (C.7)$$

The derivatives of displacements u and v with respect to x and y above are obtained by multiplying $[\underline{J}]^{-1}$ by their derivatives with respect to t and s, i.e.,

$$\left\{ \begin{array}{c} \dfrac{\partial u}{\partial x} \\[3mm] \dfrac{\partial u}{\partial y} \end{array} \right\} = [\underline{J}]^{-1} \left\{ \begin{array}{c} \dfrac{\partial u}{\partial t} \\[3mm] \dfrac{\partial u}{\partial s} \end{array} \right\}$$

and $\qquad\qquad\qquad\qquad\qquad\qquad\qquad\qquad\qquad\qquad$ (C.8)

$$\left\{ \begin{array}{c} \dfrac{\partial v}{\partial x} \\[3mm] \dfrac{\partial v}{\partial y} \end{array} \right\} = [\underline{J}]^{-1} \left\{ \begin{array}{c} \dfrac{\partial v}{\partial t} \\[3mm] \dfrac{\partial v}{\partial s} \end{array} \right\}$$

The stress intensity factors, K_I and K_{II}, are normally defined along the line $\theta = 0$ (s = -1). Using s = -1 for simplicity, the strains along this line are given by

$$\underline{\varepsilon} = \frac{1}{1+t} \begin{bmatrix} 0 & 0 & \frac{2t-1}{a} & 0 & \frac{2t+1}{a} & 0 & 0 & 0 \\[2ex] 0 & \frac{2(t-2)}{b} & 0 & 0 & 0 & \frac{2(-t-2)}{b} & 0 & \frac{4(1-t)}{b} \\[2ex] \frac{2(t-2)}{b} & 0 & 0 & \frac{2t-1}{a} & \frac{2(-t-2)}{b} & \frac{2t+1}{a} & \frac{4(1-t)}{b} & 0 \end{bmatrix}$$

$$\begin{bmatrix} \frac{-4t}{a} & 0 & 0 & 0 \\[2ex] 0 & \frac{-4(1-t)}{b} & 0 & \frac{8}{b} \\[2ex] \frac{-4(1-t)}{b} & \frac{-4t}{a} & \frac{8}{b} & 0 \end{bmatrix} \{u_i\} \qquad (C.9)$$

where $\{u_i\}$ is the displacement vector. The stresses in this element are related to the element strains using

$$\underline{\tau} = \underline{C}\, \underline{\varepsilon} \qquad (C.10)$$

where $\underline{C}$ is the elasticity matrix. For plane strain conditions, the stresses are

$$\begin{Bmatrix} \sigma_{xx} \\ \sigma_{yy} \\ \tau_{xy} \end{Bmatrix} = \frac{E}{(1+\nu)(1-2\nu)} \begin{bmatrix} 1-\nu & \nu & 0 \\ \nu & 1-\nu & 0 \\ 0 & 0 & \frac{1-2\nu}{2} \end{bmatrix} \begin{Bmatrix} \varepsilon_{xx} \\ \varepsilon_{yy} \\ \gamma_{xy} \end{Bmatrix}$$

or

$$\left\{ \begin{array}{c} \sigma_{xx} \\ \sigma_{yy} \\ \tau_{xy} \end{array} \right\} = \frac{E}{(1+\nu)(1-2\nu)} \begin{bmatrix} 0 & M_{12} & M_{13} & 0 & M_{15} & M_{16} \\ 0 & M_{22} & M_{23} & 0 & M_{25} & M_{26} \\ M_{31} & 0 & 0 & M_{34} & M_{35} & M_{36} \end{bmatrix}$$

$$\begin{bmatrix} 0 & M_{18} & M_{19} & M_{110} & 0 & M_{112} \\ 0 & M_{28} & M_{29} & M_{210} & 0 & M_{212} \\ M_{37} & 0 & M_{39} & M_{310} & M_{311} & 0 \end{bmatrix} \{u_i\} \qquad (C.11)$$

where

$$M_{12} = \frac{2\nu(t-2)}{b} \qquad M_{22} = \frac{2(1-\nu)(t-2)}{b} \qquad M_{31} = \frac{(1-2\nu)(t-2)}{b}$$

$$M_{13} = \frac{(1-\nu)(2t-1)}{a} \qquad M_{23} = \frac{\nu(2t-1)}{a} \qquad M_{34} = \frac{(1-2\nu)(2t-1)}{2a}$$

$$M_{15} = \frac{(1-\nu)(2t+1)}{a} \qquad M_{25} = \frac{\nu(2t+1)}{a} \qquad M_{35} = \frac{(1-2\nu)(-t-2)}{b}$$

$$M_{16} = \frac{2\nu(-t-2)}{b} \qquad M_{26} = \frac{2(1-\nu)(-t-2)}{b} \qquad M_{36} = \frac{(1-2\nu)(2t+1)}{2a}$$

$$M_{18} = \frac{4\nu(1-t)}{b} \qquad M_{28} = \frac{4(1-\nu)(1-t)}{b} \qquad M_{37} = \frac{2(1-2)(1-t)}{b}$$

$$M_{19} = \frac{-4(1-\nu)t}{a} \qquad M_{29} = \frac{-4\nu t}{a} \qquad M_{39} = \frac{-2(1-2\nu)(1-t)}{b}$$

$$M_{110} = \frac{-4\nu(1-t)}{b} \qquad M_{210} = \frac{-4(1-\nu)(1-t)}{b} \qquad M_{310} = \frac{-2(1-2\nu)t}{a}$$

$$M_{112} = \frac{8\nu}{b} \qquad M_{212} = \frac{8(1-\nu)}{b} \qquad M_{311} = \frac{4(1-2\nu)}{b}$$

From Eqs. (C.5) and (C.11) it can be seen that stresses can be written in the form:

$$\sigma_{ij} = \frac{1}{\sqrt{r}} (E_{ij}\sqrt{r} + F_{ij}) \tag{C.12}$$

where E_{ij} and F_{ij} are the factors to be determined from the result of the finite element analysis. In two-dimensional deformation field, the stress distribution in the vicinity of a crack tip has been shown to take the form [C.7]:

$$\sigma_{xx} = \frac{K_I}{\sqrt{2\pi r}} \cos\frac{\theta}{2} [1 - \sin\frac{\theta}{2} \sin\frac{3\theta}{2}] - \frac{K_{II}}{\sqrt{2\pi r}} \sin\frac{\theta}{2}[2+\cos\frac{\theta}{2} \cos\frac{3\theta}{2}]$$

$$\sigma_{yy} = \frac{K_I}{\sqrt{2\pi r}} \cos\frac{\theta}{2} [1+\sin\frac{\theta}{2} \sin\frac{3\theta}{2}] + \frac{K_{II}}{\sqrt{2\pi r}} \cos\frac{\theta}{2} \sin\frac{\theta}{2} \cos\frac{3\theta}{2}$$

$$\tau_{xy} = \frac{K_I}{\sqrt{2\pi r}} \sin\frac{\theta}{2} \cos\frac{\theta}{2} \cos\frac{3\theta}{2} + \frac{K_{II}}{\sqrt{2\pi r}} \cos\frac{\theta}{2} [1 - \sin\frac{\theta}{2} \sin\frac{3\theta}{2}] \tag{C.13}$$

where K_I is the opening mode of stress intensity factor and is defined as

$$K_I = \lim_{r \to o} \sigma_{yy} (r, \theta=0) \cdot \sqrt{2\pi r} \tag{C.14}$$

and K_{II} is the stress intensity factor for mode II and is also obtained by

$$K_{II} = \lim_{r \to o} \tau_{xy} (r, \theta=0) \cdot \sqrt{2\pi r} \tag{C.15}$$

Therefore, the stress intensity factors, from Eqs. (C.11), (C.14) and (C.15), can be expressed as

$$K_I = \sqrt{2\pi} \, F_{yy}$$

and $\hspace{10cm}$ (C.16)

$$K_{II} = \sqrt{2\pi} \, F_{xy}$$

Further manipulation using Eq. (C.5) with s = -1 leads to the following expressions for K_I and K_{II}:

$$K_I = \sqrt{2\pi a} \, (\sigma_{yy,7} - \sigma_{yy,4})$$

$\hspace{12cm}$ (C.17)

$$K_{II} = \sqrt{2\pi a} \, (\tau_{xy,7} - \tau_{xy,4})$$

where $\sigma_{ij,4}$ and $\sigma_{ij,7}$ are the stresses at nodal number 4 and 7, respectively (see Fig. C.2a). The similar expressions to those in Eq. (C.17) have already been used by Harrop [C.8].

References:

C.1. R. D. Henshell and K. G. Shaw, "Crack Tip Elements Are Unnecessary," Int. J. Num. Meth. Eng., Vol. 9, 1975, pp. 495-507.

C.2. R. S. Barsoum, "On the Use of Isoparametric Finite Elements in Linear Fracture Mechanics," Int. J. Num. Meth. Eng., Vol. 10, 1976, pp. 25-37.

C.3. S. K. Chan, I. S. Tuba and W. K. Wilson, "On the Finite Element Method in Linear Fracture Mechanics," Eng. Fract. Mech., Vol. 2, 1970, pp. 1-17.

C.4. C. F. Shih, H. G. deLorenzi and M. D. German, "Crack Extension Modeling with Singular Quadratic Isoparametric Elements," Int. J. Fract., Vol. 12, 1976, pp. 647-651.

C.5. M. L. Williams, "On the Stress Distribution at the Base of a Stationary Crack," J. Appl. Mech., Vol. 24, 1957, pp. 109-114.

C.6. K.-J. Bathe and E. L. Wilson, Numerical Methods in Finite Element Analysis, Prentice-Hall, Englewood Cliffs, 1976.

C.7. P. C. Paris and G. C. Sih, "Stress Analysis of Cracks," Fracture
      Toughness Testing and Its Application, ASTM STP 381, 1965,
      pp. 30-81.

C.8. L. P. Harrop, "Linear Elastic Stress Intensity Factors Using a
      Distorted Isoparametric Finite Element," Proc. First Int. Conf.
      on Numerical Methods in Fracture Mechanics, edited by A. R.
      Luxmoore and D. R. J. Owen, Swansea, 1978, pp. 302-314.

APPENDIX D: FRICTION BOUNDARY CONDITION BETWEEN CRACK SURFACES

When a crack is located in the compression region the upper and lower crack surfaces will contact each other. If there appears friction between these surfaces the relative sliding motion with respect to each other will be retarded. For the rectangular coordinate system in which the x-axis is parallel to the crack, the boundary conditions of closed crack surfaces may be expressed by the following relations:

$$\sigma_{y\ell} = \sigma_{yu},$$

$$\tau_{xy\ell} = \tau_{xyu},$$

$$\tau_{xy} = \pm \mu\sigma_y,$$

$$v_\ell = v_u$$

(D.1)

where the subscripts ℓ and u indicate the lower and the upper surface, respectively. The sign on the right hand of the third equation should be chosen properly according to the signs of τ_{xy} and σ_y.

In the finite element program based on the displacement method, the stresses are expressed by a linear combination of the nodal displacements for the linear elastic case. Therefore, the stress boundary conditions in Eq. (D.1) can be transformed into linear functions of nodal displacements. By choosing the appropriate relation the frictional boundary condition problem can be solved by FEM.

APPENDIX E: THRESHOLD STRESS INTENSITY RANGE IN MODE II

For cracks in Mode II to propagate, ΔK_{II} should be greater than the threshold range in Mode II. However, there is no experimental data or theoretical work on threshold in Mode II available presently. A very approximate expression for the threshold stress intensity factor in Mode II is derived by formally following the recent work in Mode I by Yu and Yan [E.1].

In monotonic loading case the plastic zone size at a crack tip, ω, can be given by

$$\omega = \frac{1}{2\pi} \left(\frac{\Delta K_{II}}{\tau_y}\right)^2 \tag{E.1}$$

where ΔK_{II} is the stress intensity factor range and τ_y is the shear yield stress. Also, the strain in the plastic zone γ is assumed to follow a modified HRR field solution of the form

$$\gamma = \gamma_y \left(\frac{\omega}{x+\rho}\right)^{1/(1+n)} \tag{E.2}$$

where γ_y is the shear yield strain, x the distance from the crack tip, n the strain-hardening exponent, and ρ the factor added to prevent the plastic strain from reaching infinity at x=0 [E.2]. Thus, the average plastic strain over a length ℓ is obtained by

$$\gamma_{avg} = \frac{1}{\ell} \int_0^\ell \gamma \, dx = \gamma_y \left(\frac{1+n}{n}\right) \left(\frac{\omega}{\ell}\right)^{1/(1+n)} \left[\left(\frac{\ell+\rho}{\ell}\right)^{n/(1+n)} - \left(\frac{\rho}{\ell}\right)^{n/(1+n)}\right] \tag{E.3}$$

For a threshold (at the initiation of crack propagation), the process zone ℓ and also the factor ρ may reach the critical root

root radius ρ_{min}, or the Burgers vector $|\underline{B}|$ since the basic deformation process of metals is slip. By assuming γ_{avg} reaches the fracture strain γ_f and by substituting Eq. (E.1) into Eq. (E.3), we obtain

$$\gamma_f = \gamma_y \left(\frac{1+n}{n}\right)\left(\frac{\Delta K_{IIth}^2}{2\pi\tau_y^2 \rho_{min}}\right)^{1/(1+n)} [2^{n/(1+n)} - 1] \tag{E.4}$$

and therefore from this ΔK_{IIth} can be solved as

$$\Delta K_{IIth} = \tau_y \left[\left(\frac{G\gamma_f}{\tau_y}\right)\left(\frac{n}{1+n}\right)\left(\frac{1}{2^{n/(1+n)}-1}\right)\right]^{(1+n)/2} \cdot \sqrt{2\pi\rho_{min}} \tag{E.5}$$

where G is the shear modulus. By taking n=1 as a first approximation, we get

$$\Delta K_{IIth} = 1.2 \, G\gamma_f\sqrt{2\pi\rho_{min}} . \tag{E.6}$$

If we assume $\gamma_f = [2(1+\nu)/\sqrt{3}]\epsilon_f$, then with $G = E/2(1+\nu)$ and $\nu = 0.3$ the threshold becomes

$$\Delta K_{IIth} = 0.7 E\epsilon_f\sqrt{2\pi\rho_{min}} \tag{E.7}$$

which shows $\Delta K_{IIth} \approx 0.7 \, \Delta K_{Ith}$.

References:

E.1. C. Yu and M. Yan, "A Calculation of the Threshold Stress Intensity Range for Fatigue Crack Propagation in Metals," <u>Fatigue Eng. Mat. Str.</u>, Vol. 3, 1980, pp. 189-192.

E.2. S. d. Antolovich and A. Saxena, "A Model for Fatigue Crack Propagation," <u>Eng. Fract. Mech.</u>, Vol. 7, 1975, pp. 649-652.

APPENDIX F: ELASTIC-PLASTIC INCREMENTAL CONSTITUTIVE RELATIONS USED IN FEM ANALYSIS [F.1]

In elastic-plastic analysis the material behavior is described using three properties in addition to the elastic stress-strain relations, $\underline{c}^E$: (1) a yield condition, (2) a flow rule, and (3) a hardening rule.

The initial and subsequent yield condition for isothermal kinematic or isotropic hardening can be written as

$$^tF(^t\underline{e}^P, \ ^t\underline{\sigma}, \ ^t\kappa) = 0 \tag{F.1}$$

where for isotropic hardening the strain hardening parameter $^t\kappa$ depends on the plastic deformation, and for kinematic hardening $^t\kappa$ is a constant. Restricting the analysis to associated flow rules, the function F in Eq. (F.1) is the plastic potential function to which the normality rule is applicable, i.e.,

$$e^P_{ij} = {}^t\lambda \ \frac{\partial {}^tF}{\partial {}^t\sigma_{ij}} \tag{F.2}$$

or in matrix form

$$\underline{e}^P = {}^t\lambda {}^t\underline{q} \tag{F.3}$$

where e^P_{ij} is the plastic incremental strains and $^t\lambda$ is a scalar to be determined. Since during plastic deformation $^tF=0$, we also have

$$d^tF = \frac{\partial {}^tF}{\partial {}^t\sigma_{ij}} \ \sigma_{ij} + \frac{\partial {}^tF}{\partial {}^te^P_{ij}} \ e^P_{ij} = 0 \tag{F.4}$$

or in matrix form

$$^t\underline{q}^T\underline{\sigma} = {}^t\underline{p}^T\underline{e}^P \tag{F.5}$$

where σ_{ij} is the incremental stresses. The stress increments are calculated from

$$\underline{\sigma} = \underline{c}^E(\underline{e} - \underline{e}^P) \qquad (F.6)$$

Using Eqs. (F.3) and (F.6) to eliminate $\underline{e}^P$ and $\underline{\sigma}$, we obtain

$$^t\lambda = \frac{^t\underline{q}^T\ \underline{c}^E\ \underline{e}}{^t\underline{p}^T\ ^t\underline{q} + ^t\underline{q}^T\ \underline{c}^E\ ^t\underline{q}} \qquad (F.7)$$

Substituting in Eq. (F.6) from Eqns. (F.3) and (F.7) for $\underline{e}^P$ and $^t\lambda$, the elastic-plastic material law at time t becomes

$$\underline{\sigma} = {^t\underline{c}}^{EP}\ \underline{e} \qquad (F.8)$$

where

$$^t\underline{c}^{EP} = \underline{c}^E - \frac{\underline{c}^E\ ^t\underline{q}\ (\underline{c}^E\ ^t\underline{q})^T}{^t\underline{p}^T\ ^t\underline{q} + ^t\underline{q}^T\ \underline{c}^E\ ^t\underline{q}} \qquad F.9)$$

In ADINA the von Mises and the Drucker-Prager yield condit ons have been implemented. When the von Mises yield condition is used the loading surface for isothermal classical isotropic or kinematic hardening is given by

$$^t_F(^t\underline{\sigma},\ ^t e^P,\ ^t\kappa) = \frac{1}{2}(^t s_{ij} - ^t\alpha_{ij})(^t s_{ij} - ^t\alpha_{ij}) - ^t\kappa \qquad (F.10)$$

where $^t s_{ij}$ is the deviatoric stresses and $^t\alpha_{ij}$ is a tensor denoting the translation of the yield surface.

In the case of isotropic hardening, which includes perfectly plastic conditions, we have

$$^t\alpha_{ij} = 0;\quad ^t\kappa = {^t\sigma_y}^2/3 \qquad (F.11)$$

where $^t\sigma_y$ is the yield stress at time t and is a function of the plastic work per unit volume $^t_W{}^P$,

$$^t_W{}^P = \int_0^{^te^P_{ij}} {}^t\sigma_{ij} \; e^P_{ij} \tag{F.12}$$

Evaluating $^t\underline{q}$ and $^t\underline{p}$ we obrain in two-dimensional analysis

$$^t\underline{q}^T = [^ts_{11} \quad ^ts_{22} \quad 2^ts_{12} \quad ^ts_{33}] \tag{F.13}$$

and

$$^t\underline{p}^T = {}^tH \; [^t\sigma_{11} \quad ^t\sigma_{22} \quad ^t\sigma_{12} \quad ^t\sigma_{33}] \tag{F.14}$$

where

$$^tH = 2/3 \; ^t\sigma_y \frac{d^t\sigma_y}{d^t_W{}^P} \tag{F.15}$$

We can now calculate the material property matrix in Eq. (F.9). In Table F.1 the stress-strain relations for two-dimensional plain strain analysis are given. In the case of linear hardening, if the strain-hardening modulus E_T (tangential modulus) is available, ^tH can be calculated as

$$1/^tH = 3/2 \; (1/E_T - 1/E) \tag{F.16}$$

References:

F.1. K.-J. Bathe, Static and Dynamic Geometric and Material Nonlinear Analysis Using ADINA, Report 82448-2, Acoustics and Vibration Laboratory, M. I. T., 1976.

Table F.1. Stress-Strain Matrix in 2D Elastic-Plastic Analysis: von Mises Yield Criterion; Material Isotropic Hardening

$$\underline{C}^{EP} = \frac{E}{1+\nu}
\begin{bmatrix}
\dfrac{1-\nu}{1-2\nu} - \beta\,{}^t s_{11}^2 & \dfrac{\nu}{1-2\nu} - \beta\,{}^t s_{11}\,{}^t s_{22} & -\beta\,{}^t s_{11}\,{}^t s_{12} & \dfrac{\nu}{1-2\nu} - \beta\,{}^t s_{11}\,{}^t s_{33} \\[2ex]
 & \dfrac{1-\nu}{1-2} - \beta\,{}^t s_{22}^2 & -\beta\,{}^t s_{22}\,{}^t s_{12} & \dfrac{\nu}{1-2\nu} - \beta\,{}^t s_{22}\,{}^t s_{33} \\[2ex]
\text{SYMMETRIC} & & 1/2 - \beta\,{}^t s_{12}^2 & -\beta\,{}^t s_{12}\,{}^t s_{33} \\[2ex]
 & & & \dfrac{1-\nu}{1-2\nu} - \beta\,{}^t s_{33}^2
\end{bmatrix}$$

Where

$$\beta = \frac{3}{2}\,\frac{1}{{}^t\sigma_y^2}\; \frac{1}{1 + \dfrac{2}{3}\dfrac{E E_T}{E - E_T}\dfrac{1+\nu}{E}}$$

Distribution List

	Number of Copies
Aero Material Department Naval Air Development Center Warminster, PA 18974 Attn: Mr. M.J. Devine, Code 30-7	1
Air Force Aero Propulsion Laboratory Wright Patterson Air Force Base Dayton, OH 45433 Attn: Mr. C. Hudson	1
Air Force Materials Laboratory Wright Patterson Air Force Base Dayton, OH 45433 Attn: Mr. F. Brooks	1
Defense Documentation Center Building 5 Cameron Station Alexandria, VA 22314	12
National Bureau of Standards Department of Commerce Washington, D.C. 20234 Attn: Dr. A.W. Ruff	1
National Science Foundation Engineering Mechanics Division 1800 G Street Washington, D.C. Attn: Mr. M.S. Ojalvo	1
Naval Air Systems Command Washington, D.C. 20361 Attn: R. Schumaker, Code 340E	1

Director Naval Research Laboratory
Washington, D.C, 20375
Attn: Technical Information Division
     Dr. L. Jarvis, Code 6170
     Dr. R. Ravner
	6

Naval Sea Systems Command Washington, D.C. 20362 Attn: Mr. M. Hoobchack	1
Naval Ship Research and Development Laboratory Annapolis, MD 21402 Attn: Mr. N. Glassman Attn: Dr. J. Dray	1 1

Office of Naval Research
800 N. Quincy Street
Arlington, VA 22217
Attn: Mr. K. Ellingsworth   3

Office of Naval Research
800 N. Quincy Street
Arlington, VA 22217
Attn: Dr. R. Miller, Code 473   1

Mr. D. Anderson
Foxboro Analytical
P.O. Box 435
Burlington, MA 01803   1

Mr. N.L. Basdekas
Office of Naval Research
800 N. Quincy Street
Arlington, VA 22217   1

Mr. J.R. Belt, Code 28
David W. Taylor Naval Ship R&D Center
Annapolis, MD 21402   1

Dr. M.K. Bernett, Code 6176
Naval Research Laboratory
Washington, D.C. 20375   1

Dr. G. Bosmajian, Code 283
David W. Taylor Naval Ship R&D Center
Annapolis, MD 21402   1

Mr. M.A. Chaszeyka
Office of Naval Research - BRO
Chicago, IL 60605   1

Professor H.S. Cheng
Northwestern University
Dept. of Mechanical Engineering &
Astronautical Sciences
Evanston, IL 60201   1

Mr. A. Conte Code 60612
Naval Air Development Center
Warminster, PA 18974   1

Mr. R.J. Craig, Code 2832
David W. Taylor Naval Ship R&D Center
Annapolis, MD 21402   1

Dr. J.F. Dill, Code SFL
Air Force Aero Propulsion Lab
Wright Patterson Air Force Base
Dayton, OH 45433   1

Mr. A.J. D'Orazio
Naval Air Propulsion Center
Trenton, NJ 08628   1

Dr. T. Dow
Battelle Columbus Lab
505 King Avenue
Columbus, OH 43201   1

Mr. E.C. Fitch
FPRC - Oklahoma State University
Stillwater, OK 74074   1

Dr. P. Genalis, Code 1720.1
David W. Taylor Naval Ship R&D Center
Bethesda, MD 20084   1

Dr. P.K. Gupta
Mechanical Technology Inc.
Latham, NY 12110   1

Mr. P.T. Heyl
Pratt & Whitney Aircraft
E. Hartford, CT 06108   1

Dr. D. Jewell, Code 1170
David W. Taylor Naval Ship R&D Center
Bethesda, MD 20084   1

Professor J.H. Johnson
Michigan Technical University
Houghton, MI 49931   1

Dr. J.P. King
Pennwalt Corp.
King of Prussia, PA 19406   1

Dr. M. Klinkhammer, Code 2832
David W. Taylor Naval Ship R&D Center
Annapolis, MD 21402   1

Mr. M. Kolobielski
U.S. Army MERADCOM
Ft. Belvoir, VA 22061   1

Dr. I.R. Kramer
David W. Taylor Naval Ship R&D Center
Annapolis, MD 21402   1

Mr. A.I. Krauter
Shaker Research Corp.
Ballston Lake, NY 12120   1

Capt. L. Krebes
AFOSR/NC
Bolling Air Force Base
Washington DC 20332   1

Mr. S.P. Lavelle
ROYCO Institute
62 Prospect St.
Waltham, MA 02154   1

Professor A.O. Lebeck
University of New Mexico
Mechanical Engineering Dept.
Albuquerque, NM 87131   1

Dr. M. Lee
General Electric Corp. Res. & Dev.
P.O. Box 8
Schenectady, NY 12301   1

Dr. L. Leonard
Franklin Research Center
20th & Race St.
Philadelphia, PA 19103   1

Mr. S.J. Leonardi
Mobil R & D Corp.
Billingsport Rd.
Paulsboro, NJ 08066   1

Mr. W.E. Mayo
Rutgers College of Engineering
P.O. Box 909
Piscataway, NJ 08854   1

Dr. C.J. Montrose
Catnolic University of America
Washington DC 20060   1

Dr. R.W. McQuaid, Code 2832
David W. Taylor Naval Ship R&D Center
Annapolis, MD 21402   1

Dr. P. Nannelli
Pennwalt Corp.
King of Prussia, PA 19406   1

Mr. A.B. Neild, Code 2723
David W. Taylor Naval Ship R&D Center
Annapolis, MD 21402   1

Mr. R.N. Pangborn
Rutgers College of Engineering
P.O. Box 909
Piscataway NJ 08854   1

Mr. M.B. Peterson
Wear Sciences Inc.
925 Mallard
Arnold, MD 21012   1

Professor E. Rabinowicz
Room 35-014
Massachusetts Institute of Technology
77 Massachusetts Avenue
Cambridge, MA 02139   1

Professor D. Rigney
Metallurgical Engineering Department
Ohio State University
Columbus, OH 43210   1

Mr. F.G. Rounds
General Motors Research Labs
F & L Dept.
12 Mile & Mound Road
Warren, MI 48090   1

Mr. W. Rosenlied
SKF Industries Inc.
King of Prussia, PA 19406   1

Dr. N. Saka
Room 35-014
Massachusetts Institute of Technology
77 Massachusetts Avenue
Cambridge, MA 02139   1

Professor N.P. Suh
Room 35-136
Massachusetts Institute of Technology
77 Massachusetts Avenue
Cambridge, MA 02134   1

Dr. J. Tichy
Rensselaer Polytechnical Institute
Troy, NY 12181   1

Dr. R. Valori
Naval Air Propulsion Center
Trenton, NJ 08628   1

Mr. V.D. Wedeven
NASA/ Lewis Research Center
Cleveland, OH 44135   1

Mr. P. Weinberg
Naval Air Systems Command
Washington DC 20361   1

Professor D. Wilsdorf
School of Engineering & Applied Science
University of Virginia
Charlottesville, VA 22903

Mr. A.D. Woods, Code 5243
Naval Sea Systems Command
Washington DC 20360   1

Dr. C.C. Wu, Code 6368
Naval Research Laboratory
Washington DC 20375   1

Mr. R. Lee
Joint Oil Analysis Program
Technical Support Center
Bldg. 780
Naval Air Station
Pensacola, FL 32508   1